SLAC-PUB-613
July 1969
(EXP) and (EXPI)

MULTIBODY PHOTOPRODUCTION BETWEEN 2 AND 16 GEV*

by

M. Davier,† I. Derado,†† D. Drickey,††† D. Fries,†††† R. Mozley,
A. Odian, F. Villa, and D. Yount†††††
Stanford Linear Accelerator Center
Stanford University, Stanford, California 94305

(Submitted to Phys. Rev.)

---

* Work supported by the U. S. Atomic Energy Commission.
† Now at Laboratoire de l'Accelerateur Lineaire, Orsay, France.
†† Now at Max Planck Institut f. Physik and Astrophysik, Munich, Germany.
††† Now at University of California, Los Angeles, California.
†††† Now at Kernforschungs Zentrum, Karlsruhe, Germany.
††††† Now at University of Hawaii, Honolulu, Hawaii.

ABSTRACT

The SLAC 2.2-m streamer chamber has been used to study photoproduction from hydrogen with a 16-GeV bremsstrahlung beam. The use of a single-hadron trigger permitted a study from 2 - 16 GeV which included photoproduction of the Δ^{++} and of the vector mesons ρ, ω, and ϕ. The sample reported here represents 87,000 pictures containing 7,055 hadronic events of which about 2,500 were above 5 GeV. Interesting aspects of the data are: the dominance of ρ^0 production in the 3-prong topology at high energies; the diffraction character of high energy ρ^0 production; the clear indication of the transversality of the ρ^0 spin orientation; the apparent interference between the resonant $\pi^+\pi^-$ (ρ^0) production and a non-resonant background. Tests of the vector dominance model are described including a comparison of total photoproduction cross sections derived from our data with those obtained elsewhere by direct measurements.

I. INTRODUCTION

In studies of multibody photoproduction, the problems of accidental coincidences and of aperture biases make it desirable, and in some cases even essential, to use a large-solid-angle detection system. The accidentals problem is accentuated at machines, such as linear accelerators, which have a small duty cycle. While our group at SLAC was working on the design of a large-solid-angle detector, we learned of the successful operation of streamer chambers by Alikhanian et al.[1] and Chikovani et al.[2] and decided to develop a very large streamer chamber magnet system to yield approximately 4π detection efficiency for photoproduction events. This article is a report on the first experiment performed with the SLAC two-meter streamer chamber.

The experimental setup is indicated in Fig. 1 and Fig. 2. The streamer chamber was located in the one-meter-high, two-meter diameter gap of a 450-ton electromagnet. A collimated low-intensity bremsstrahlung beam of less than 1/2 cm diameter passed through a 1.25-cm-diameter tube of 50 μ wall thickness containing hydrogen gas pressurized to 4 atmospheres absolute and mounted in the upper half of the neon-helium volume. Hadronic events were detected by an array of scintillation counters located on the beam-exit side of the magnet, and photographs of the triggered chamber were taken in three-camera stereo through the open upper pole of the magnet.

In the experiment reported here, 87,000 pictures were taken containing 7,055 hadronic events in a large number of channels. About 2,500 of these were above 5 GeV, but a significant fraction had one or more neutral particles and were difficult to analyze. Preliminary results of the analysis of this experiment have been reported earlier.[3]

II. EXPERIMENTAL APPARATUS

A. Streamer Chamber

Momentum resolution of a few percent is necessary for reasonable kinematic fitting and mass determination at high energies, while the accuracy expected of a streamer track is of the order 0.5 mm in real space. These considerations led to the design and construction of a chamber having a sensitive volume 2-m long, 1.5-m wide, and 60-cm deep with an electrode structure 4-m long, 3-m wide, and 70-cm deep. Streamer formation requires electric fields of about 20 kV/cm and 10-ns duration; the chamber described here requires pulses of 600 kV lasting less than the transit time from one end of the chamber to the other. The production and application of such a pulse was our most serious technical problem.

In a streamer chamber one is attempting to produce a series of small streamers about 1 mm in diameter and 5 to 10 mm long centered on the original particle path. When a high-voltage pulse is applied to a neon-helium volume through which an ionizing particle has passed, ion multiplication occurs, and a Townsend avalanche is formed by electrons cascading in the direction of the positive high-voltage plate. When the ion density and rate of ion formation are sufficiently high, photoionization becomes the dominant process, and streamer formation occurs at both ends of the ionized region. It is during the streamer formation stage that appreciable light is produced; since streamers grow at a rate of order 1 mm/ns, as compared with 1 mm/10 ns for avalanches, the pulse duration is critical, and pulses of order 10 ns are required.

As suggested by Chikovani et al.,[2] the problem of producing a high-voltage pulse of short duration is best handled by separating the high-voltage-generator and pulse-shaping functions. In our case the high voltage was produced by a

17-gap, 34-stage Marx generator[4] rated at 1.3 MV when charged to ± 40 kV. The output with ~150-ns charging time, was used to charge the intermediate electrode of a Blumlein line.[5] Near the peak of the Marx pulse, the Blumlein spark gap broke down by overvoltage producing a pulse of 4-ns risetime. The duration ~10 ns of the Blumlein pulse was twice the transit time of the charging element in oil and could be varied by substituting charging elements of different length. The virtue of the Blumlein, as compared with other pulse-shaping networks, is that it produces a "rectangular" pulse with the full charging voltage. The use of a single gap in the Blumlein, instead of the 17 gaps of the Marx generator, permits a small inductance and hence a fast rise. In practice the generator was charged to about ± 20 kV, and the Blumlein pulse was then about 600 kV.

As indicated in Figs. 1, 2 and 3, the Blumlein pulse was applied to a central electrode separating the upper and lower 30-cm gaps of the streamer chamber. The outer electrodes were at ground potential and were joined at the sides to make an enclosed-line configuration which reduced the otherwise large amount of rf radiation from the fast pulse. Since the electrode dimensions were comparable with the product of pulse duration times velocity, the chamber was driven as a transmission line and was terminated with a distributed impedance of 23 Ω .

In the visible region of the chamber the three electrodes consisted of stainless steel wires 0.25 mm in diameter and spaced about 5 mm apart. The neon-helium gas was contained in cells with polyurethane walls and top and bottom windows of 2-mil Mylar. An example is shown in Fig. 4. The streamer chamber developments at SLAC are described in detail in a SLAC report and have been summarized in various conference proceedings.[6]

B. Camera System

A major problem in the use of streamer chambers is that very little light is emitted. This is coupled to the fact that the chambers do not saturate since they are not loaded by streamers. As a result special film with high acutance and sensitivity to neon light is required. In the experiment reported here, Kodak special order SO-340 film was used with Zeiss Planar lenses and with lens apertures of F2. A demagnification of 70 yielded a reasonable depth of field and allowed us to use a 35-mm sprocketed film format.

Events were photographed by three cameras mounted 4 m above the chamber with vertical lens axes and a stereo angle of 18^{o}. For the F2 lens apertures, vignetting occurred at about this angle. The locations of events in the magnetic field were determined with the aid of 25 fiducials on a marble plate pinned to the lower magnet pole and 2 upper fiducials supported by granite beams attached to the four vertical flux-return columns of the magnet. Figures 5 and 6 show typical photographs.

C. Magnet

The magnet was designed to allow access to the field region from all sides. There was no upper pole so that the chamber could be viewed and photographed from above. Seven double coils were installed above the 1-m magnet gap and three around the lower pole tip to produce an approximately symmetric field. The coils were formed of 2.5-cm × 3.75-cm copper tubing wrapped with fiber glass and vacuum impregnated with epoxy to form double pancakes.

Each of the top and bottom plates of the magnet was laminated from two separable plates weighing less than 50 tons each to facilitate assembly and later modification. The magnet weighed approximately 450 tons of which 50 tons were the coils. The entire detection system, including magnet, streamer

chamber and drive system, cameras, trigger counters, and fast electronics, was assembled as a unit outside of the beam line and was moved into the beam on rails. Once in place, the magnet and peripheral gear were elevated to the proper beam height by four jacks, and the final alignment was made.

During the experiment reported here, the 5.8-MW magnet power supply was limited by transformer failures and produced a field of only 8 kG. The field distribution in the central region is shown in Fig. 7.

D. Trigger Electronics

The experiment was intended as a survey and was designed to be triggered by any charged hadron leaving the magnet in the forward $\sim 15^{\circ}$ cone. The principal background for false triggers was from electromagnetic interactions: The pair cross section is approximately 200 times larger than the total hadronic cross section, and the Compton cross section is large enough to cause many false triggers from the numerous low-energy photons in a bremsstrahlung spectrum.

To reduce the triggers from pairs, which occur mainly at small angles, the trigger counters were separated by a 20-cm horizontal gap in the beam plane. Very few high-energy Compton electrons were produced, and low-energy electrons were swept aside by the magnetic field. The background from materializing Compton photons was minimized by placing as little material as possible before the first plane of trigger counters and by making this plane only 6-mm thick.

The trigger counters were arrayed in four vertical planes perpendicular to the photon beam line. Polyethylene sheets 1 inch thick were placed between the counter planes to reduce the number of soft electrons that could penetrate. In addition, approximately two radiation lengths of lead were introduced between

the second and third layers and 1-1/2 radiation lengths between the third and fourth layers to make it possible to identify showers from high-energy electrons. The trigger logic required a pulse from each layer and no large pulse from the last two layers of a triggering zone. The counters formed a 32-zone hodoscope covering an area two feet high and eight feet wide above the beam and a similar area below. A proper four-fold coincidence in any zone caused the chamber to fire. This allowed the rejection of triggers from electrons without the rejection of hadronic events with π^0's.

A problem with a streamer chamber is the pickup from electromagnetic radiation when the chamber fires. This was reduced many orders of magnitude by completely enclosing the chamber high-voltage electrode; nevertheless, additional shielding of the counters and cabling was required. The firing of the streamer chamber took place about 750 ns after the trigger logic had functioned, and multiple redundant gates throughout the logic provided additional rf protection.

The ratio of pictures to hadronic events was reduced by the trigger system from several hundred to one with no trigger to about 12 to one. A complete removal of electromagnetic backgrounds would have resulted in ratio of about three to one, as the target hydrogen in the chamber volume was about one-third the total effective material in the beam line near the counter system. Some of the false triggers came from Compton scattering in the Mylar windows and helium gas bag near the trigger counters, but a large fraction apparently came from showers of soft photons originating in the upstream beam line. A relatively small number of false triggers were from pairs; the shower rejection reduced the false trigger rate by only about 10%. In a subsequent run with the hydrogen gas target pressurized to 6.5 atmospheres absolute, it has been possible to reduce the ratio of pictures to hadronic events to about 4.5 to one.

E. Photon Beam

A special effort was made to produce a well-collimated photon beam. Since particle trajectories inside the hydrogen target tube were not seen, it was essential that the target and beam diameter be small. Moreover, even with high pressure (~4 atmospheres absolute) hydrogen, the target walls, flanges, and neon-helium gas were much thicker in radiation lengths than the hydrogen; thus beam halo had to be reduced to a minimum.

The photon beam line and radiator area are shown in Fig. 8. Basically the system consisted of a point radiator, a source-defining collimator C-1, the primary collimator C-2, and two scraping collimators C-3 and C-4, which do not intercept the primary photon envelope. The electron beam from the accelerator was momentum analyzed to less than 1% momentum width, was focused at the collimator C-2, and after striking the radiator was deflected to a beam dump by a magnet system. The beam at the radiator was essentially parallel since the beam phase space was less than 10^{-5} radian-cms. The radiator itself was 1 mm in diameter and 0.25 μ thick, and was suspended on three 10-μ wires of stainless steel.

The first collimator C-1 was located 17 meters beyond the radiator and consisted of 20-radiation length horizontal and vertical copper jaws in tandem; the openings and centering could be separately varied. The source-defining collimator was followed by a sweeping magnet in which was located a beam hardener of one radiation length LiH. Following the hardener, the beam proceeded 30 meters to a second collimator, C-2, consisting of a 1-mm-diameter hole in 60 radiation lengths of tungsten. The centering of this hole and of several others in the same tungsten block could be remotely adjusted. Following the two primary collimators, the beam proceeded 30 meters to a scraping

collimator, C-3, similar in design to C-2, with a nominal diameter of 5 mm. A second scraping collimator C-4 was fixed in a location 15 meters beyond C-3 and had a nominal hole diameter of 10 mm.

A laser beam transmitted by C-2, C-3 and C-4 was used to align the hydrogen target tube and was traced to the entrance window of the quantameter some 39 meters beyond the center of the streamer chamber. The photon beam itself was used to check the alignment at the beginning of the run. Final checks of the beam centering were made by studying the trigger rate and by visually monitoring backgrounds in the streamer chamber for different centering values of C-2 and C-3. The response was normally independent of the C-2 and C-3 settings for values within a few tenths of 1 mm of beam center.

The photon beam was monitored in a quantameter calibrated to a few tenths of 1% with electron and positron beams and the SLAC Faraday cup.[7] The quantameter drift with no beam corresponded to less than 100 equivalent quanta per second assuming a standard 95% Argon-5% CO_2 gas filling. Since the beam intensity was over 100 equivalent quanta per pulse at 180 cycles per second, the effect of drift was normally less than $\pm$ 1%. The quantameter was operated at ambient temperature and pressure, and the gain was not corrected for changes in these quantities. Considering the various factors mentioned, we have estimated an overall uncertainty for the experiment of $\pm$ 2.5%.

The photon beam was also monitored by a thin scintillation counter directly in front of the quantameter. The signal from this counter was displayed on an oscilloscope to indicate beam time-structure, and it was frequently used in beam tune-up as an instantaneous current monitor.

The streamer chamber system was insensitive for about 0.3 seconds after each firing; the beam lost during this deadtime period was determined by counting pulses in the above-mentioned scintillator. It was necessary to measure the

energy spectrum of the photon beam since the well-known bremsstrahlung spectrum could be affected by collimator edges and particularly by the beam hardener. The hardener was installed in a 15-kG field to reduce secondary radiation; its location 45 meters upstream of the primary collimator C-2 also reduced any such low-energy contamination.

The photon spectrum was checked by measuring the energies of pairs produced in the hydrogen gas target tube. It was essential to use pairs which did not trigger the chamber since the trigger counters were intentionally biased against pairs. An unbiased sample could be obtained with a trigger timed to occur during an accelerator pulse and not derived from the trigger logic, but in this experiment we used pairs found in frames containing hadronic events. The chance of a non-triggering hadronic event occurring randomly on a frame triggered by a positron-electron pair was negligible.

All frames containing hadronic events were scanned for pairs within the same fiducial volume used for hadrons. A difficulty in this scan was the possible confusion of pairs with events when neither vertex was seen; thus pairs visible within a region extending 17.5 cm downstream of the hadronic vertex were not used. It was essential to study the pair spectrum as a function of the position in the fiducial volume since high-energy pairs were often missed in the down-stream end of the chamber due to the unseen vertex.

The pair spectrum obtained with appropriate corrections for fiducial volume is shown in Fig. 9. An enhancement of the low-energy region would be expected if there were problems related to collimator edges or the use of a beam hardener. Within the statistical accuracy of the sample, the agreement with the predicted Bethe-Heitler spectrum is satisfactory.

The total photon intensity determined from the pair scan was compared with that measured by the quantameter. Pairs were assumed to provide a random sample of the intensity during operation, and the attenuation of low-energy (< 50 MeV) photons by the beam hardener was neglected since only the total energy was measured by the quantameter. Each 120-meter roll of film was analyzed separately and represented roughly a one-hour sample of the total run. Beam instability would cause a second-order error due to the fact that more samples were made at times of high intensity than at low intensity. Since the beam was monitored continuously, an increase of no more than 5% in the pair yield was expected. A correction was made to the pair rate because the chamber sometimes fired before the 1.5 μs accelerator beam pulse was over. In addition, there was occasional difficulty in distinguishing hadronic events from two or more pairs.

After all corrections were made, the pair yield between 1 and 16 GeV, determined from a sample of 200 events, was 85% of that calculated from the quantameter. Since the pair analysis was estimated to involve a net systematic error of about 10%, this agreement was considered satisfactory. The quantameter data, which were accurate to $\pm$ 2.5%, were used in the final cross-section calculations.

III. ANALYSIS

A. Film Scanning

Two independent scans were made and about one frame in twelve contained a hadronic event. A strong interaction could be distinguished by the angle of emission of the tracks and by the requirement that there be one more positive than negative track. The problem was complicated by the lack of a visible

vertex and by the presence of flares in the chamber. Typical frames are shown in Figs. 5 and 6. The lack of a vertex caused occasional pairs to be included wrongly in events, and these were removed in the manner to be described. The flares often obscured the vertex region and could have caused a scanning bias. As a result a cut was made on all events with tracks of dip-angle λ greater than 45°. This is also discussed in more detail below.

Scanning was relatively easy since there was less than one background pair per picture. The statistical efficiency from two scans was 0.99. Systematic scanning errors were undoubtedly present for certain event configurations, and these were estimated to result in a loss of 5%. The scanning statistics were as follows:

Photographs scanned	87,000
Events found	7,055
Ambiguous events	993
Only one view	21
One prong	687
3 and more prongs	5,074
Strange particles	280

B. Film Measuring and Spatial Reconstruction

Events were measured on an image-plane digitizer at 3 to 15 points per track in each of three views. Camera positions were located by measuring twelve lower fiducials and two upper fiducials. Three fiducials were used for ordinary event reconstruction. Lens errors for each measured point r_0 in the film plane were compensated by assuming a radial distortion of the form

$$r = r_0 - \alpha \sin^3 \gamma$$

where γ is the angle between r_0 and the optic axis.

Since the vertex was not observed and the magnetic field was very non-uniform, a fitting program SYBIL[8] was developed for the geometrical reconstruction of the events. All tracks were fitted simultaneously; the errors for the different tracks were not independent, and the analysis produced a correlated error matrix. The exact particle trajectories were used instead of an helical approximation. The resulting geometrical fits were consistent with an average measuring error on film of 8-μ in each coordinate direction. The 8-μ error corresponds to 0.56 mm in real space.

Figure 10 shows a histogram of the geometric standard deviations of 3 prong events reconstructed by SYBIL. All events which did not pass SYBIL were remeasured, and after two measurements, 4,460 of 5,074 events passed. About 2.5% did not converge, and the remainder were rejected for technical reasons. Strange particles, one-prongs, and events with greater than nine prongs were not measured. In the 4,460 events which passed SYBIL there were:

3,182	3 prongs
1,025	5 prongs
221	7 prongs
32	9 prongs

For a more complete discussion of the performance and resolution of a streamer chamber see Ref. 8.

C. Determination of the Vertex Position

The error in the vertex position transverse to the beam was less than 0.5 mm in real space. The error along the beam direction depended strongly on the event type since high-energy particles frequently did not leave the target for several centimeters. The largest error was in the vertical coordinate, about $\pm$ 2 mm caused by the $\simeq 18^{\circ}$ stereo angle.

To test whether the beam struck the 50 μ Mylar wall of the target tube, events were plotted (Fig. 11) as a function of vertex position along the line of viewing (vertical coordinate) and along an orthogonal line also perpendicular to the beam direction. The profiles are consistent with beam dimensions of 6 mm and 3 mm respectively. The absence of any accumulation of events at the wings of the beam profile distribution confirms that the beam was not striking the Mylar.

D. Contamination of Events by Pairs

When a pair vertex occurred very close to a 3-prong event vertex, the configuration could be mistaken for a 5-prong event in both scanning and measuring steps. Figures 12a-c summarize an analysis of the tracks of all 5-prong events. Figure 12a shows the tracks with no angular cut, while Fig. 12c shows all tracks in those events in which both the smallest-angle positive and the smallest-angle negative tracks have λ and ϕ angles of less than 40 mr where λ is again the dip angle, and ϕ is the angle between the track and the beam direction projected onto the horizontal plane. From such cuts we have found 76 3-prong events falsely identified as 5-prongs and 27 5-prongs falsely identified as 7-prongs. This is the same ratio as that of the 3-prong to the 5-prong events identified as such. Moreover, the events identified in this way had the same percentage of kinematic fits as the classes to which they were assigned. Finally, the pairs detected in association with these events had an energy distribution above 3 GeV compatible with a bremsstrahlung spectrum.

E. Kinematic Determination

After the reconstruction of momenta and angles of the particles, the events were subjected to the constraints of energy and momentum conservation in a least square procedure TEUTA.[8] Since the energy of a particular photon

in the bremsstrahlung spectrum was unknown, completely visible final states resulted in fits having 3 constraints (3-C fits) if the identity of each particle was assumed. A single missing neutral with assumed identity (π^0, neutron) led to a zero-constraint (0-C) kinematic fit. A fit was defined by conservation of energy and momentum to less than 10^{-4} GeV with $\chi^2 < 30$. In 3-C events the particle identity could be determined from the fit; in 0-C events the distinction between proton and positive pion generally could not be made kinematically (assuming a missing π^0), nor could one be sure that any of the tracks were protons (missing neutron). Ionization information was used to restrict the choices in about 20% of the 0-C events. Since there was an 80% probability of having more than one neutral,[9] further analysis of 0-C events was very difficult.

The 3-prong events were fitted with the appropriate 3-C and 0-C pion and kaon hypotheses. (For 5-prong and 7-prong events the choice of hypotheses was of course much greater.)

The probability distribution of the 3-C events showed an accumulation of low probability fits. Errors for low-momentum tracks were underestimated since multiple scattering and energy loss in the Mylar and gas were neglected. The measurement error assumed for such events should be increased. This has been checked by increasing the assumed measurement error in discrete steps and observing the increase in the number of events satisfying 3-C fits. A plateau was reached beyond which further increases in the assumed measurement error did not increase the number of fitted events having χ^2 probability of greater than 1%. At that point few 0-C events had entered the low-probability category for 3-C events.

A further test of kinematically selected events was made by studying the mass-squared distribution of the incident photon given by

$$m_\gamma^2 = p_\gamma^2 - \left[\sum_i P_i - P_{\text{proton}}^{\text{inc}}\right]^2$$

where the P_i are the four vectors of the outgoing particles in the reaction. Figure 13 is a plot of M_γ^2 for $\chi^2 < 30$ and for $\chi^2 > 30$. The value of 30 was determined empirically by decreasing the acceptable χ^2 until the M_γ^2 peak began to appear in the high-χ^2 plot. The cut for $\chi^2 > 30$ resulted in the same number of events as that given by the variation in assumed measuring error and was the actual criterion used for all data. The small number of solutions incompatible with the ionization information were rejected.

IV. TRIGGER AND GEOMETRIC EFFICIENCIES

A. Counter Efficiencies

The streamer chamber was fired by any particle passing through a counter hodoscope located down-beam from the chamber. As described earlier, the hodoscope consisted of four layers in coincidence covering two areas 60 cm by 240 cm above and below a 20 cm gap in the central plane. To check trigger efficiency, tracks from events of over 2 GeV were extrapolated from the measured trajectories in the streamer chamber to the position of the trigger counters.

Figure 14 is a plot showing the position of interception at the trigger counters of those events in which only one track intercepted the trigger counters plus a 30-inch border. There are no obviously insensitive regions in this plot nor in similar plots for other classes of events; we assume, therefore, that the counters were operating normally and that their efficiencies were high enough to permit a meaningful correction of about 2% per counter plane to be made for the monitored counter instabilities.

B. Geometrical Efficiencies

The greater concentration of events near the center of Fig. 14 suggests that geometrically a reasonable sample of all possible events was obtained.

In particular, if a positive particle was emitted to the right in a magnetic field that swept to the left, it would have had a much greater chance of triggering than the same particle emitted to the left. The magnetic field thus insured that the sample contained a significant number of events in which the angle between the beam line and the track direction was large. The existence of a subsample of large-angle events, appropriately weighted, implies a relatively large effective solid angle for the triggering system.

Flares were frequently observed in the chamber in association with steep tracks approximating the direction of the pulsed electric field. Streamers tended to coalesce when the dip angle λ was large, and an intense discharge could then occur along the track. The charge deposited on the Mylar windows of the neon-helium cells accumulated until a surface breakdown or flare was formed.

In correcting for flares associated with steep tracks, we have used the intrinsic symmetry about the beam axis that is characteristic of events produced by unpolarized bremsstrahlung. Since the dip angle λ coincides with the production angle θ in the particular case of tracks originating in the plane containing the beam and the vertical axis ($\psi = \pm 90^{\circ}$ where ψ is the angle of rotation of the track about the beam line), it then suffices to compare the distributions in θ for tracks near the vertical beam plane ($\psi \simeq \pm 90^{\circ}$) and for tracks near the horizontal beam plane ($\psi \simeq 0^{\circ}$ or 180°); the ratio of the two θ distributions gives directly the efficiency as a function of dip angle:

$$\epsilon(\lambda) = \frac{4\left[N(\theta)\right]_{|\psi|}}{\left[N_0(\theta)\right]_{\psi}} \quad \begin{matrix} = (90 \pm 10)^{\circ} \\ = 0^{\circ} \pm 40^{\circ} \text{ or } 180^{\circ} \pm 40^{\circ} \end{matrix}$$

The data plotted in Fig. 15 indicate that the probability of missing a track increases rapidly after $|\lambda| > 45^{\circ}$.

C. Trigger and Geometric Efficiency Corrections

The method used in correcting the trigger and geometric efficiencies depended essentially upon the rotational (ψ) symmetry of events about the beam axis, and the same method applied in both cases. Because of scanning and measuring inefficiencies, only events having $|\lambda| < 45^{\circ}$ for all tracks were used. Each event in this sample was rotated through 360° in N successive intervals $\Delta\psi$ (N = 36). At each interval three operations were performed:

1. A function $t(\psi_j)$ was assigned a value 1 or 0 depending upon whether or not at least one track in the event extrapolated to give a "virtual" hit at the counter array.

2. The product, $f(\psi_j) = \prod_{i=1}^{N} \epsilon(\lambda_i^j)$, was calculated where $\epsilon(\lambda_i^j)$ was the geometrical efficiency for the i-th track at the rotational angle ψ_j and was defined to be unity for $|\lambda_i^j| < 45^{\circ}$ and zero elsewhere.

3. A correlation function, $C(\psi_j) = t(\psi_j)\, f(\psi_j)$, was formed for the two effects and the average acceptance calculated:

$$A = \frac{1}{N} \sum_{j=1}^{N} C(\psi_j) \quad .$$

The weight was then 1/A for that event.

The choice of intervals $\Delta\psi$ was determined by the rapidity of the variation of $t(\psi)$. For example, too large an interval might have caused certain extrapolated tracks consistently to miss the gap in the trigger counters and hence to yield a higher efficiency than actually obtained. Such considerations led to a choice of 36 intervals of 10° each. The correction described was made by a program ISIS.[8]

D. Limitation of the Method

The method described above is valid for a given class of events if two conditions are satisfied:

1. There must be enough events in the class to provide a statistically significant sample of all event types included in that class.

2. All geometric configurations should be represented in the event class.

Acceptance histograms are given in Fig. 16 for events of the type $p\pi^+\pi^-$ between 4 and 8 GeV; the variation of the weighting with energy is shown in Fig. 17. Below 2 GeV the acceptance was poor, making it probable that certain classes of events are missing. Hence distributions obtained in this region are suspect.

Figure 18 shows the variations with photon energy of the total efficiency for the reactions $\gamma p \rightarrow \pi^+\pi^- p$ and $\gamma p \rightarrow \pi^+\pi^-\pi^+\pi^- p$. In each case the efficiency first increases with energy (at low energies particles are swept away from the counters by the magnetic field) and reaches a maximum, the peaks occurring at 7 and 10 GeV respectively. In the 3-prong case there is a clear decrease in efficiency at the highest energies due to particles passing through the horizontal gap separating the upper and lower trigger counters. For the 5-prong events, the effect is not clear.

E. Effects of the Efficiency on Physical Observables

A second approach to estimating the detection efficiency and in addition determining whether variations in efficiency affect certain physical quantities, was to generate events by Monte Carlo methods.[8] We consider here, in particular, events of the type $\gamma p \rightarrow \pi^+\pi^- p$ satisfying the following characteristics:

1. The invariant $\pi^+\pi^-$ mass distribution had the mass and width of the ρ_0 meson.

2. The t distribution was of the form $e^{-8|t|}$.

3. The sample of photon energies had a bremsstrahlung distribution.
4. The angular distribution of the ρ^0 decay was $\sin^2\theta$ in the helicity system.
5. The exact geometry and magnetic field of our experimental setup were used.

The generated Monte-Carlo events are compared with the accepted Monte-Carlo events as a function of t in Fig. 19. The acceptance function versus di-pion mass for the Monte Carlo events is plotted in Fig. 20. The facts that the t dependence does not differ appreciably for generated and accepted events and that the mass sensitivity is flat in the regions of interest imply that the corrections are mainly an overall renormalization of the data and do not affect the shape of the experimental distribution.

Figure 21 shows the fraction of the Monte Carlo events accepted as a function of the decay angle θ_H in the helicity system. Here the flat response indicates that the decay distribution in the helicity frame is not appreciably affected by the acceptance function.

The Monte Carlo efficiency as a function of photon energy is compared in Fig. 18 with corresponding efficiency determined by rotating real events in the manner already described. Within the statistical accuracy of this comparison the agreement is adequate.

F. Determination of Absolute Cross Sections

In obtaining absolute cross sections, four pieces of information are required:

1. The total flux of incident photons.
2. The shape of the bremsstrahlung.
3. The overall detection efficiency, including the efficiency of the apparatus and of the data analysis.
4. The number of events actually observed.

As discussed in Section II. E., relating to the photon beam, the incident flux was measured to an accuracy of $\pm$ 2.5% with a quantameter. This was checked to $\pm$ 10% by monitoring the yield of pairs produced in the chamber.

Tests of the individual counters used in the experiment gave an efficiency of better than 98% and an estimated four-fold trigger efficiency of about 92 $\pm$ 4%. In addition, during short intervals certain counters of the hodoscope malfunctioned. Individual rolls of film were corrected on the basis of the particular counter area, and the total effect on the experiment was less than 1%.

The distribution of event vertices showed a decrease at either end of the target. At the upstream end this was due to the fact that certain low-energy events never reached the trigger counters. At the downstream end the loss was due primarily to the horizontal slot between upper and lower trigger counters. These two effects were taken into account in the principal correction for detection efficiency made by rotating events about the beam axis in the manner already described – a procedure which we estimate was valid to $\pm$ 5%.

A third factor influencing the target fiducial volume was related to the low magnetic field; particles originating at small angles near the downstream end of the target frequently remained within the target tube and were not seen. This effect was particularly severe for high-energy 3-prong events, and it has caused us to reduce the fiducial volume with increasing energy rather than try to correct for these losses. The useful target length was 1.35 m below 8 GeV, 0.50 m between 8 and 12 GeV, and 0.40 m between 12 and 16 GeV.

A statistical evaluation of the scanning efficiency gave 99 $\pm$ 1%, as mentioned earlier. In addition, there was a systematic inefficiency due to ambiguous events that could not be classified either by energy or by channel. Assuming these were distributed in proportion to the populations of normal

events, we estimated that there were 460 ambiguous 3-prongs as compared with 3182 normal 3-prongs. The scanning efficiency for this effect was then $87 \pm 3\%$. The measuring efficiency, defined as the fraction of all measured events which passed the geometrical fitting program SYBIL, was $88 \pm 2\%$.

By combining quadratically the errors given in this section, we have obtained an estimate of about $\pm 8\%$ for the systematic uncertainties in our absolute-cross-section data. This is in addition to the statistical errors calculated from the number of events actually observed in the individual channels.

V. EXPERIMENTAL RESULTS

A. The reaction $\gamma p \rightarrow \pi^+ \pi^- p$

1. General Features

Cross sections for photon energies between 2 and 16 GeV for the reaction $\gamma p \rightarrow \pi^+ \pi^- p$ are plotted in Fig. 22 and are tabulated below. Our results are in good agreement with those of the DESY[10] and CEA[11] bubble chambers below 6 GeV and with the SLAC[9] bubble chamber exposures to a monochromatic beam at 5 and 7.5 GeV.

The invariant mass distributions for $(p\pi^+)$, $(p\pi^-)$, and $(\pi^+\pi^-)$ are shown in Figs. 23, 24, and 25. In Fig. 23 a prominent Δ^{++} (1236 MeV) is seen decreasing rapidly with increasing photon energy. At photon energies above 2 GeV the production of ρ^0 mesons dominates the $(\pi^+\pi^-)$ distribution of Fig. 25 and within our statistics is constant with energy.

Apart from the Δ^{++} and the ρ^0 no other resonance can be positively identified at our statistical level. It appears, however, that there may be some f^0 (1260 MeV) between 2 and 4 GeV in Fig. 25, decreasing rapidly at

higher energy. The possible existence of $(\pi^+\pi^-)$ resonances strongly produced by photons is of interest since diffraction production would imply a selection of quantum numbers of which $J^P = 1^-$, those of the photon, are the simplest case. Such resonances could play an important role in explaining the electromagnetic structure of nucleons as does the ρ^o. Our data set limits on the production of such resonances at the level of 0.1 μb per event between masses of 1 and 2 GeV ($4 < k < 16$ GeV) and 0.3 μb per event between masses of 2 and 3 GeV ($8 < k < 16$ GeV).

2. The reaction $\gamma p \rightarrow \rho^o p$

To calculate the cross section for ρ^o production it is necessary to evaluate the fraction of ρ^o's in the $\pi^+\pi^-$ mass spectrum. One must also take into account the effects of the reflection of the $\Delta^{++}(p\pi^+)$ resonance and of the phase space for production of $\pi^+\pi^-$ pairs. For the ρ resonance we have used a Breit-Wigner shape[12]

$$\sigma_{\rho'}(m) = c_\rho \frac{\Gamma_\rho(m)}{(m^2 - m_\rho^2) + m_\rho^2 \Gamma_\rho^2(m)} \qquad \text{(Fit A)}$$

where

$$\Gamma_\rho(m) = \Gamma_0 \left(\frac{q}{q_\rho}\right)^3 \frac{m_\rho}{m} \qquad \text{(Shape I)}$$

and where q is the pion momentum in the center-of-mass of the di-pion, and Γ_0 is the ρ width. ρ subscripts for m and q refer to the mean value of the di-pion mass. Among other more empirical forms for the width, one frequently used is

$$\Gamma_\rho(M) = \Gamma_0 \left(\frac{q}{q_\rho}\right)^3 \frac{1 + (q_\rho R)^2}{1 + (qR)^2} \qquad \text{(Shape II)}$$

where k is a constant equal to 3.58 GeV^{-1}. Either of these expressions gives virtually the same result, and we have used the second form in the analysis which follows. The Δ^{++} resonance has been fitted in the same manner as the ρ. We have fixed m_Δ, Γ_Δ, and Γ_ρ = 150 MeV so that the only free parameters are m_ρ, c_ρ, c_Δ, and a phase-space factor, all of which we adjust with the program MURTLEBERT.[8]

Figures 26a, b, and c show the best fits to the $\pi^+\pi^-$ mass plots in three energy regions. (See Table I, Fit A.) The fitted values of m_ρ (~720 MeV) are different from those found in pion production or in storage-ring experiments (~770 MeV), and the observed shape differs from the above predictions. The ρ mass disagreement increases slightly with energy, although it is statistically compatible with a constant value. The probabilities for the fits shown are very low, and it appears that the expression (Fit A) for σ_ρ(m) is not correct. The asymmetry observed has been predicted by Ross and Stodolsky, Fit B,[12] who introduce a $\left(\frac{m_\rho}{m}\right)^4$ factor into the cross section by a vector-dominance calculation in which the mass of the ρ coupled to the photon is the mass of the final state 2π system. The fit is improved but not satisfactory, and there are problems with this assumption which lead one to look for the causes of the asymmetry in an interference effect. We have tried a third, purely phenomenological analysis within a region (500-950 MeV) near the ρ resonance (Fit C):

$$I(m) = Am + B + \sigma_\rho(m)$$

where σ_ρ(m) is given above. The ρ width and mass determined by this analysis are also given in Table I. Another approach by Söding[12] will be considered below.

In determining the fraction of ρ's in the $\pi^+\pi^-$ samples we have used Breit-Wigner fits (Fit A) which give values statistically compatible with the Ross-Stodolsky fits (Fit B). Fit C dealt only with the central part of the ρ region and was used to study the mass and width. The results are plotted in Fig. 27 together with earlier DESY[10] measurements. As the energy increases, the reaction $\gamma p \rightarrow \pi^+\pi^- p$ is more and more dominated by ρ^o production which reaches a level of $(97 \pm 4)\%$ in the range 8 to 16 GeV. The cross sections for ρ photoproduction are shown as a function of energy in Fig. 28 and are tabulated below:

Photon Energy k	$\sigma(\gamma p \rightarrow \rho^o p)$
GeV	μb
2-4	19.2 ± 2.3
4-8	15.6 ± 1.7
8-16	13.4 ± 3.6

The ρ-production differential cross sections are shown in Fig. 29 and Table II as a function of momentum transfer t' where

$$t' = t - t_{min} \quad ,$$

and

$$t_{min} \simeq \left(\frac{m_\rho^2}{2k} \right)^2 \quad .$$

At energies above 4 GeV, t_{min} differs negligibly from zero. We fit our t distributions with the function

$$\frac{d\sigma}{dt} = Ae^{-Bt'} \quad ,$$

and we use all of the points in Fig. 29 except those at the smallest momentum transfer. (The loss of events at very low momentum transfer is due to protons

of less than about 60 MeV/c momentum stopping in the 50 μ Mylar walls of the target tube.)

We have studied the angular distributions of the $\rho \to \pi^+ \pi^-$ decay in two reference systems:

The Jackson frame is defined as the di-pion center-of-mass system with the Z direction that of the incident gamma transformed to the di-pion center-of-mass system, with Y perpendicular to the production plane ($\vec{P}\gamma \times \vec{P}_\rho$, where $\vec{P}_\nu$ and $\vec{P}_\rho$ are overall c.m. system momenta of incident gamma and outgoing di-pion), and X chosen to make right-handed Cartesian system.

The helicity frame is the same as the Jackson except that the Z direction is the direction of flight of the di-pion instead of the gamma.

The angular distribution is then given in terms of the meson-spin density-matrix elements $\rho_{mm'}$:

$$W(\theta, \phi) = \frac{3}{4\pi} \left[\rho'_{11} + (1 - 3\rho_{11}) \cos^2 \theta - \rho_{1-1} \sin^2\theta \cos 2\phi - 2\mathrm{Re}\ \rho_{10} \sin 2\theta \cos \phi \right]$$

where $2\rho_{11} + \rho_{00} = 1$.

The Jackson system is well suited to studying exchange processes in the t channel. The interpretation is particularly simple when a single particle is involved; for example, single-pion exchange gives a $\sin^2\theta_J$ distribution. The data plotted as a function of cos θ_J in Fig. 30 are certainly not of the simple $\sin^2\theta_J$ form.

The angular distributions in the helicity system are given in Fig. 31. For events in the range 4 to 16 GeV, we obtain a value of ρ_{11}^H compatible with its

maximum value 1/2 (a $\sin^2 \theta_{11}$ distribution):

$$\rho_{11}^{H} = 0.53 \pm 0.2 \qquad 4 < k < 16 \text{ GeV} .$$

The off-diagonal matrix elements do not appear in the angular distribution after integration over ϕ, and $\rho_{00} = (1 - 2\rho_{11})$ is evidently near zero. Our results, which are dominated by low-momentum-transfer events, are compatible with the ρ^0 behaving as a photon.

Söding[12] has suggested that the observed asymmetry in di-pion mass may result from an interference by terms in which a pair of pions is coupled to the photon, and one of these rescatters from the proton, as shown in the inset in Fig. 32a. In applying this suggestion, we have used an analytic expression for the diffractive production of the ρ given by A. Krass[12] from the strong absorption model (SAM). There are problems of double counting in this method which are not well understood. In this calculation the same scattering cross section was used for π^+ and π^-. The asymmetry of the resonant peak is reproduced by this interference. Its sense is fixed by the relative sign of the interference, which is chosen by comparison with the experimental spectrum. The curve obtained with a ρ mass of 765 MeV and a ρ width of 125 MeV is shown in Fig. 32a, where the strength of the resonance was treated as a free parameter. A reasonable fit is also obtained with the Orsay values of 772 MeV for the ρ mass and 113 MeV for the ρ width. No other parameters were adjusted. The model predicts an effect which we have observed experimentally that the slope of $\frac{d\sigma}{dt}$ decreases with the mass of ρ. This is shown in Fig. 32b. The model predicts that the interference will have little effect on the decay matrix elements.

3. The Reaction $\gamma p \to \pi^- \Delta^{++}$

From the fraction of Δ^{++} in the $p\pi^+$ spectrum, we can calculate cross sections for $\gamma p - \pi^- \Delta^{++}$ in various photon-energy intervals. Our measurements given below are compatible with those of DESY,[10] CEA[11] and of SLAC.[13] They indicate that $E_\gamma^2 \sigma$ is approximately constant as expected qualitatively for processes involving meson exchange in the t channel.

Photon Energy E_γ GeV	$\sigma(\gamma p \to \pi^- \Delta^{++})$ μb	$\langle E_\gamma^2 \sigma \rangle$ μb GeV^2
2 - 4	3.5 ± 1.2	25 ± 8.5
4 - 8	0.8 ± 0.4	33 ± 11
8 - 16	0.3 ± 0.2	34 ± 23

B. The Reaction $\gamma p \to K^+ K^- p$

Identification of the reaction $\gamma p \to K^+ K^- p$ was difficult since our sample of 3-prong events contained about 25 times as many pion as kaon final states. The basic fitting criterion was a χ^2 of less than 30. When both pion and kaon hypotheses were possible, the fit with the lowest χ^2 was normally chosen. In most cases, however, ionization data provided an effective selection criterion since the alternative solutions for 1(+) 2(-) 3(+) were $p\pi^-\pi^+$ and K^+K^-p or $\pi^+\pi^-p$ and pK^-K^+. After a particular assignment was made, its validity was tested by computing M_γ^2. All of the events satisfying $\chi_K^2 < 30$ are shown in Fig. 33; those also satisfying $\chi_\pi^2 < 30$ have a peak near $M_\gamma^2 = 0$ when $\chi_K^2 < \chi_\pi^2$ and no peak when $\chi_K^2 > \chi_\pi^2$.

Figure 34 is a mass spectrum for K^+K^-. In the region of the ϕ(1.010 - 1.030 GeV), eight events satisfy only a kaon solution, while one event also satisfies a pion solution, but with a higher χ^2. We evaluated the ϕ cross section by making the usual corrections for geometry and by assuming a

background of one event in the 20-MeV interval at the ϕ mass. A branching ratio of 0.47 for K^+K^- to all ϕ decay modes was used. The cross section between 2 and 16 GeV was then 0.55 ± 0.20 μb.

Figure 35 gives the differential cross section $d\sigma/dt'$ as a function of the momentum transfer t'. A fit of the form $A e^{-Bt'}$ gives the values

$$A = (3.4 \pm 1.8) \ \mu b/GeV$$

$$B = (6.3 \pm 2.5) \ GeV^{-2} \ .$$

These results agree with bubble chamber measurements by DESY,[10] and with counter experiments by DESY-MIT[14] and by SLAC[15]: They yield a t dependence much weaker than that for ρ production.

C. Reactions With More Than One Pair of Pions

1. The Reaction $\gamma p \rightarrow \pi^+\pi^-\pi^+\pi^- p$

The 3-C events satisfying the hypothesis $\gamma p \rightarrow \pi^+\pi^-\pi^+\pi^- p$ are plotted in Fig. 36. The cross section increases with photon energy K up to 6 μb at 5 GeV, then decreases slowly to about 2 μb at 15 GeV. In Fig. 36 our results together with those from the DESY and SLAC bubble chambers are compared with the predictions of the Satz[16] model. This calculation uses vector dominance and the quark model plus πp and pp inelastic scattering measurements to predict γp cross sections. There is some possible disagreement in the form of a greater peaking in the 5-GeV region.

The mass spectra for this reaction show two principal characteristics: the production of the Δ^{++} (1236 MeV) is demonstrated in the $p\pi^+$ mass plot of Fig. 37, and ρ^0 production is evident in the $\pi^+\pi^-$ mass plot of Fig. 39a. The various 3π spectra and the 4π spectrum of Fig. 38 show no significant structure at our present statistical level; in particular, if one considers events leading to the formation of Δ^{++}, the mass spectrum of the remaining 3π's shows no indication of states such as A_1 or A_2. The 4π spectrum is interesting since it could

show a hypothetical "ρ'," a new vector meson or a Regge recurrance of the ρ (for example $J^P = 3^-$) made by diffraction. No significant evidence for such states is seen with our present statistical accuracy.

2. The Reaction $\gamma p \rightarrow \rho^o \pi^+ \pi^- p$

We have already mentioned the ρ^o peak in the $\pi^+\pi^-$ mass plot of Fig. 39a. Its interpretation is made difficult by the number of combinations. The $\pi^+\pi^+$ and $\pi^-\pi^-$ mass plot of Fig. 39b gives an indication of the background present in Fig. 39a while providing no evidence for any state of I = 2. The cross section for ρ^o production versus photon energy is given in Fig. 39c.

3. The Reaction $\gamma p \rightarrow \pi^+\pi^-\pi^+\pi^-\pi^+\pi^- p$

We have found 23 events with six charged pions in the final state. It is especially difficult to interpret the various mass spectra in this case because of the large number of combinations possible. In the $\pi^+\pi^-$ spectrum, for example, there are nine combinations. Thus we give only the cross sections for the entire channel; these may be compared with the prediction of Satz[16] who obtains $\sim 1\ \mu b$ in the range 6 - 10 GeV.

Photon Energy E_γ GeV	$\sigma(\gamma p \rightarrow \pi^+\pi^-\pi^+\pi^-\pi^+\pi^- p)$ μb
6 - 10	0.93 ± 0.3
10 - 16	0.90 ± 0.3

D. Reactions With at Least One π^o

In dealing with events that did not have a 3-C solution, we carried out kinematic fits assuming there was one missing π^o. Weak constraints were imposed by requiring that the missing neutral have positive energy and that the total energy be less than the peak bremsstrahlung energy 16 GeV. In about 20% of the events, ionization information permitted an identification of the proton. Clearly any mass plot for these data will have large backgrounds; the

proton is not positively identified in most cases, and in many cases the missing neutral is a neutron so that all charged particles are pions. Furthermore, in the 3-prong sample there are about three times as many events with more than one π^o missing as with a single π^o missing.[9]

The narrow width of the ω(783 MeV) and the low background at the beginning of the three pion phase space, make possible an investigation of the reactions $\gamma p \to \omega p$, $\omega \to \pi^+ \pi^- \pi^o$. The $\pi^+ \pi^- \pi^o$ mass plot of Fig. 40 shows an ω peak, with data separated into intervals of 2 - 16 GeV and 5 - 16 GeV. In calculating cross sections we have estimated the background phenomenologically with a polynomial fit between 0.70 and 0.95 GeV. The peak itself was assumed to be Gaussian; theoretically one should fold a Gaussian resolution with a Breit-Wigner resonance shape, but in our case the resolution was broader than the natural resonance width. Specifically, the standard deviation of the fitted Gaussian was 25 MeV between 2 and 5 GeV and 20 MeV between 5 and 16 GeV. (The natural width of the ω is 12.6 MeV.)

Using a branching ratio of 90% for $\omega \to \pi^+ \pi^- \pi^o$, we obtained the following cross sections:

Photon Energy E_γ GeV	$\sigma(\gamma p \to \omega p)$ μb
2 - 5	3.9 ± 0.9
5 - 16	2.6 ± 0.7

The differential cross section $d\sigma/dt'$ is plotted in Fig. 41 for the two energy regions, fitting these with the usual exponential $Ae^{-Bt'}$.

Photon Energy E_γ GeV	A μb/GeV^2	B GeV^{-2}
2 - 5	35 ± 12	9.0 ± 2.6
5 - 16	25 ± 10	9.5 ± 2.3

We have used a phenomenological form suggested by DESY to extract the diffractive part of the cross section. Here production is split between a one-pion-exchange term and a diffractive term. (The amplitudes do not interfere.)

$$\sigma(\gamma p \rightarrow \omega p) = C_{ope} E^{-1.6} + \sigma_{diff.}$$

The experimental data and the diffractive part are shown in Fig. 42.

E. Vector Dominance Model

It is possible to test the vector-dominance model[17] by using it, our data on ρ, ω, and ϕ photoproduction, and recent measurements on photon vector meson coupling constants to derive the total photoproduction cross section. This cross section can then be compared with recent measurements of the total photoproduction cross section.

The vector dominance model (VDM) permits one to write the following relation between amplitudes[17]:

$$A(\gamma p \rightarrow \gamma p) = \sum_{V'} \frac{e}{f_{V'}} A(\gamma p \rightarrow V'_{tr} p)$$

where V', V stands for Vector meson,

V_{tr} means the transverse polarization states of V,

and $\frac{em_V^2}{f_V}$ is the vector meson photon coupling constant.

From this equation and the optical theorem one can derive a relation for the total γp cross section:

$$\sigma_T(\gamma p) \equiv 4\pi \sum_V \frac{e}{f_V} \sqrt{\frac{d\sigma}{dt}(\gamma p \rightarrow V_{tr} p)_{t=0} \frac{1}{1+\alpha_V^2}}$$

where

$$\alpha_V = \left.\frac{\text{Re } A(\gamma p \rightarrow V_{tr} p)}{\text{Im } A(\gamma p \rightarrow V_{tr} p)}\right|_{t=0}$$

allows for a possible contribution of a real part of the mostly diffractive amplitudes.

We can now test VDM by evaluating $\sigma_T(\gamma p)$ using our measured data and recent measurements on the coupling constants,[18] and by comparing the result with independent direct measurements of $\sigma_T(\gamma p)$.[9,10,11]

There is some uncertainty about α_V. Experimental information is available only for α and indicates that α^2 is less than 10% and consistent with zero.[14] Assuming $\alpha_V^2 = 0$ we obtain $\sigma_T(\gamma p)$ from the equation above accurate to about 20%, (the isoscalar amplitudes contribute in total only this amount).

Table III shows the relative contributions of ρ^0, ω, and ϕ to $\sigma_T(\gamma p)$. The comparison with the directly measured total photon cross section is shown in Fig. 43. The agreement appears to be very good and permits one to conclude that VDM is valid to $\pm$ 20% in this process.

Using VDM and our measured data we can also obtain information on the high energy total cross section for (Vp) reactions.

The optical theorem and the VDM equation

$$A(\gamma p \rightarrow Vp) = \sum_{V'} \frac{e}{f_{V'}} A(V'_{tr} p \rightarrow Vp)$$

yield the following relation[17] for the diffractive part of $\frac{d\sigma}{dt}(\gamma p \rightarrow Vp)$:

$$\left.\frac{d\sigma}{dt}(\gamma p \rightarrow Vp)\right|_{t=0}^{\text{diff.}} = \left(\frac{e}{f_V}\right)^2 \frac{1}{16\pi} \sigma_T^2(Vp)$$

where we assumed

1. Only 'elastic' amplitudes V = V' contribute.

and

2. Re $A(Vp \rightarrow Vp) \approx 0$.

Although for the reaction $\gamma p \rightarrow p\rho^0$ all experimental evidence suggests a nearly pure diffractive process, a nondiffractive contribution in ω photoproduction is to be expected, and we use the diffractive portion as obtained at the end of the previous section. For ϕ photoproduction we assume a pure diffraction process. The present experimental data give no information on a possible real part of the amplitude. The results from the evaluation of $\sigma_T(Vp)$ are listed in Table IV.

The ρ^0, ω and ϕ proton total cross sections are in agreement with theoretical predictions from the Quark[19] model and from SU(3) with universality and symmetry breaking in the Pomeranchuk trajectory.[20] They are also in agreement with published cross sections at lower energy (3-5 GeV) obtained from photoproduction of ρ^0 and ϕ on complex nuclei,[14] but disagree with more recent measurements by McClellan et al. and Bulos et al.[21]

ACKNOWLEDGMENTS

This has been the first experimental use of this large streamer chamber. The success of the project was due to the work in design, construction, operation, and analysis of a large group of people in addition to those mentioned in the title page. Dr. R. Zdanis helped in the run and organization of the early data analysis, Dr. A. Krass provided stimulating and helpful theoretical discussion, and L. Schwarcz directed many phases of the project. Among those whose help has also been of great value are the following: M. Aleksandrov, R. Bell, B. Bertolucci, R. Ching, D. Danielson, J. Jonson, D. Lebet, V. Lee, R. Leedy, M. Lieber, E. Maninger, E. McNerney, A. Omahen, F. Plunder, T. Pulliam, W. Quiett, M. Schlesinger, G. Schultz, F. Shuster, P. Thingstad, and W. Wadley. In addition, it is a pleasure to thank the accelerator and computer operating groups and the machine shops for their assistance.

REFERENCES

1. A. I. Alikhanian, T. L. Asatiani, E. M. Matevosyan, and R. O. Sharkhatunian, Phys. Letters 4, 295 (1963); A. I. Alikhanian, T. L. Asatiani, and E. M. Matevosyan, Soviet Phys. JETP 17, 522 (1963); A. I. Alikhanian, Loeb Lecture Notes, Harvard University, Cambridge, Massachusetts (1965) (unpublished).
2. V. A. Mikhailov, V. N. Roinishvili, and G. E. Chikovani, Soviet Phys., JETP 18, 561 (1964); G. E. Chikovani, V. N. Roinishvili, and V. A. Mikhailov, Soviet Phys., JETP 19, 833 (1964).
3. M. Davier, I. Derado, D. Drickey, D. Fries, R. Mozley, A. Odian, F. Villa, D. Yount, and R. Zdanis, Phys. Rev. Letters 21, 841 (1968) (ρ^0 production); M. Davier, I. Derado, D. Drickey, D. Fries, R. Mozley, A. Odian, F. Villa, and D. Yount, Phys. Letters 28B, 619 (1969) (ω^0, ϕ^0 production).
4. J. D. Craggs and J. M. Meek, High Voltage Laboratory Technique, (Butterworths, London, 1954).
5. Blumlein "voltage-doubler circuits" are discussed by O. L. Ratsey, J. Inst. Elect. Engrs. 93, 245 (1946); by K. J. R. Wildinson, J. Inst. Elect. Engrs. 93, 1090 (1946); and by Craggs and Meek, Ref. 4. See also J. L. Brewster, F. M. Charbonnier, L. F. Garrett, K. W. Riegelmann, and J. K. Trolan, "Design Studies for Ultra-Fast, Low-Impedance, High-Peak-Power Pulsed Systems," Technical Report No. AFWL-TR-65-21, Air Force Weapons Laboratory, Kirkland Air Force Base, N.M. (1965).
6. F. Bulos, A. Odian, F. Villa, and D. Yount, Stanford Linear Accelerator Center Report No. 74, 1967 (unpublished); F. Bulos, "Streamer Wide Gap Spark Chamber," SLAC Internal Report TN-64-73 (1964); F. Bulos, A. Boyarski, R. Diebold, A. Odian, B. Richter, and F. Villa, IEEE Trans. Nucl. Sci.

NS-12 (No. 4), 22 (1965); F. Bulos, A. Boyarski, R. Diebold, A. Odian, B. Richter, and F. Villa, "Streamer Chamber Development," Proceedings of the 1966 International Conference on Instrumentation for High Energy Physics, Stanford Linear Accelerator Center, Stanford, California, September 9-10, 1966, p. 49; F. Villa, "Two-Meters SLAC Chamber," Proceedings of the International Colloqium on Nuclear Electronics, Versailles, France, September 10-13, 1968, Vol. III, p. 7-11.

7. D. Yount, Nucl. Instr. and Methods 52, 1 (1967); and p. 75 of the Proceedings of the Symposium on Beam Intensity Measurement, Daresbury England, 22-26 April, 1968.

8. SYBIL: D. Fries, SLAC Report No. 103, 1969 (unpublished), see also I. Derado and D. Fries, Nucl. Instr. and Methods 67, 109, (1969); TEUTA: I. Derado and R. Leedy, SLAC Report No. 72, SIMULATE: R. Zdanis, private communication, see also F. Bomse et al., Phys. Rev. 158, 1281 (1967); MURTLEBERT: J. Friedman, UCRL Report No. AGM-P156, (1966) (unpublished); ISIS: M. Davier, "Photoproduction of Vector Mesons Between 2 and 16 GeV," Doctoral Dissertation, University of Paris, France (1969). A more complete description of event analysis will be published.

9. J. Ballam et al., Phys. Rev. Letters 21, 1541 (1968) (partial cross sections up to 12 GeV); Phys. Rev. Letters 21, 1544 (1968) (γp total cross sections); Y. Eisenberg et al. (Weizmann Institute), Phys. Rev. Letters 22, 669 (1969) (partial cross sections at 4.3 GeV).

10. Aachen-Berlin-Bonn-Hamburg-Heidelberg-Munchen Collaboration: Nuovo Cimento 41A, 270 (1966) (first results); Phys. Letters 23, 707 (1966) (Δ^{++}(1236) production); Nuovo Cimento 46A, 795 (1966) (ω, ϕ, η, X^0, production); Nuovo Cimento 48A, 262 (1967) (ρ production); Nuovo Cimento 49A, 337 (1967) (ρ production); Phys. Letters 27B, 54 (1968) (vector-meson production);

Phys. Rev. 175, 1669 (1968) (meson and baryon resonances, first of two final reports); DESY 68/8 (May 1968) to be published in Phys. Rev. (γp total cross sections).

11. Cambridge Bubble Chamber Group: Phys. Rev. Letters 13, 636 (1964) and Phys. Rev. Letters 13, 640 (1964) (first results); Phys. Rev. 146, 994 (1966) (ρ production); Phys. Rev. 155, 1468 (1967) (ω production); Phys. Rev. 155, 1477 (1967) (cross sections); Phys. Rev. 163, 1510 (1967) ($\Delta^{++}(1236)$ production); Phys. Rev. 169, 1081 (1968) (multipion production).
12. J. D. Jackson, Nuovo Cimento 34, 1644 (1964) and H. Pilkuhn, The Interactions of Hadrons, North Holland, Amsterdam, 1967 (Breit-Wigner shape and angular distributions); M. Ross and L. Stodolsky, Phys. Rev. 149, 1172 (1966) (ρ mass asymmetry); P. Söding, Phys. Letters 19, 702 (1966) (interfering dipion background); A. Krass, Phys. Rev. 159, 1496 (1967) (diffraction production in the strong absorption model).
13. A. Boyarski et al., Phys. Rev. Letters 22, 148 (1969).
14. J. G. Asbury et al., Phys. Rev. Letters 19, 865 (1967) (ρ production on complex nuclei); Phys. Rev. Letters 19, 869 (1967) ($\rho^0 \rightarrow e^+e^-$, $\gamma\rho$ coupling constant); Phys. Rev. Letters 20, 227 (1968) (tests of vector dominance); U. Becker, Phys. Rev. Letters 21, 1504 (1968) ($\phi^0 \rightarrow e^+e^-$, $\gamma\phi$ coupling constants).
15. W. G. Jones et al., Phys. Rev. Letters 21, 586 (1968).
16. H. Satz, Phys. Letters 25B, 27 (1967); Phys. Rev. Letters 19, 1453 (1967).
17. J. J. Sakurai, Ann. Phys. (N.Y.) 11, 1 (1960); N. M. Kroll, T. D. Lee, and B. Zumino, Phys. Rev. 157, 1376 (1967); J. Joos, Acta Physica Austriaca Supplementum IV (1967).

18. V. L. Auslender et al., Phys. Letters 25B, 433 (1967(ρ^o production); J. E. Augustin, Phys. Letters 28B, 503 (1969)(comparison with vector dominance); Phys. Letters 28B, 508 (1969)(ρ^o production); Phys. Letters 28B, 513 (1969)(ω^o production); Phys. Letters 28B, 517 (1969)(ϕ^o production).

19. H. Joos, Phys. Letters 24B, 103 (1967).

20. M. Davier, Phys. Rev. Letters 20, 952 (1968).

21. G. McClellan et al., Phys. Rev. Letters 22, 377 (1969) and F. Bulos et al., Phys. Rev. Letters 22, 490 (1969). We have used the coupling constants of the colliding beam measurements (Ref. 18), but we are aware of the apparent discrepancy between those values and the values given by the references quoted here. In particular, the photoproduction total cross sections predicted by vector dominance from our data would be significantly lower than the direct experimental values if the constants of McClellan et al., or Bulos et al., were used.

TABLE I

Rho Mass Fits

Photon Energy (GeV)	Fit A m_ρ (MeV)	Fit B m_ρ (MeV)	Fit C m_ρ (MeV)	Fit C Γ_ρ (MeV)
2 - 4	725 ± 13	758 ± 4	747 ± 6	80 ± 23
4 - 8	711 ± 24	766 ± 11	754 ± 9	111 ± 41
8 - 16	710 ± 21	770 ± 23	747 ± 47	219 ± 195

TABLE II

Rho Momentum Transfer Distributions

$\Delta t'$ (GeV^2)	$\frac{d\sigma}{dt}$ ($\mu b/GeV^2$) 2 - 4 GeV	$\frac{d\sigma}{dt}$ ($\mu b/GeV^2$) 4 - 8 GeV	$\frac{d\sigma}{dt}$ ($\mu b/GeV^2$) 8 - 16 GeV
0 - 0.05	$\geq 78 \pm 13$	$\geq 72 \pm 13$	$\geq 50 \pm 20$
0.05 - 0.1	87 ± 15	74.4 ± 14	68.5 ± 23
0.1 - 0.2	63 ± 8.3	30.8 ± 5.8	34 ± 9
0.2 - 0.3	16.8 ± 4.4	17.9 ± 4.8	9.9 ± 5
0.3 - 0.4	12.9 ± 3.2	7.1 ± 2.9	3 ± 2.1
0.4 - 0.5	3.2 ± 2.2	1.8 ± 1.2	-
A ($\mu b/GeV^2$)	178 ± 33	133 ± 34	152 ± 65
B (GeV^{-2})	8.3 ± 1.0	8.9 ± 1.5	11.1 ± 2.8

TABLE III

VDM Calculation of $\sigma_T(\gamma p)$ (in μb)

	2 - 4	4 - 8	8 - 16
ρ^o	110 ± 16	95.5 ± 13	102^{+22}_{-26}

	2 - 5	5 - 16
ω	$18.3^{+3.4}_{-3.7}$	$15.5^{+3.}_{-3.4}$

	2 - 16
ϕ	$7.1^{+1.5}_{-1.9}$

	2 - 4	4 - 8	8 - 16
$\sigma_T(\gamma p)$	135.6 ± 16	119.4 ± 14	124.5^{+22}_{-26}

TABLE IV

Cross Sections and Differential Cross Section Parameters for Photoproduction of ρ^o, ω and ϕ.

V	Photon Energy E_γ Interval $(\overline{E}_\gamma)$ (GeV)	$\gamma p \rightarrow Vp$			$e^+e^- \rightarrow V$	$\sigma_{e\ell}(Vp)$	$\sigma_T(Vp)$
		σ (μb)	$\left(\frac{d\sigma}{dt}\right)_{t=t_{min}}$ (μb/GeV^2)	B_V (GeV^{-2})	$\frac{f_V^2}{4\pi}$	(mb)	(mb)
ρ	8 - 16 (11.5)	13.8 ±2.9	152 ± 65	11.1 ± 2.8	2.10 ± 0.11	3.86± 0.6	29.4± 6
ω	5 - 16 (9.5)	2.6 ± 0.7	25 ± 10	9.5 ± 2.3	14.8 ± 2.8	3.84± 1.2	27 ± 8
ϕ	2 - 16 (6.5)	.61 ± 0.24	3.9 ± 2.1	6.3 ± 2.5	11.0 ± 1.6	.91± 0.6	10.7± 3.8

FIGURE CAPTIONS

1. Side view of the SLAC 2.2-m streamer chamber and magnet.
2. Top view of the SLAC 2.2-m streamer chamber and magnet.
3. Photograph of the streamer chamber installed in the magnet showing two foam cells between three horizontal electrodes.
4. Photograph of a foam cell used in the 2.2-m streamer chamber.
5. Typical 3-prong event followed by an electron-positron pair.
6. Typical 5-prong event with a flare obscuring the vertex.
7. Magnetic field distribution in the 450-ton, 5.8-MW streamer chamber magnet.
8. Photon beam layout.
9. Energy spectrum of pairs produced in the 2.2-m streamer chamber.
10. Distribution of standard deviations for fitted 3-prong events.
11. Distribution of 3-prong event vertices perpendicular to the beam direction.

12a,b,c. Separation of positron-electron pairs in a sample of apparent 5-prong events. The full sample is shown in a, while b and c indicate the sample still identified as 5-prongs after events having tracks nearly parallel to the beam have been removed.

13. Number of events versus the calculated mass-squared of the incident photon.
14. Distribution of events for which only one track intercepted the trigger counters (indicated by the two rectangular regions).
15. Detection efficiency versus dip angle λ in degrees for streamer chamber, tracks.
16. Number of events versus detection efficiency for counters, streamer chamber, and total system. The acceptance histograms indicate that most event types were detected with high efficiency by the counters, with about 50% efficiency by the streamer chamber, and with an overall efficiency of about 50%.

17. Acceptance histograms for different energy intervals.

18. Total acceptance versus energy for the reactions $\gamma p \rightarrow \pi^+ \pi^- p$ and $\gamma p \rightarrow \pi^+ \pi^- \pi^+ \pi^- p$.

19. Generated Monte-Carlo events compared with accepted Monte-Carlo events as a function of t.

20. Counter acceptance versus dipion mass.

21. Fraction of Monte-Carlo events accepted versus decay angle θ_H in the helicity system.

22. Cross sections versus energy for the reaction $\gamma p \rightarrow \pi^+ \pi^- p$.

23. Invariant mass distribution for $(p\pi^+)$ in the reaction $\gamma p \rightarrow \pi^+ \pi^- p$.

24. Invariant mass distribution for $(p\pi^-)$ in the reaction $\gamma p \rightarrow \pi^+ \pi^- p$.

25. Invariant mass distribution for $(\pi^+ \pi^-)$ in the reaction $\gamma p \rightarrow \pi^+ \pi^- p$.

26a, b, c. Corrected $\pi^+ \pi^-$ mass plots in three energy intervals. The solid curves are from Table I, Fit A.

27. Fraction of ρ's in the sample $\gamma p \rightarrow \pi^+ \pi^- p$ versus energy.

28. Cross sections for ρ^o photoproduction versus energy.

29a, b, c. Differential cross sections $d\sigma/dt'$ for ρ^o production as a function of momentum transfer t'.

30. Angular distributions for ρ^o decay in the Jackson system.

31. Angular distribution for ρ^o decay in the helicity system.

32a, b. Corrected $\pi^+ \pi^-$ mass plot (a) fitted with resonant ρ production and an interfering 2π background. The variation of the slope parameter B for $d\sigma/dt$ is shown as a function of ρ mass in (b).

33. Photon mass-squared distributions for events satisfying kaon solutions with χ^2 less than 30.

34. $K^+ K^-$ mass spectrum in the sample $\gamma p \rightarrow K^+ K^- p$.

35. Differential cross sections $d\sigma/dt'$ for ϕ production as a function of momentum transfer t'.

36. Cross sections versus energy for the reaction $\gamma p \rightarrow \pi^+\pi^-\pi^+\pi^- p$.

37. Mass spectrum for $p\pi^+$ in the reaction $\gamma p \rightarrow \pi^+\pi^-\pi^+\pi^- p$.

38. Mass spectrum for $\pi^+\pi^-\pi^+\pi^-$ in the reaction $\gamma p \rightarrow \pi^+\pi^-\pi^+\pi^- p$.

39a, b, c. Mass spectra for $\pi^+\pi^-$ (a) and for $\pi^+\pi^+$ and $\pi^-\pi^-$ (b) in the reaction $\gamma p \rightarrow \pi^+\pi^-\pi^+\pi^- p$. The cross section versus photon energy for the reaction $\gamma p \rightarrow \rho^0\pi^+\pi^- p$ is given in c.

40. Comparison of the mass spectra for $\pi^+\pi^-\pi^0$ in the intervals 2-16 GeV and 5-16 GeV in the reaction $\gamma p \rightarrow p\pi^+\pi^-\pi^0$.

41. Differential cross section $d\sigma/dt'$ versus t' for the reaction $\gamma p \rightarrow \omega p$.

42. Separation of the one-pion-exchange and diffractive contributions to the reaction $\gamma p \rightarrow \omega p$.

43. Comparison of experimental total cross sections with those derived from the vector dominance model using data from the SLAC streamer chamber.

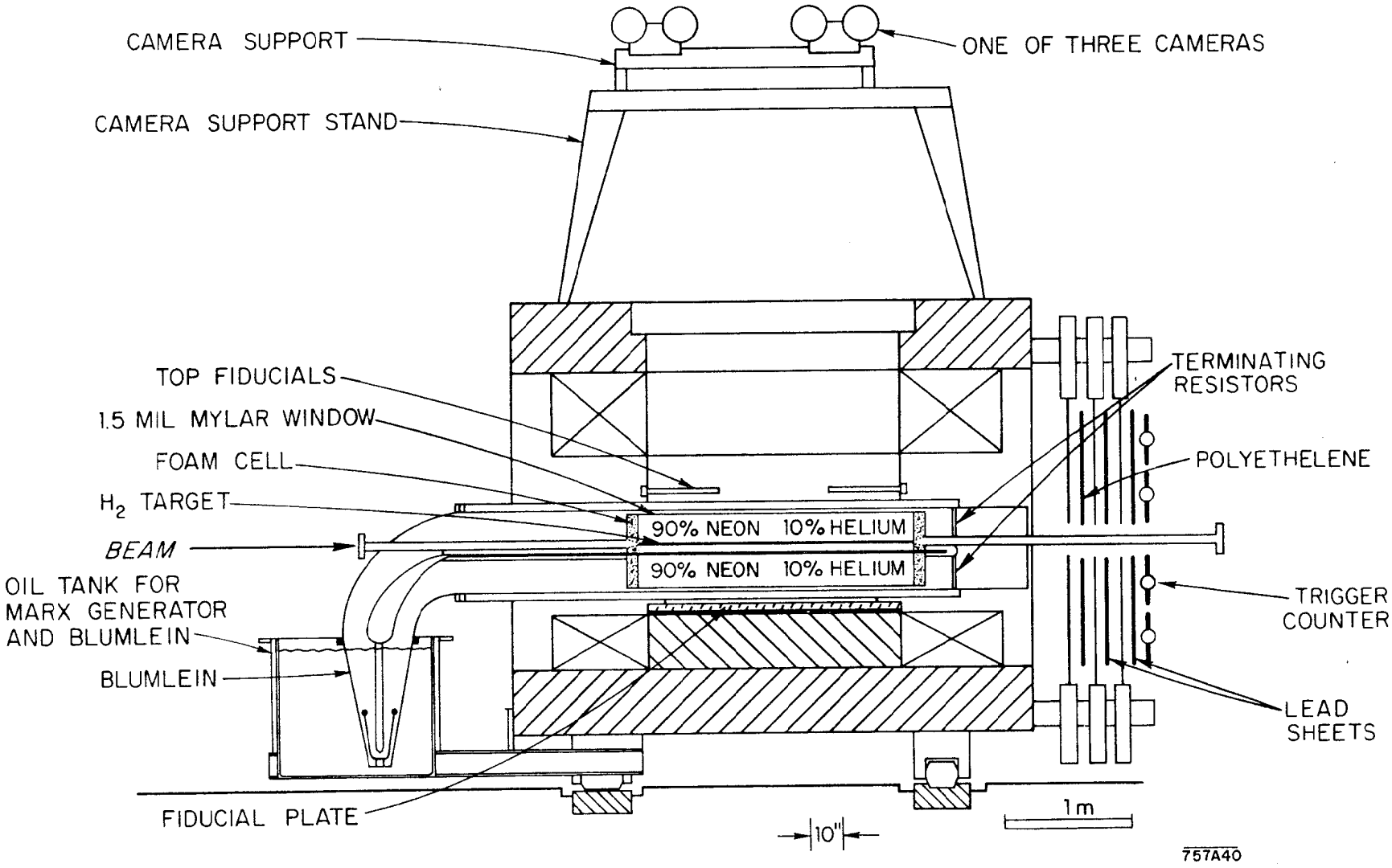
CAMERA SUPPORT
ONE OF THREE CAMERAS
CAMERA SUPPORT STAND
TOP FIDUCIALS
1.5 MIL MYLAR WINDOW
FOAM CELL
H_2 TARGET
BEAM
OIL TANK FOR MARX GENERATOR AND BLUMLEIN
BLUMLEIN
FIDUCIAL PLATE
90% NEON 10% HELIUM
90% NEON 10% HELIUM
TERMINATING RESISTORS
POLYETHELENE
TRIGGER COUNTER
LEAD SHEETS
10"
1m
757A40

Fig. 1

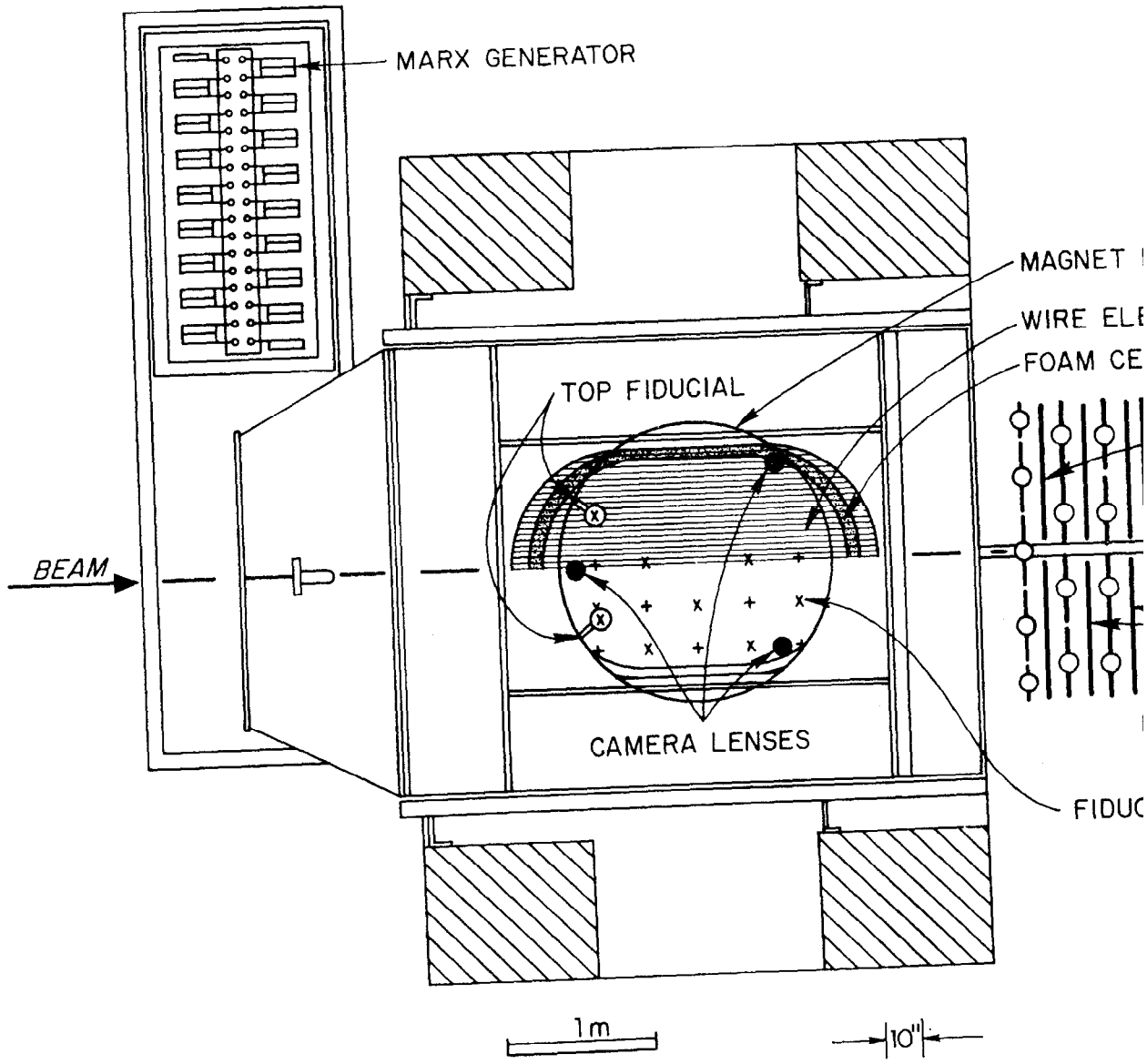
MARX GENERATOR
MAGNET
WIRE ELE
FOAM CE
TOP FIDUCIAL
BEAM
CAMERA LENSES
FIDUC
1m
10"

Fig. 2

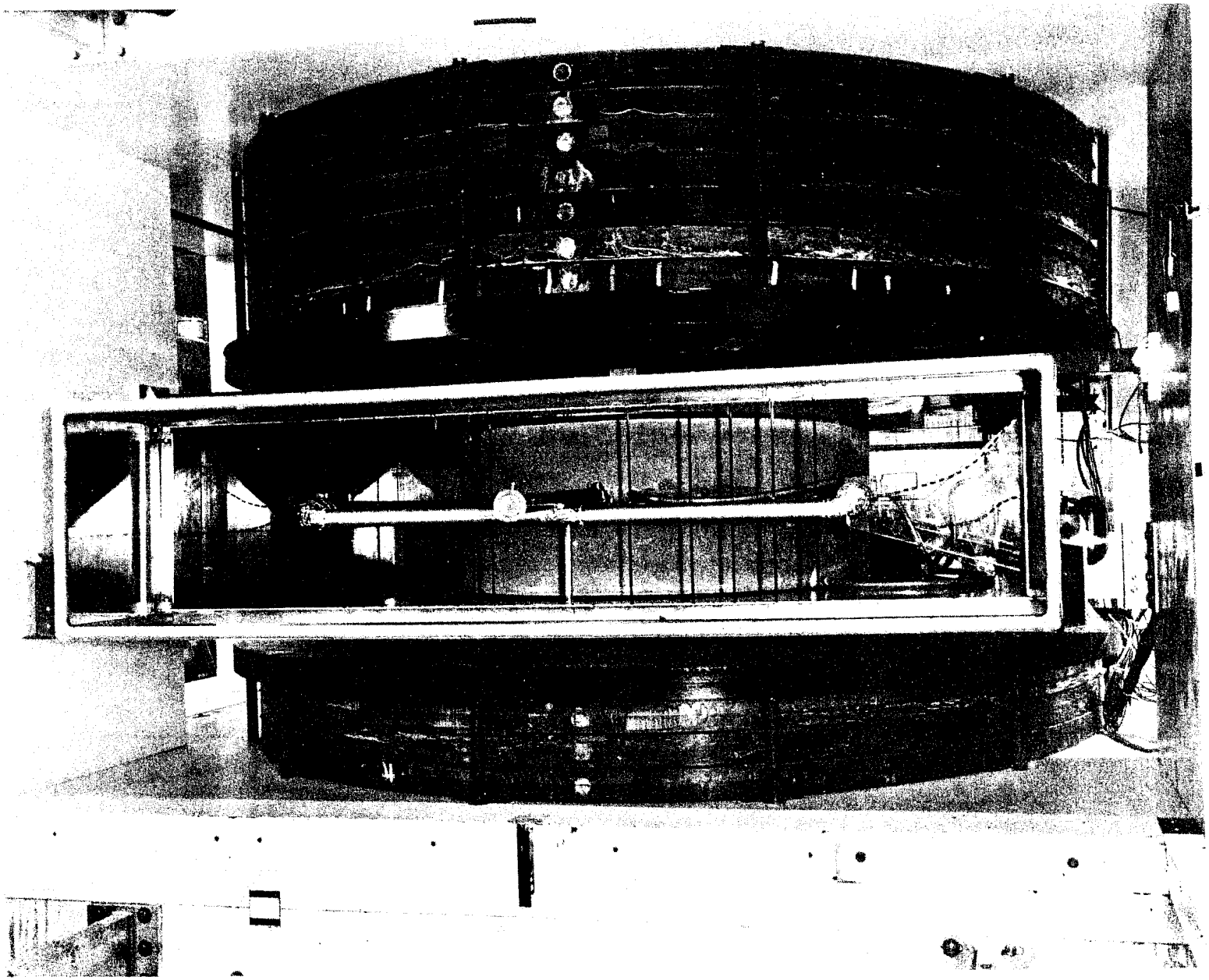

757A51

Fig. 3

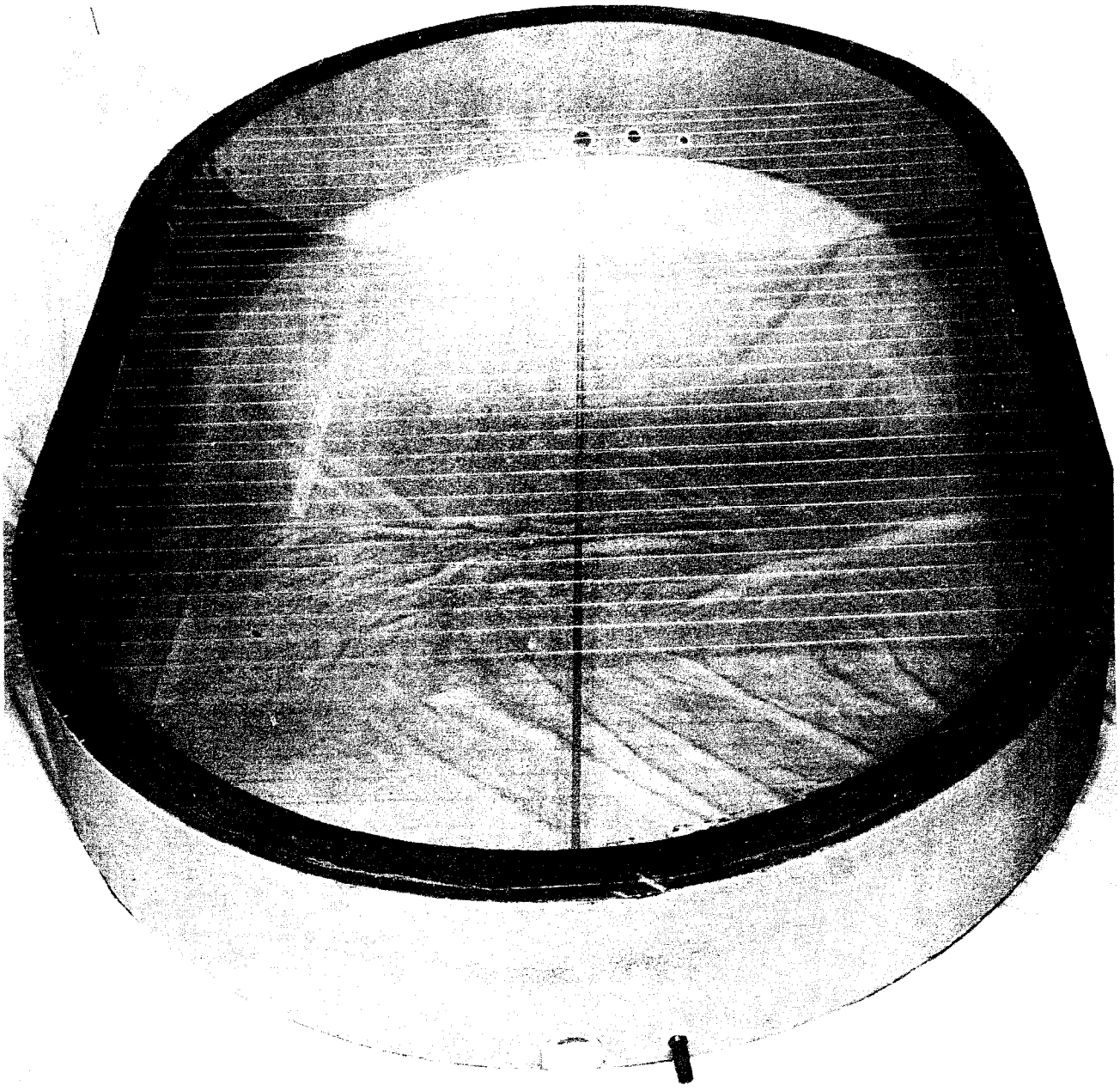

757A52

Fig. 4

Fig. 5

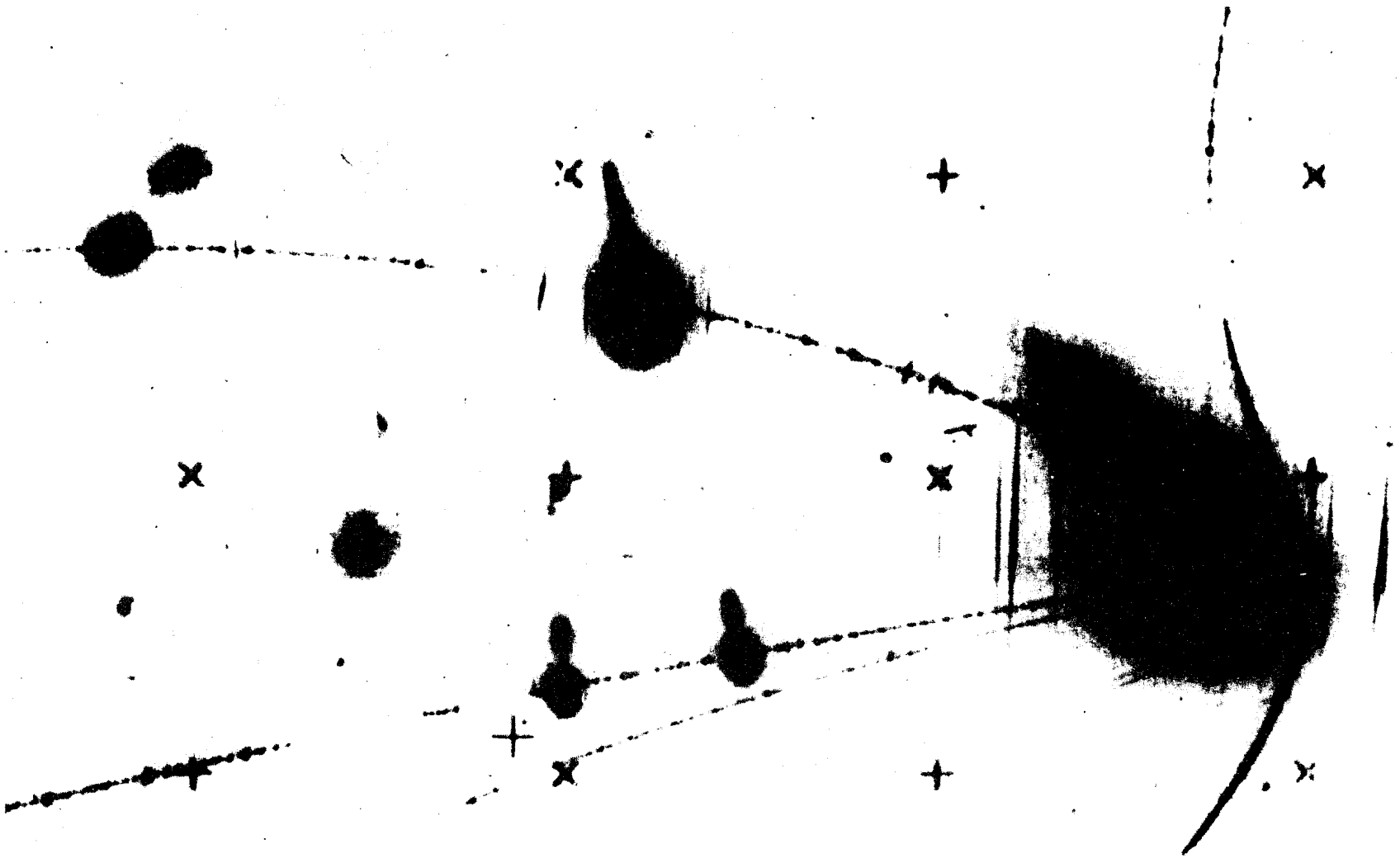

Fig. 6

1276A30

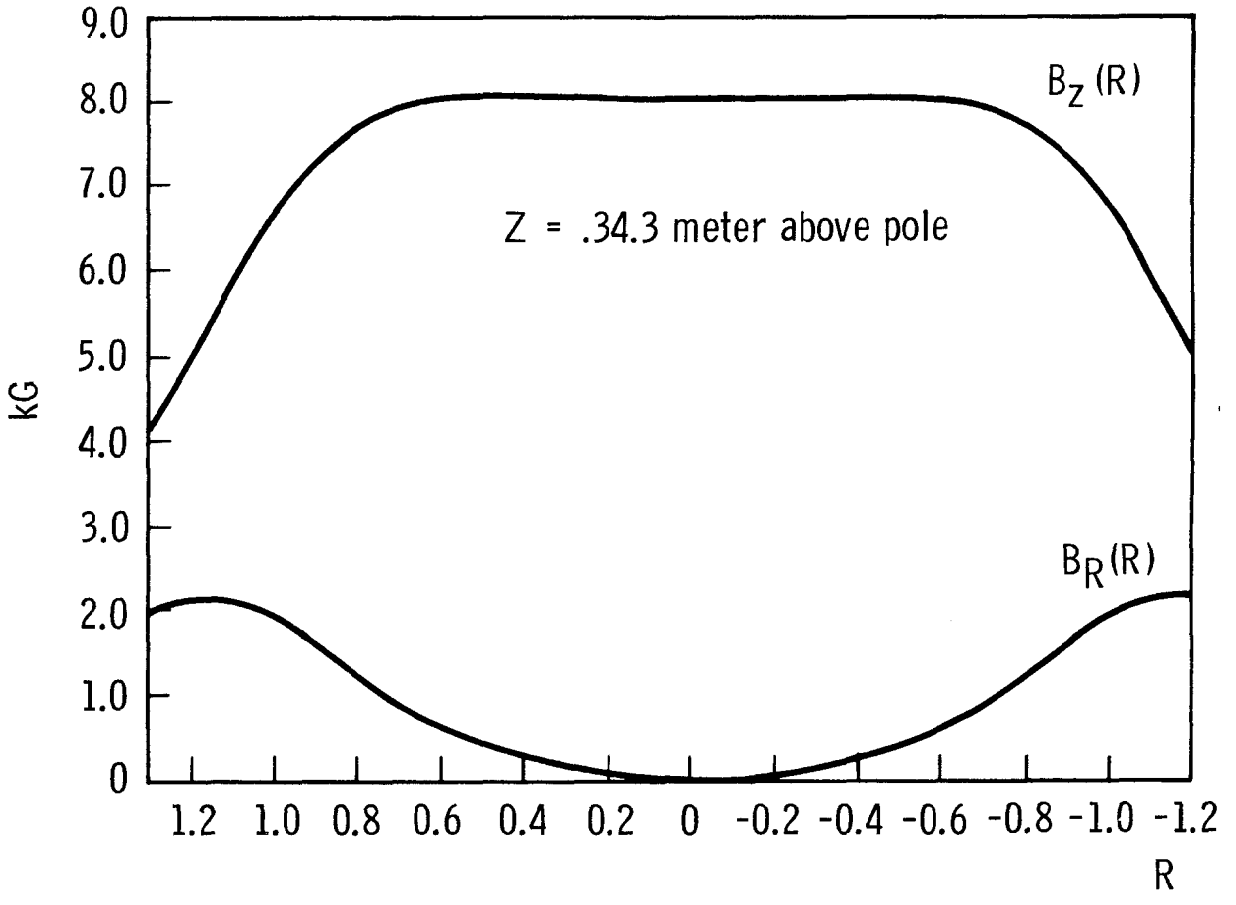
9.0
8.0
7.0
6.0
5.0
4.0
3.0
2.0
1.0
0
kG
B_Z (R)
Z = .34.3 meter above pole
B_R(R)
1.2 1.0 0.8 0.6 0.4 0.2 0 -0.2 -0.4 -0.6 -0.8 -1.0 -1.2
R
RADIAL DISTANCE FROM THE CENTER OF THE MAGNET (in meters)
1276A33

Fig. 7

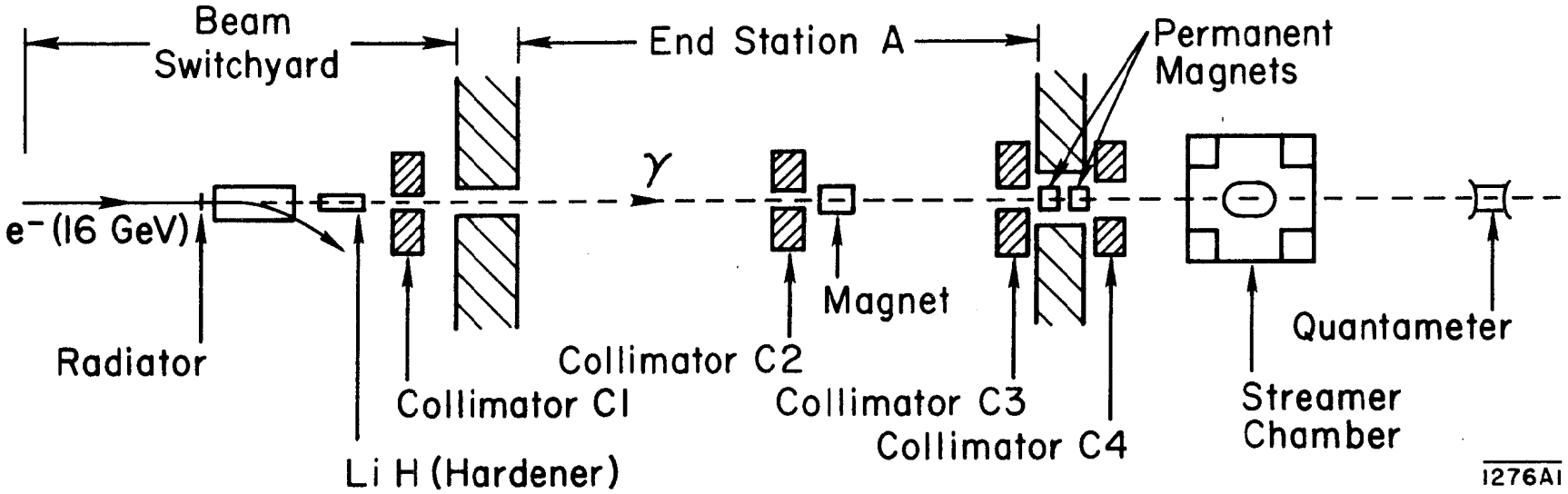
Beam
Switchyard
End Station A
Permanent
Magnets
γ
e⁻ (16 GeV)
Radiator
Li H (Hardener)
Collimator C1
Collimator C2
Magnet
Collimator C3
Collimator C4
Streamer
Chamber
Quantameter
1276A1

Fig. 8

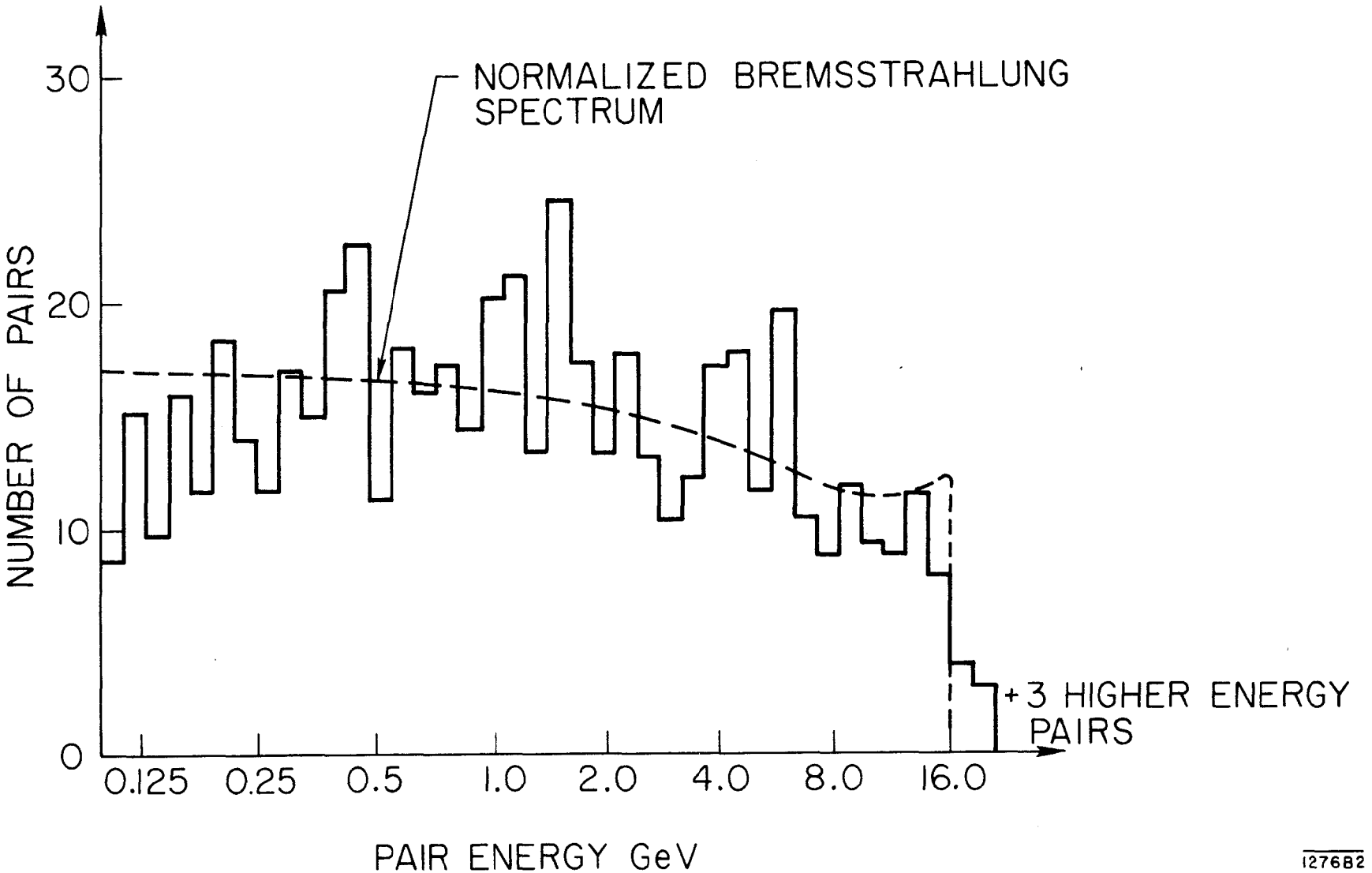
NORMALIZED BREMSSTRAHLUNG SPECTRUM
NUMBER OF PAIRS
30
20
10
0
0.125
0.25
0.5
1.0
2.0
4.0
8.0
16.0
+3 HIGHER ENERGY PAIRS
PAIR ENERGY GeV
127682

Fig. 9

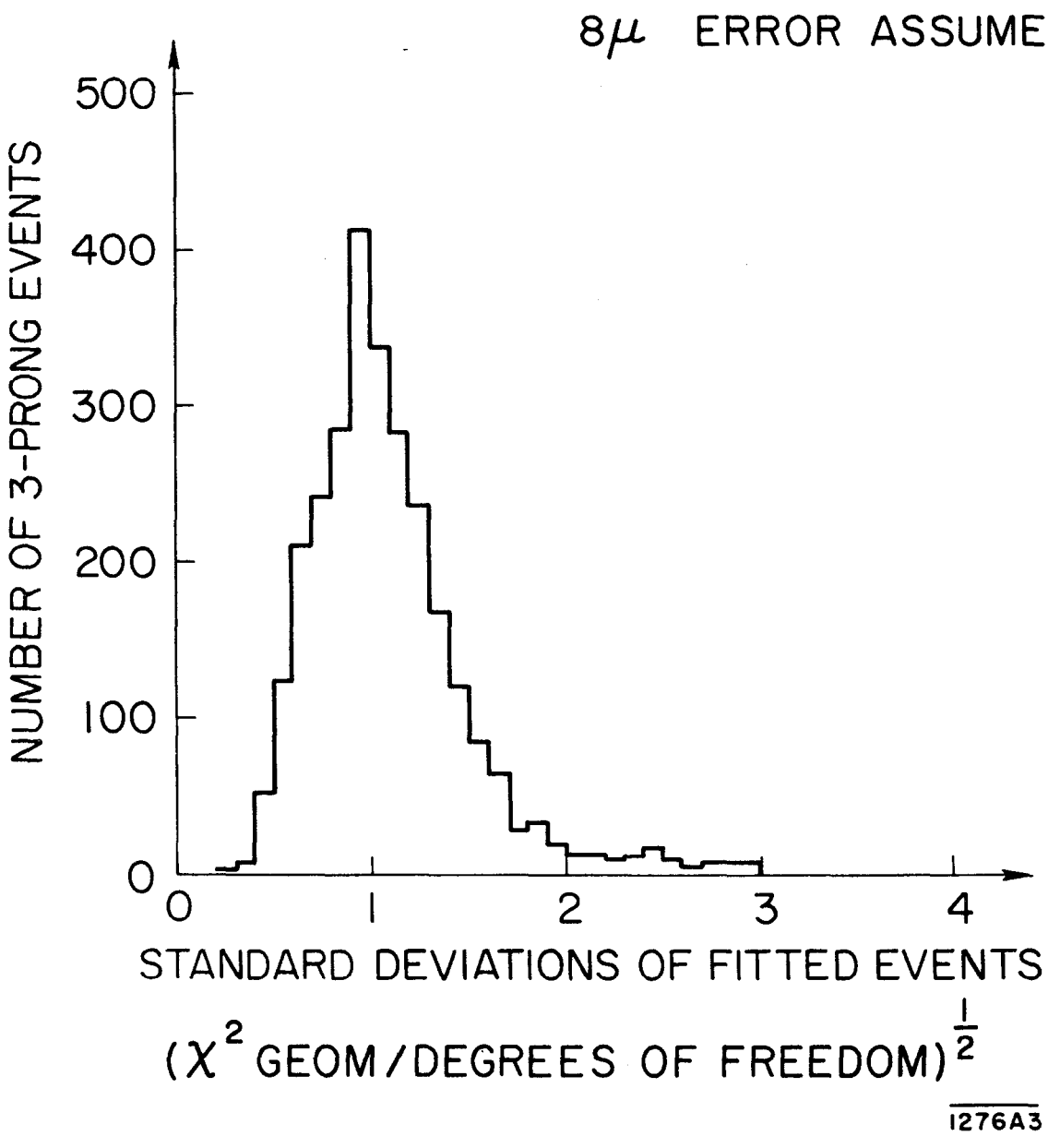
8μ ERROR ASSUMED
NUMBER OF 3-PRONG EVENTS
500
400
300
200
100
0
0
1
2
3
4
STANDARD DEVIATIONS OF FITTED EVENTS
(χ² GEOM/DEGREES OF FREEDOM)^1/2
1276A3

Fig. 10

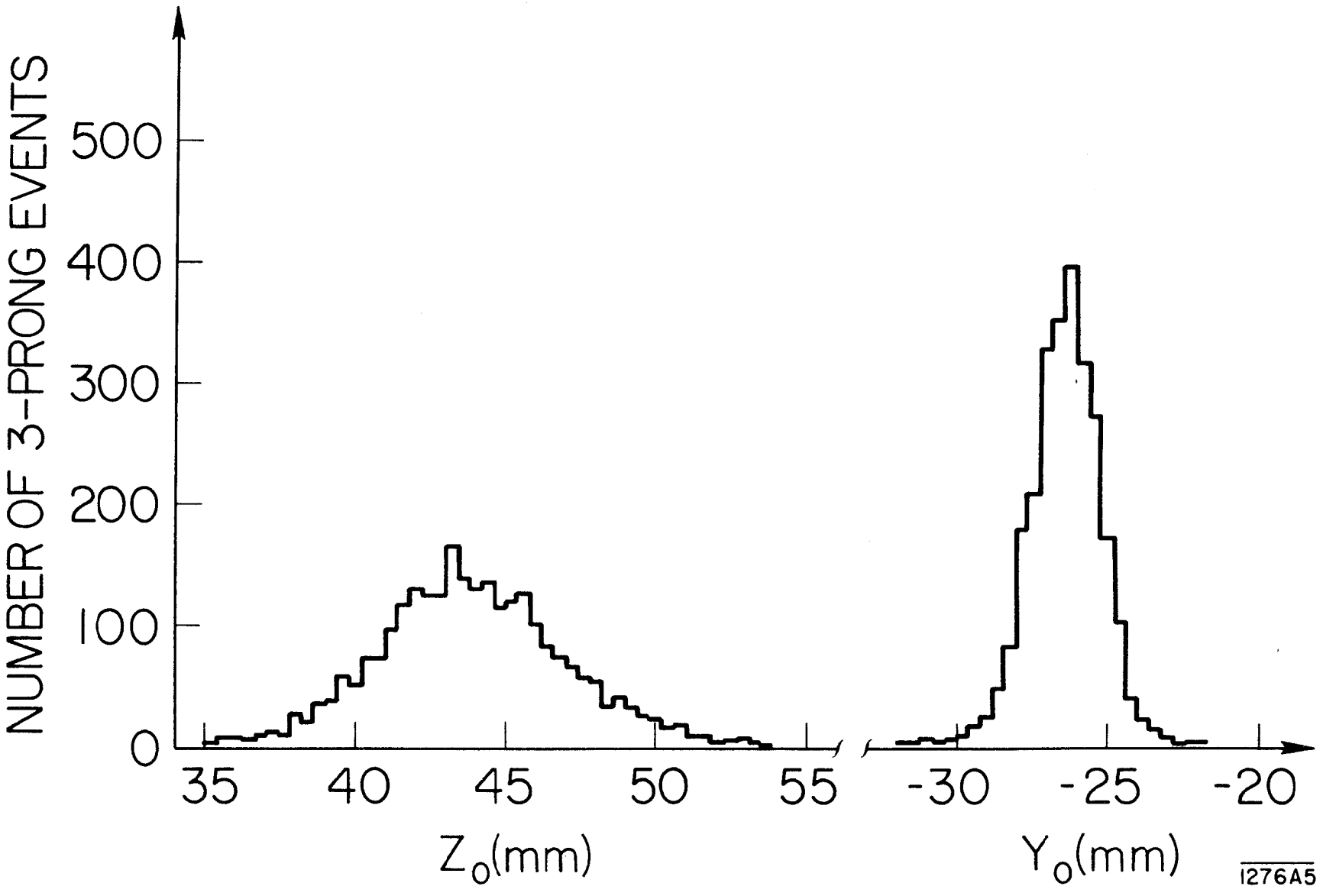
NUMBER OF 3-PRONG EVENTS
500
400
300
200
100
0
35
40
45
50
55
-30
-25
-20
Z_0(mm)
Y_0(mm)
1276A5

Fig. 11

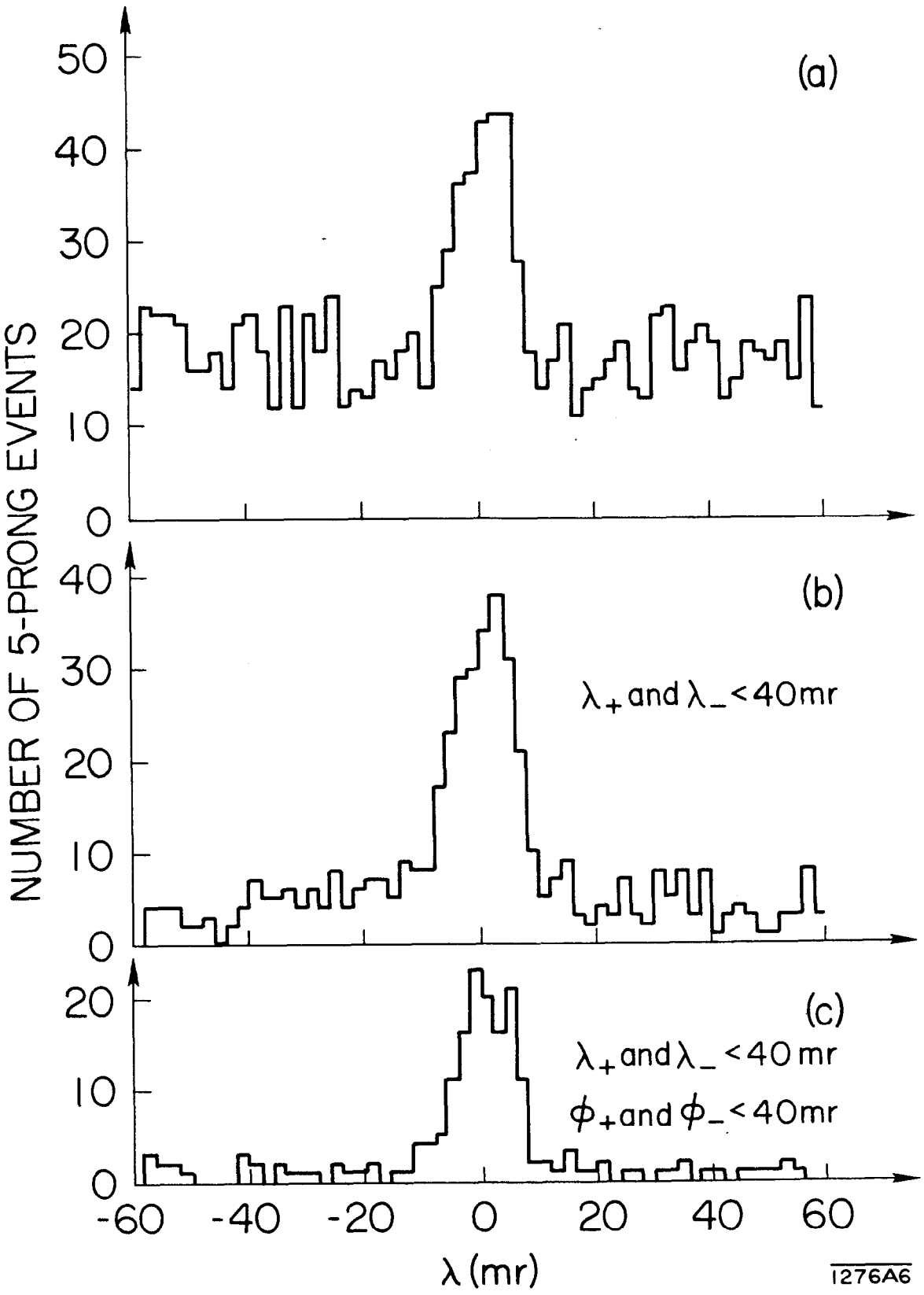
NUMBER OF 5-PRONG EVENTS
50
40
30
20
10
0
(a)
40
30
20
10
0
(b)
λ_+ and λ_- < 40mr
20
10
0
(c)
λ_+ and λ_- < 40 mr
ϕ_+ and ϕ_- < 40mr
-60
-40
-20
0
20
40
60
λ (mr)
1276A6

Fig. 12

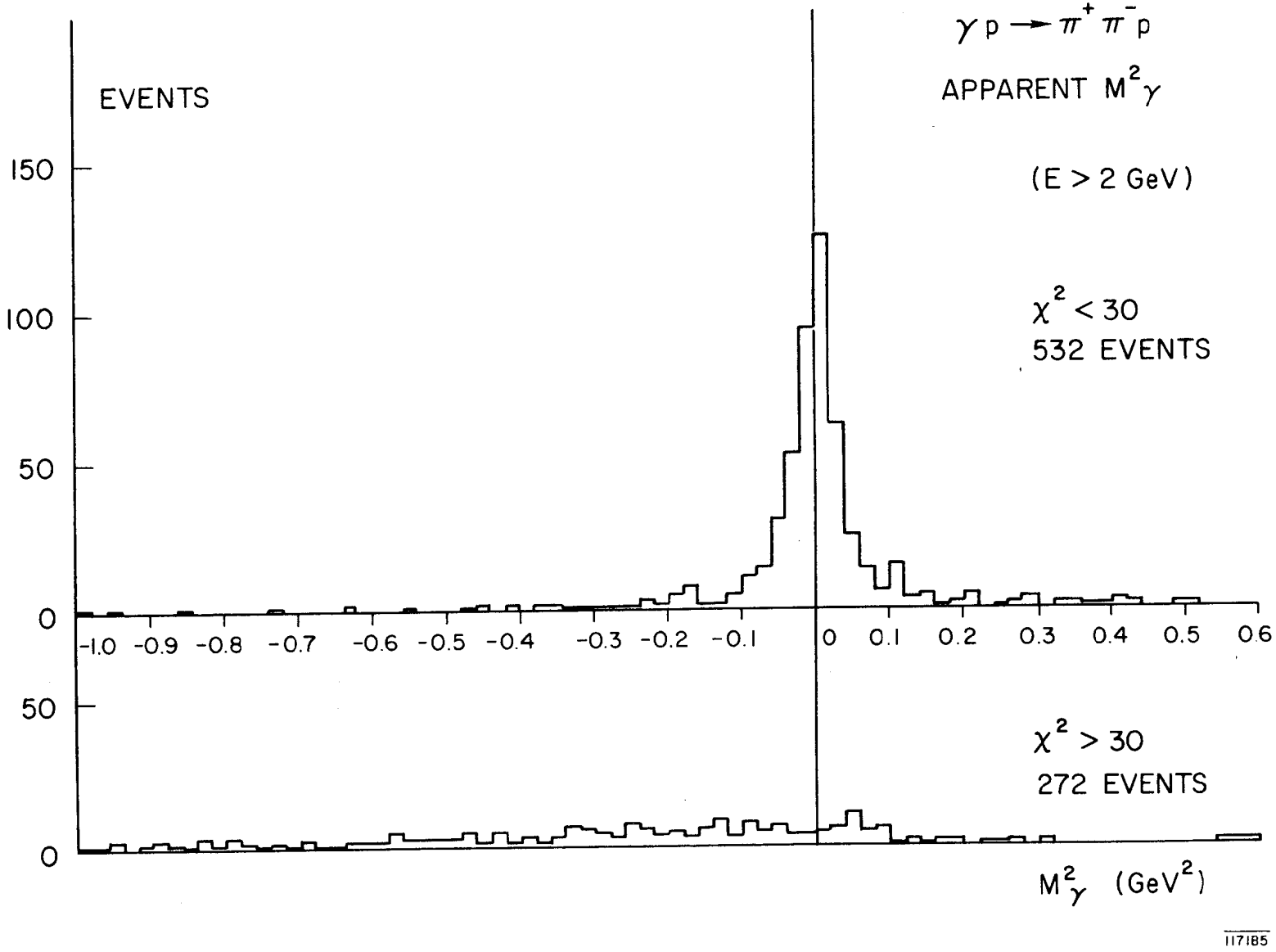
$\gamma p \rightarrow \pi^+ \pi^- p$
APPARENT $M^2\gamma$
(E > 2 GeV)
EVENTS
150
100
50
0
$\chi^2 < 30$
532 EVENTS
-1.0 -0.9 -0.8 -0.7 -0.6 -0.5 -0.4 -0.3 -0.2 -0.1 0 0.1 0.2 0.3 0.4 0.5 0.6
50
0
$\chi^2 > 30$
272 EVENTS
M^2_γ (GeV^2)
117185

Fig. 13

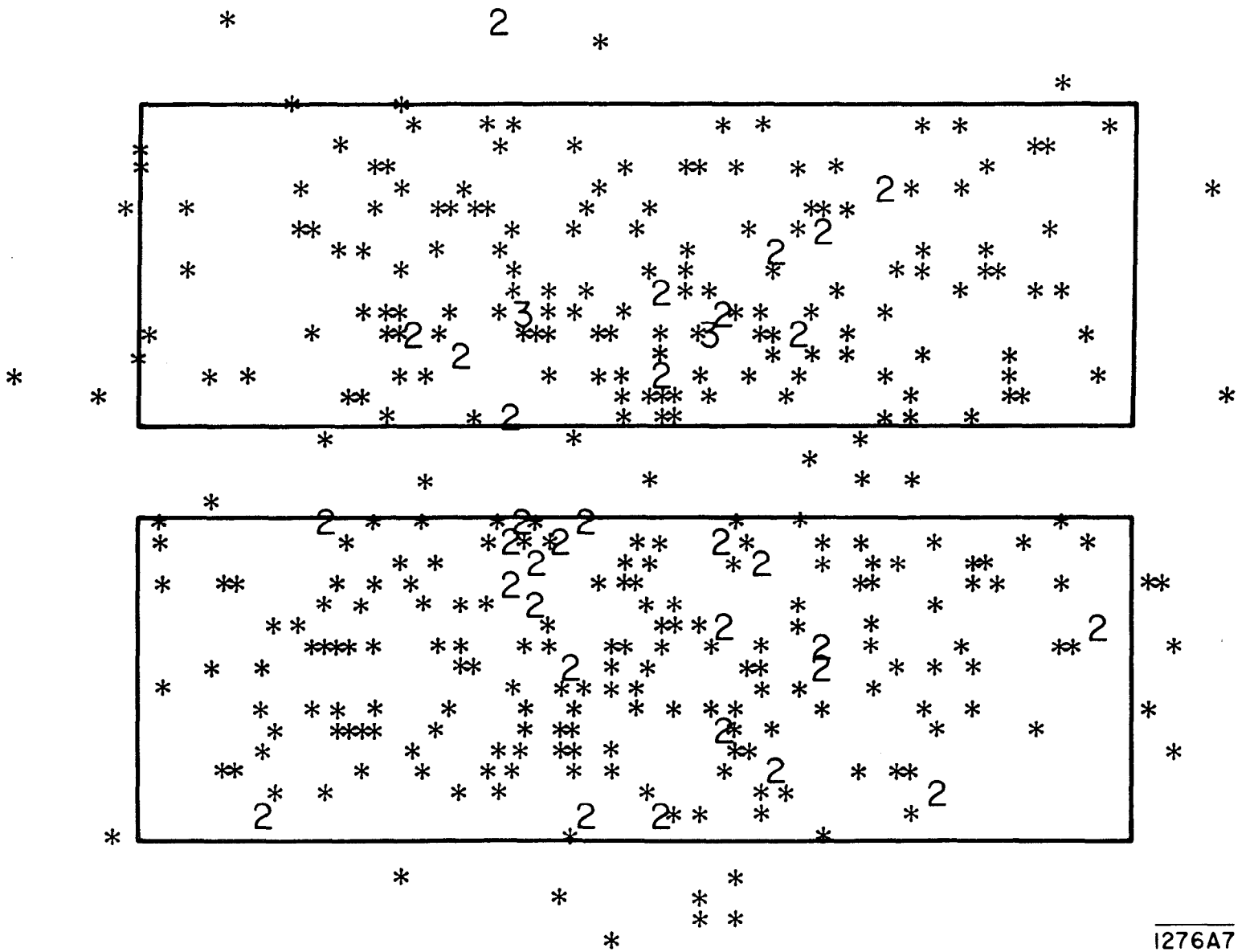

Fig. 14

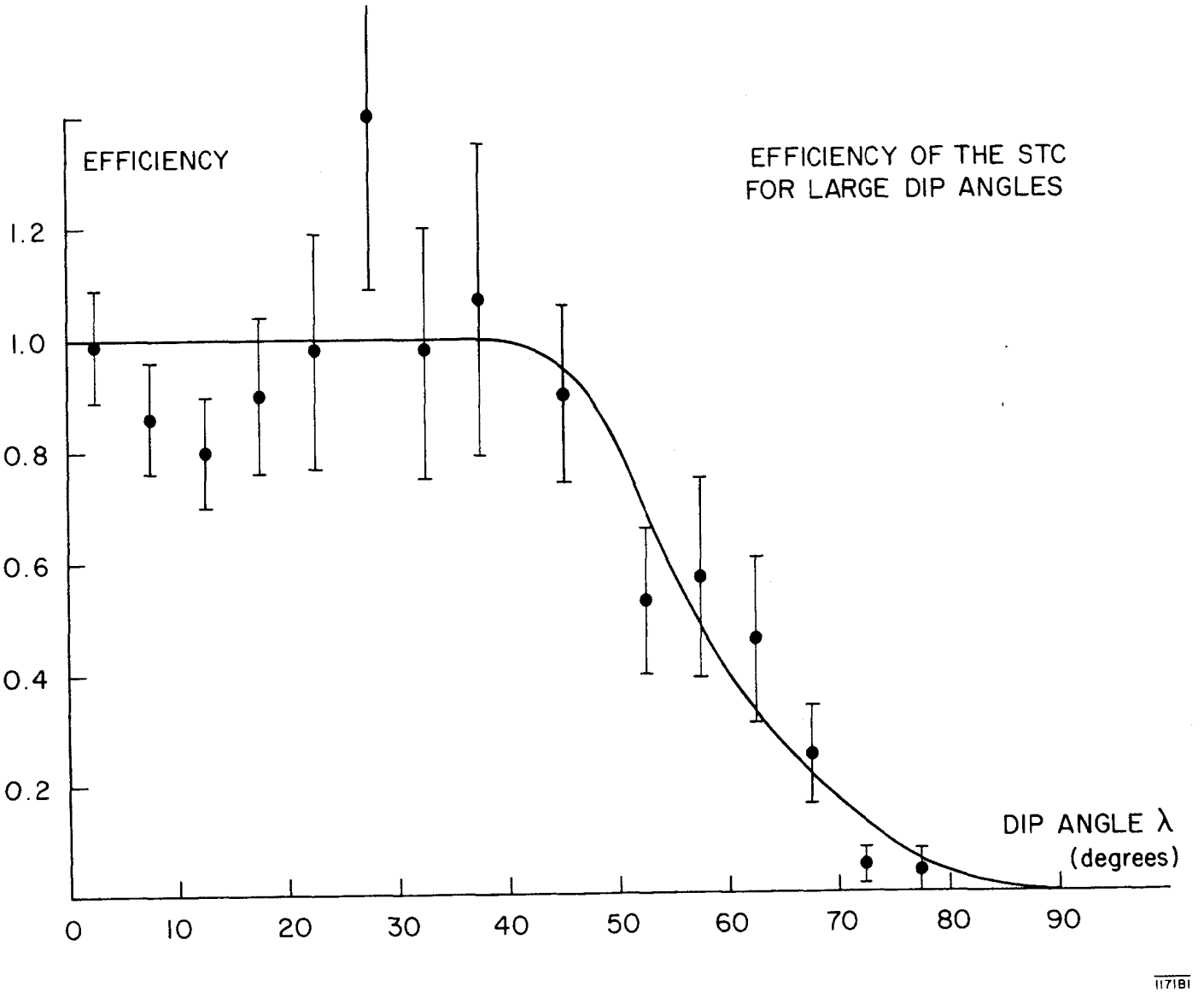
EFFICIENCY
EFFICIENCY OF THE STC
FOR LARGE DIP ANGLES
1.2
1.0
0.8
0.6
0.4
0.2
0
10
20
30
40
50
60
70
80
90
DIP ANGLE λ
(degrees)
117181

Fig. 15

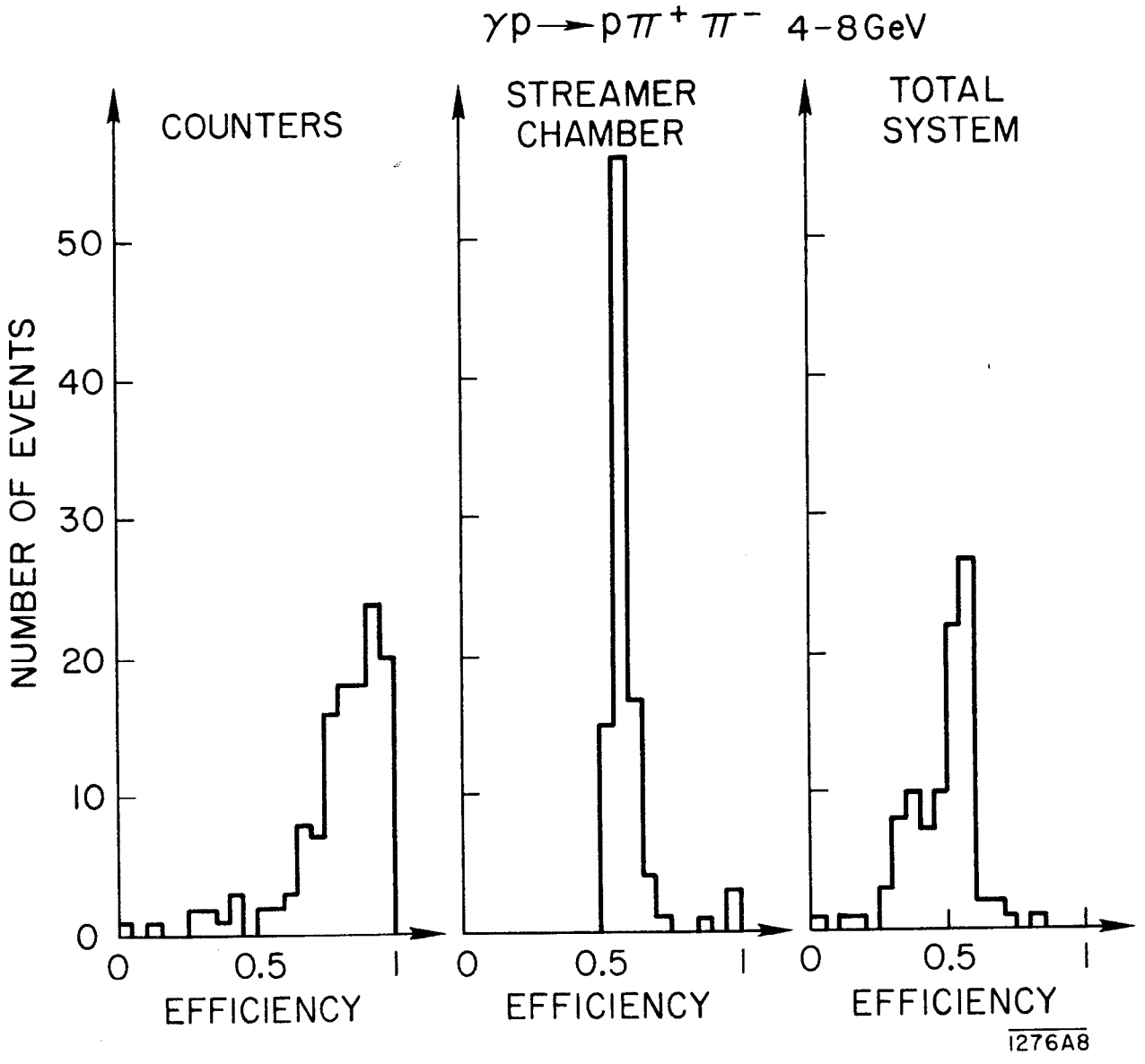
$\gamma p \rightarrow p\pi^+\pi^-$ 4-8 GeV
COUNTERS
STREAMER CHAMBER
TOTAL SYSTEM
NUMBER OF EVENTS
0
10
20
30
40
50
0
0.5
1
EFFICIENCY
1276A8

Fig. 16

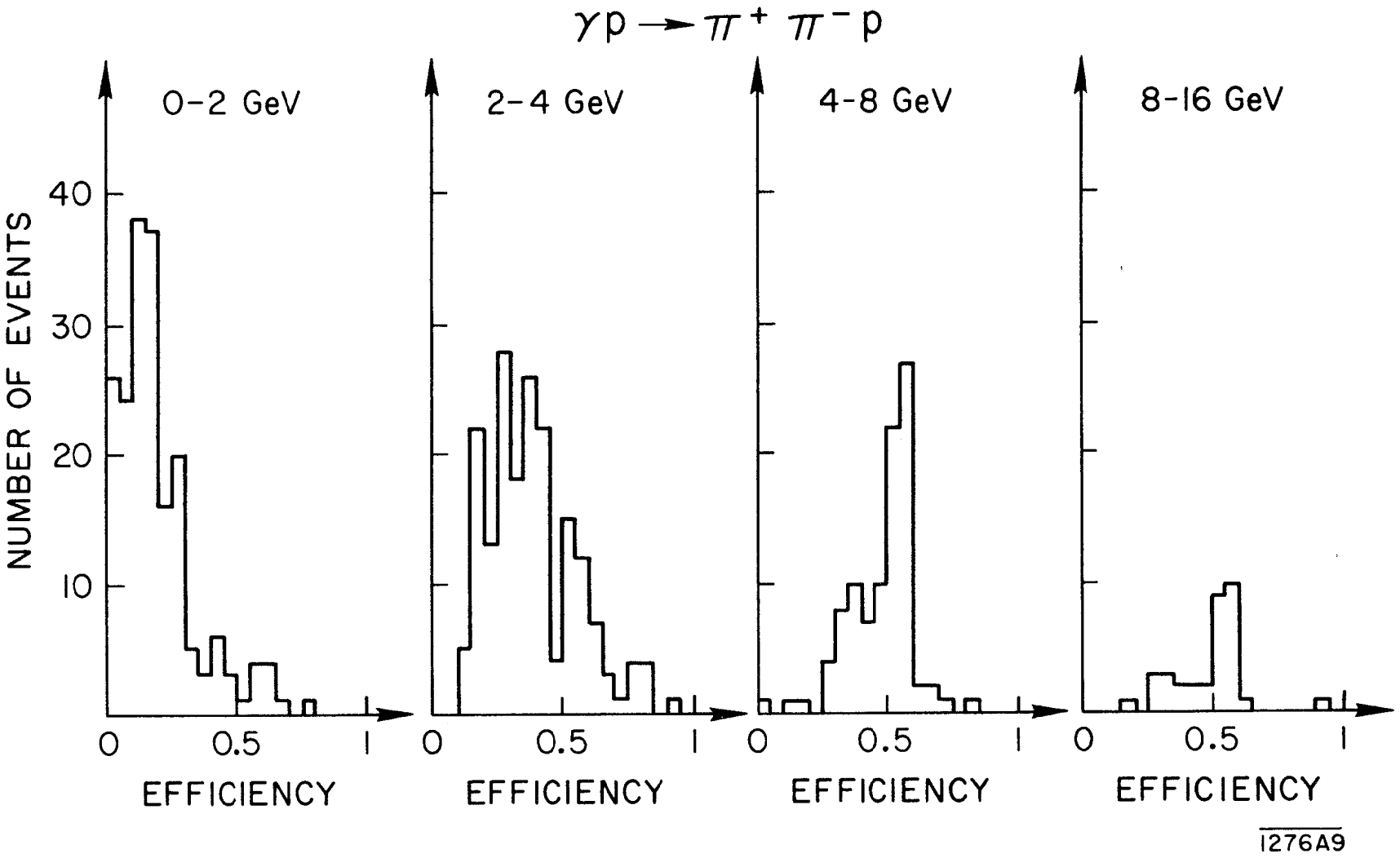
γp → π⁺ π⁻ p
0-2 GeV
2-4 GeV
4-8 GeV
8-16 GeV
NUMBER OF EVENTS
40
30
20
10
0
0.5
1
EFFICIENCY
1276A9

Fig. 17

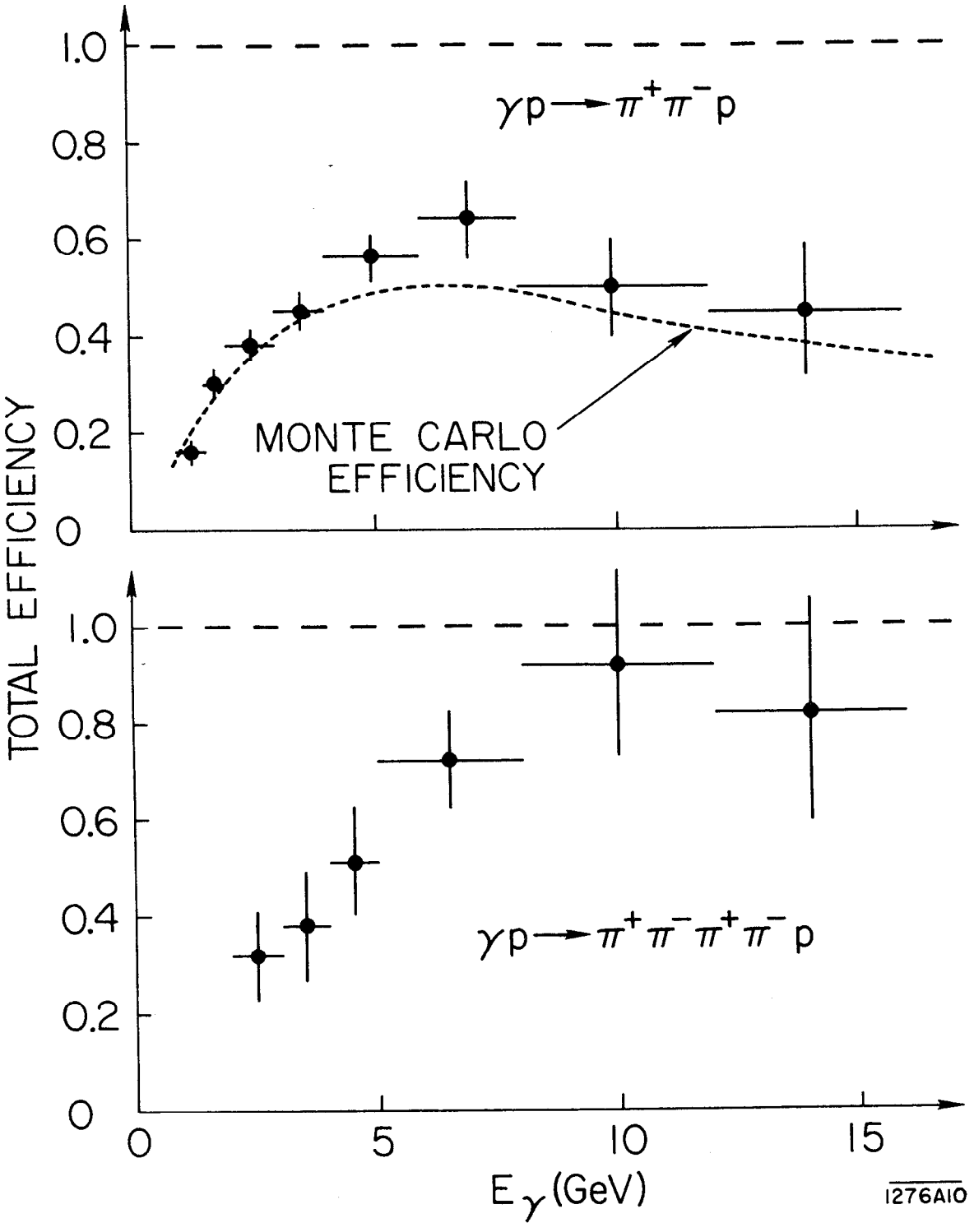
1.0
0.8
0.6
0.4
0.2
0
$\gamma p \rightarrow \pi^+\pi^- p$
MONTE CARLO
EFFICIENCY
TOTAL EFFICIENCY
1.0
0.8
0.6
0.4
0.2
0
$\gamma p \rightarrow \pi^+\pi^-\pi^+\pi^- p$
0
5
10
15
E_γ (GeV)
1276A10

Fig. 18

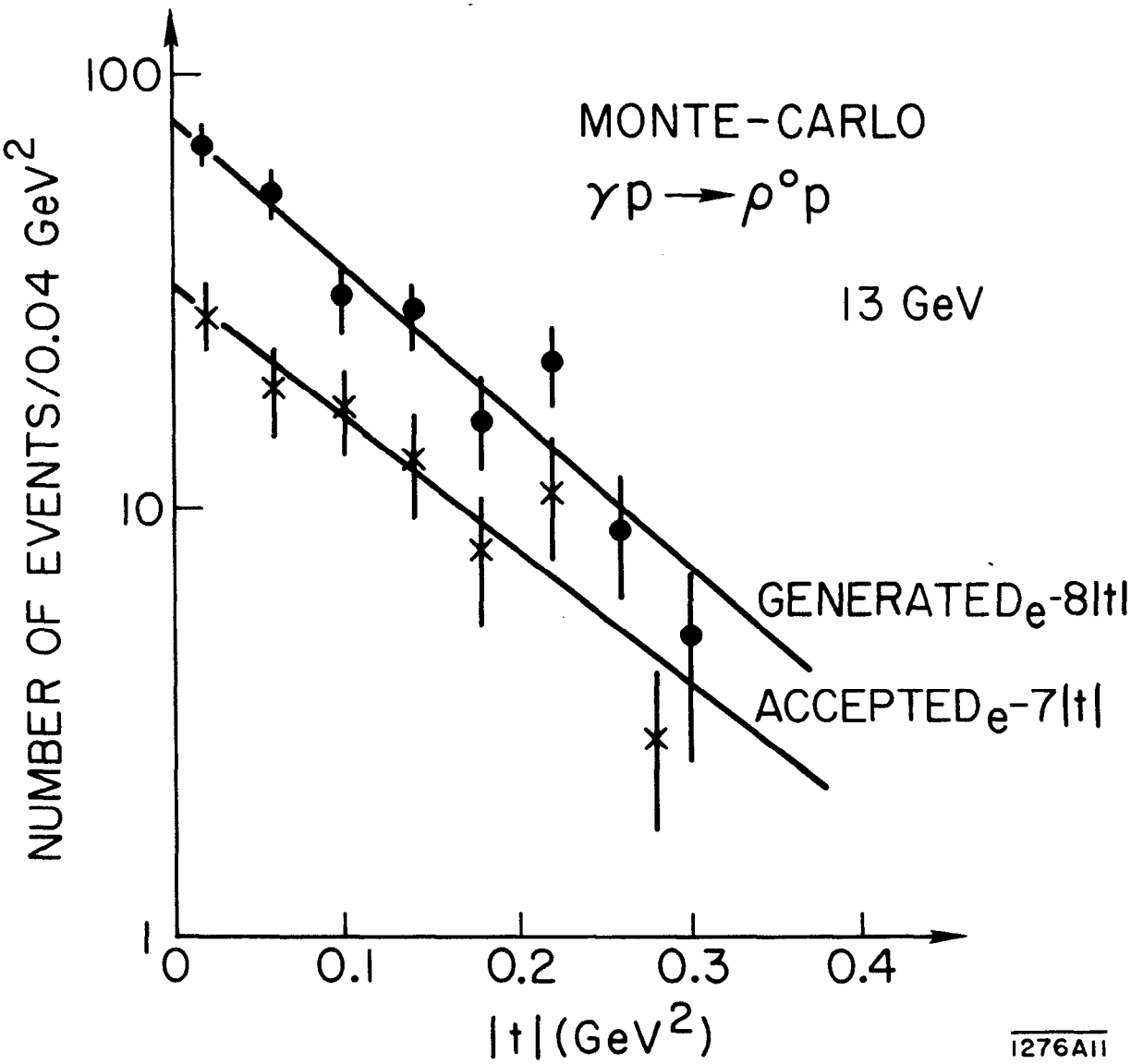
MONTE-CARLO
$\gamma p \rightarrow \rho^0 p$
13 GeV
GENERATED$_e$-8|t|
ACCEPTED$_e$-7|t|
NUMBER OF EVENTS/0.04 GeV^2
100
10
1
0
0.1
0.2
0.3
0.4
|t| (GeV^2)
1276A11

Fig. 19

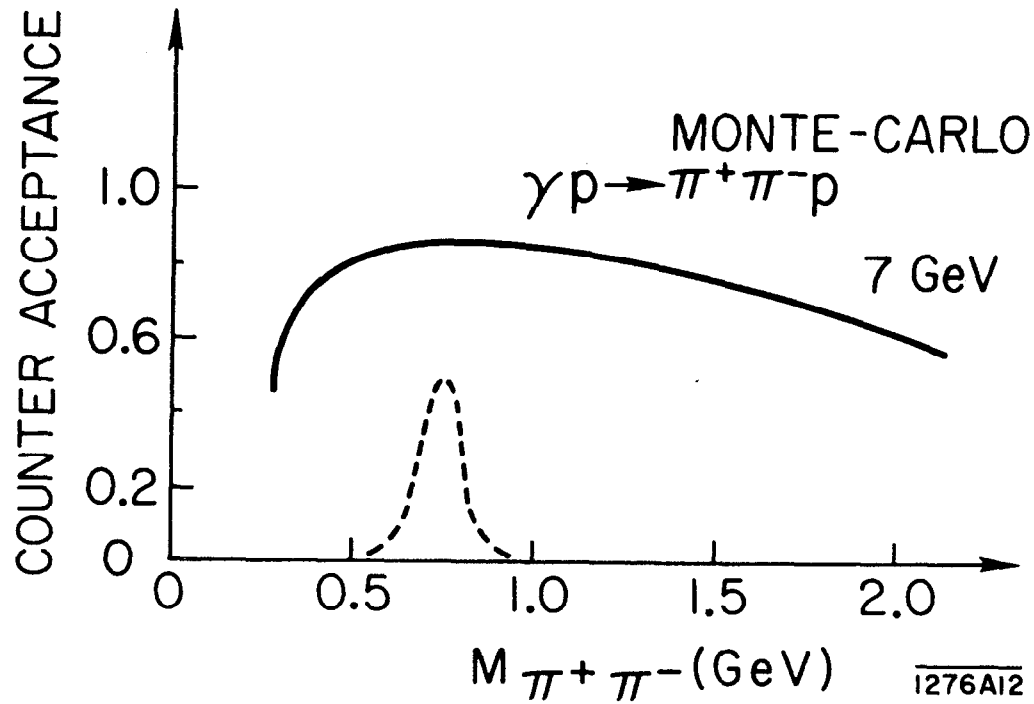
COUNTER ACCEPTANCE
1.0
0.6
0.2
0
MONTE-CARLO
γp→π+π-p
7 GeV
0
0.5
1.0
1.5
2.0
M π+ π- (GeV)
1276A12

Fig. 20

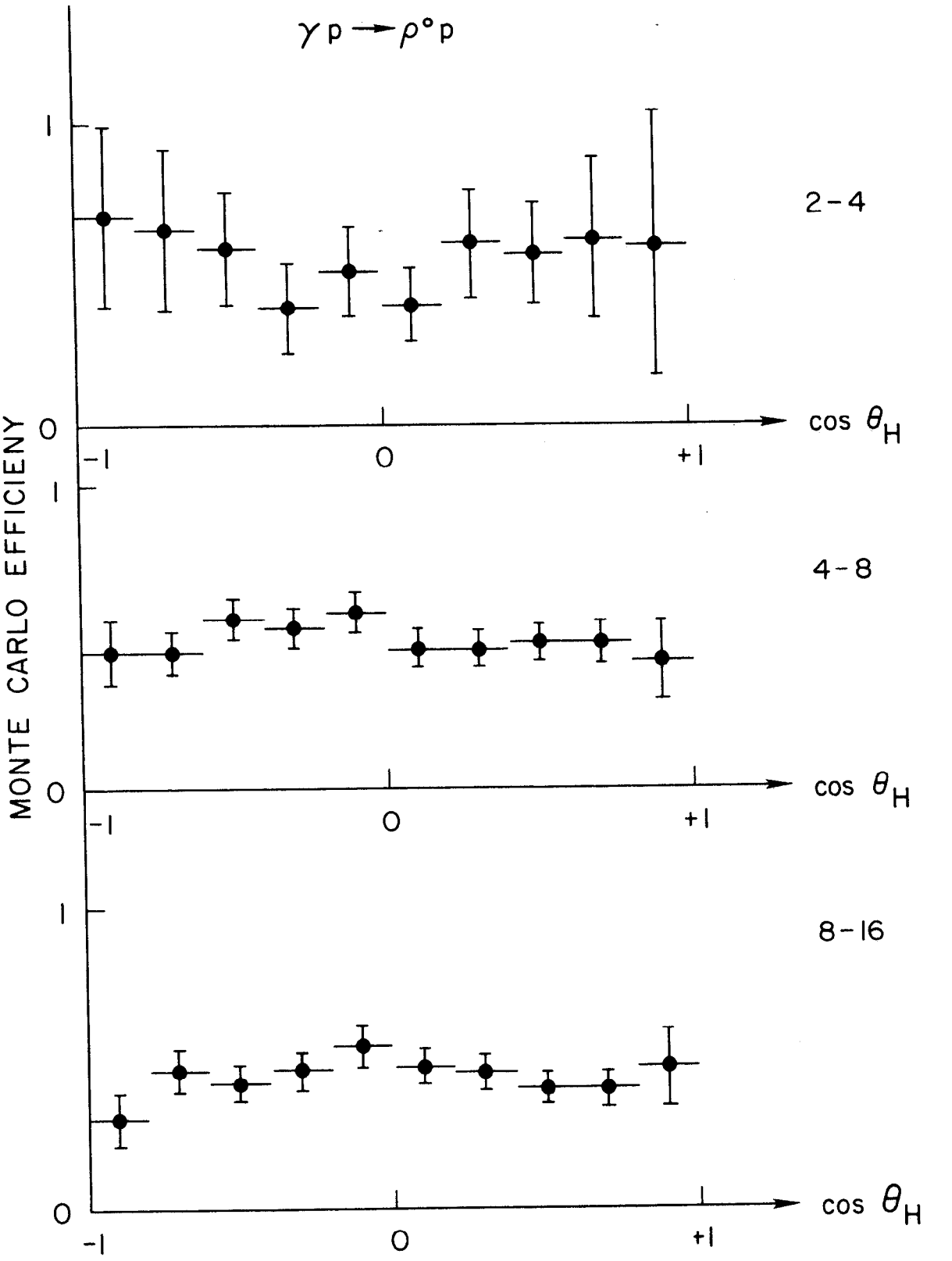

Fig. 21

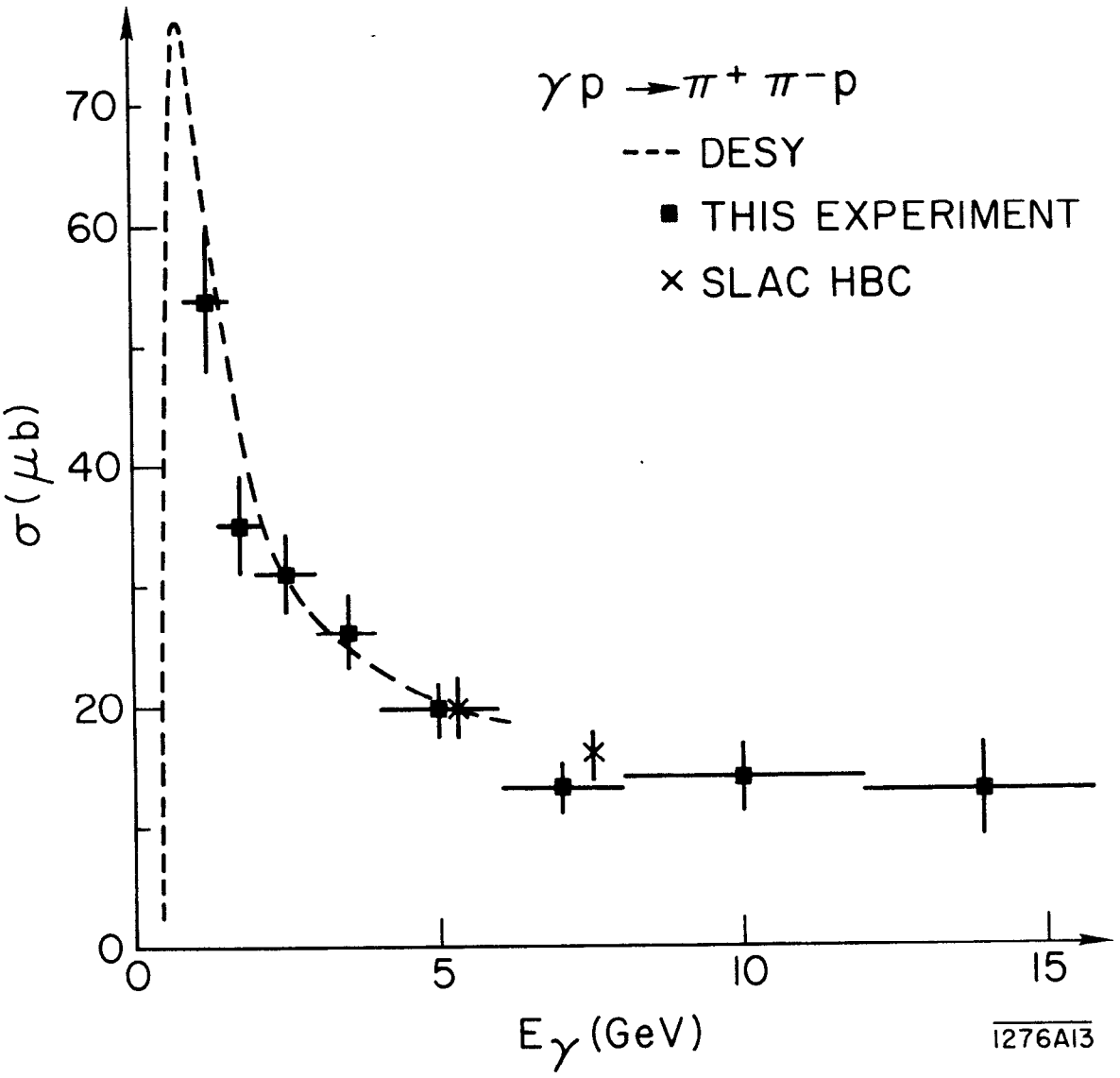
γ p → π⁺ π⁻ p
--- DESY
■ THIS EXPERIMENT
× SLAC HBC
σ (μb)
70
60
40
20
0
0
5
10
15
E_γ (GeV)
1276A13

Fig. 22

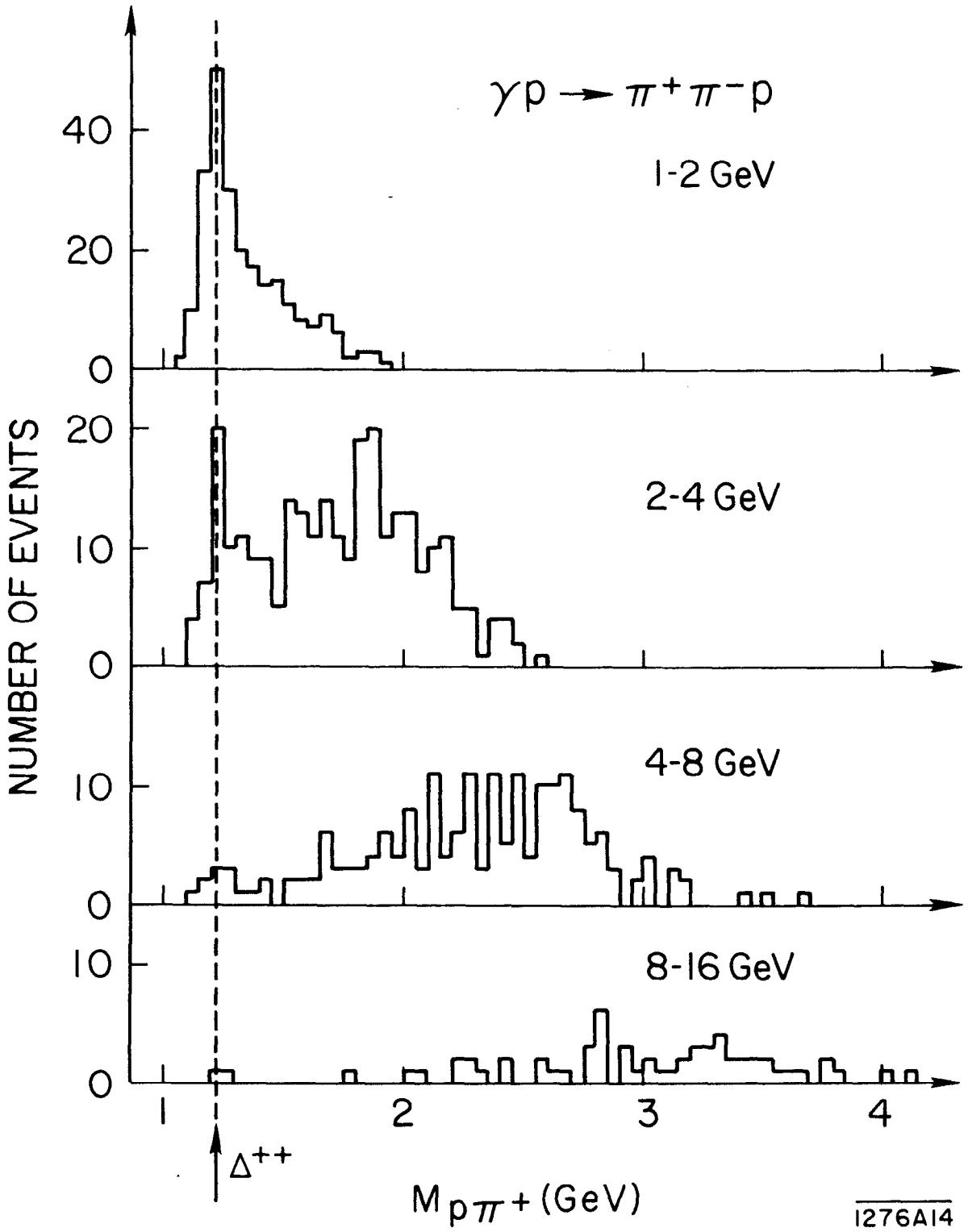
γp → π+π−p
1-2 GeV
2-4 GeV
4-8 GeV
8-16 GeV
NUMBER OF EVENTS
40
20
0
20
10
0
10
0
10
0
1
2
3
4
Δ++
M pπ+ (GeV)
1276A14

Fig. 23

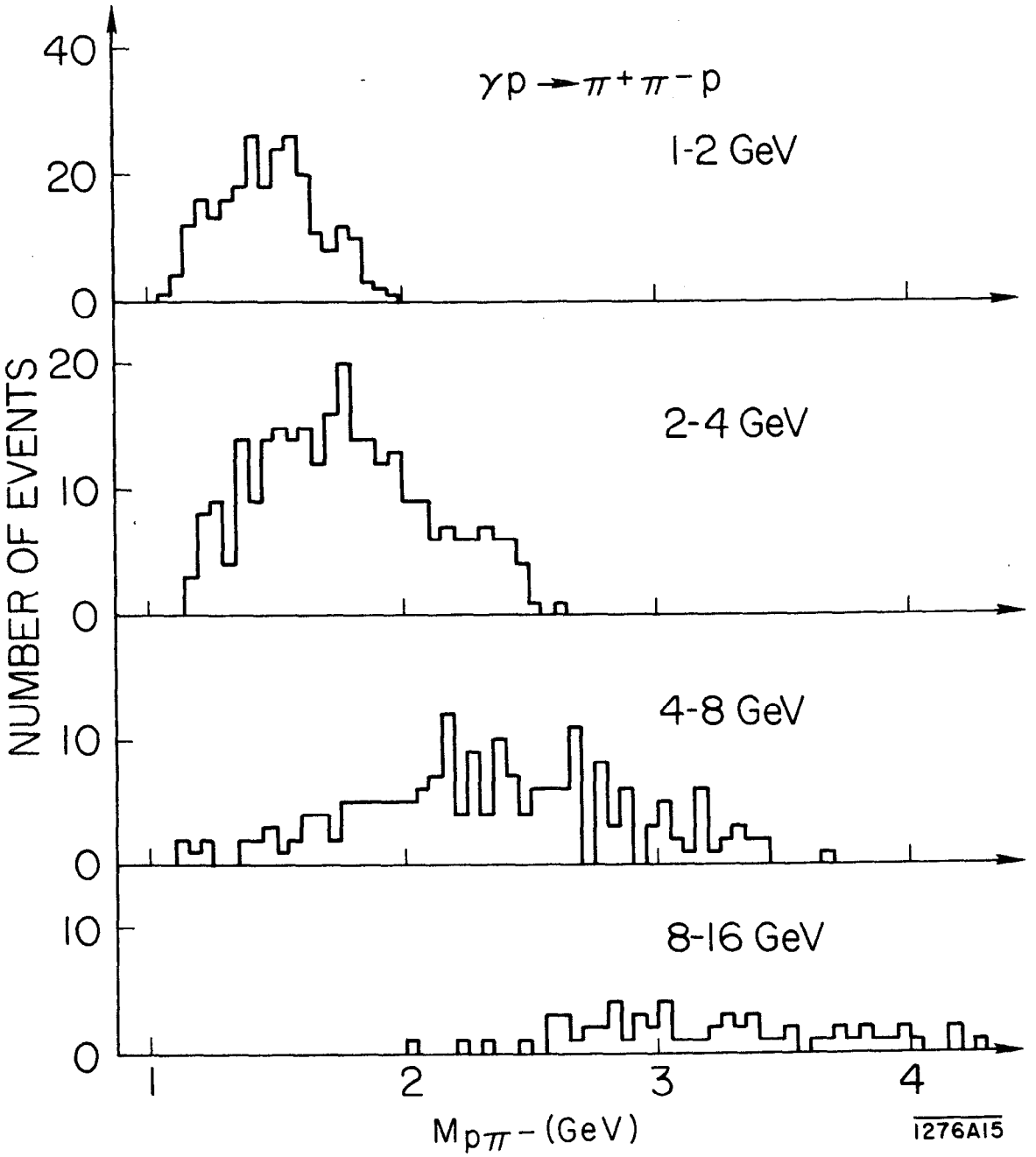
$\gamma p \to \pi^+ \pi^- p$
1-2 GeV
2-4 GeV
4-8 GeV
8-16 GeV
NUMBER OF EVENTS
40
20
0
20
10
0
10
0
10
0
1
2
3
4
$M_{p\pi^-}$ (GeV)
1276A15

Fig. 24

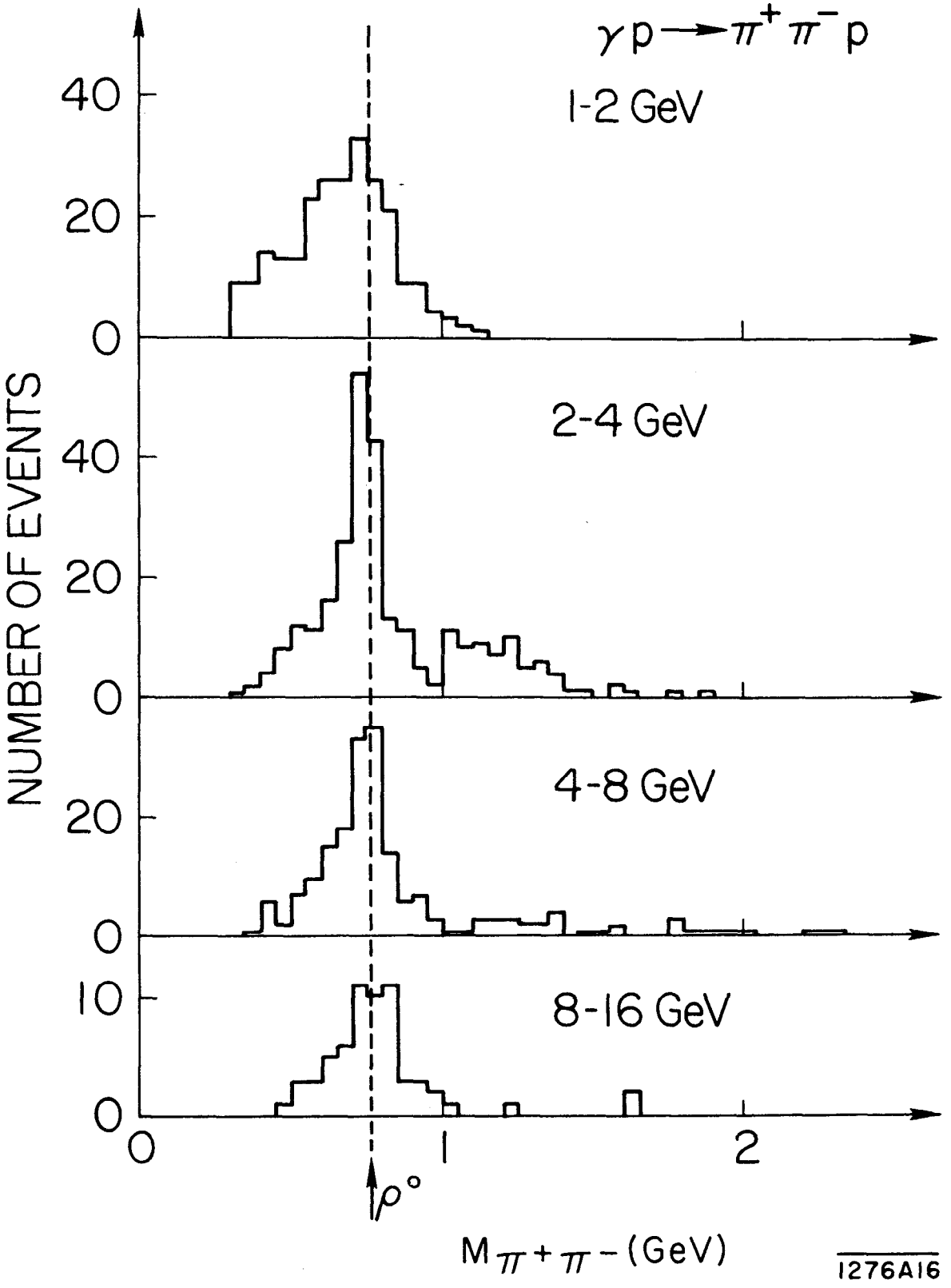
γp → π⁺π⁻p
1-2 GeV
2-4 GeV
4-8 GeV
8-16 GeV
NUMBER OF EVENTS
40
20
0
40
20
0
20
0
10
0
0
1
2
ρ°
M π⁺π⁻ (GeV)
1276A16

Fig. 25

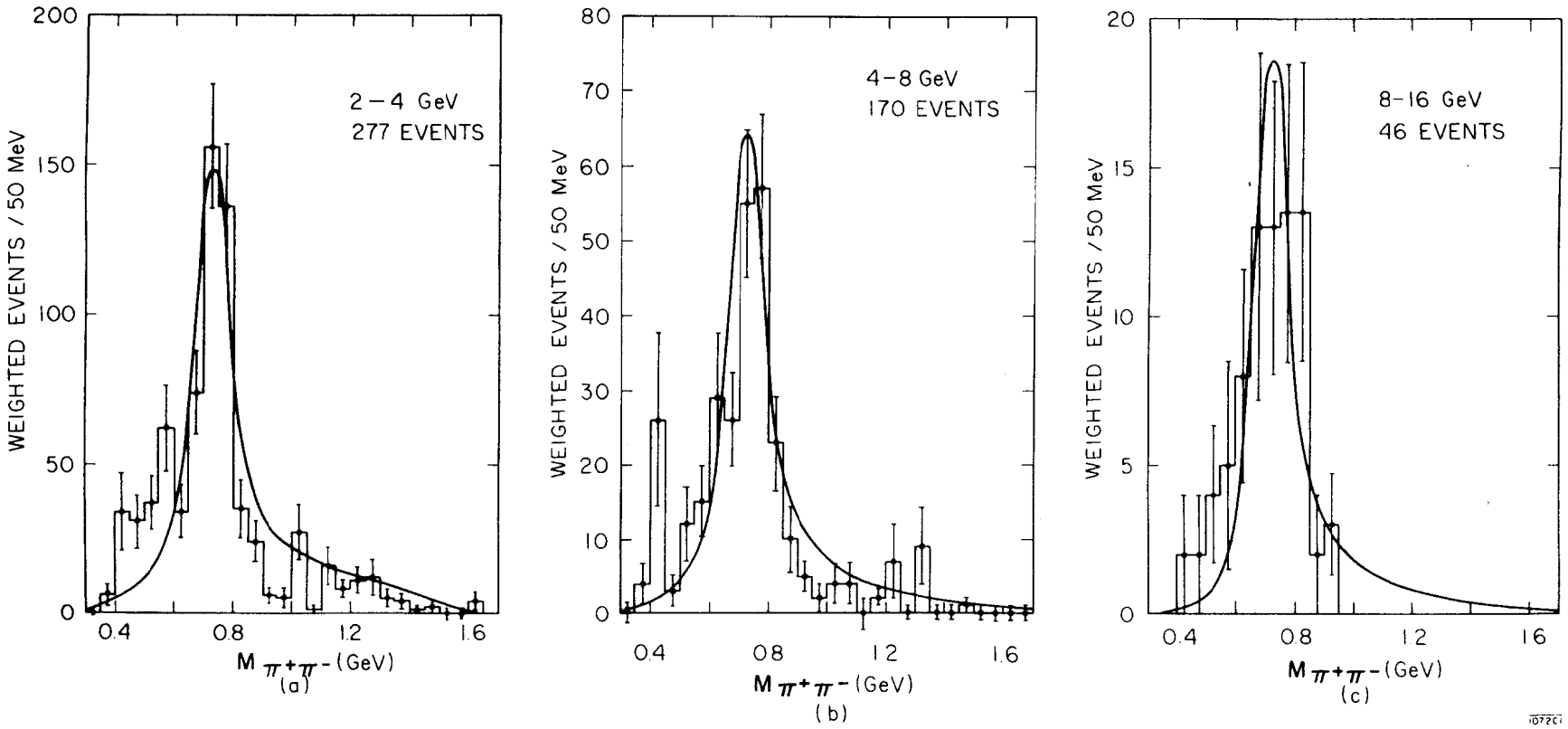
2−4 GeV
277 EVENTS
WEIGHTED EVENTS / 50 MeV
M π+π− (GeV)
(a)
4−8 GeV
170 EVENTS
WEIGHTED EVENTS / 50 MeV
M π+π− (GeV)
(b)
8−16 GeV
46 EVENTS
WEIGHTED EVENTS / 50 MeV
M π+π− (GeV)
(c)

Fig. 26

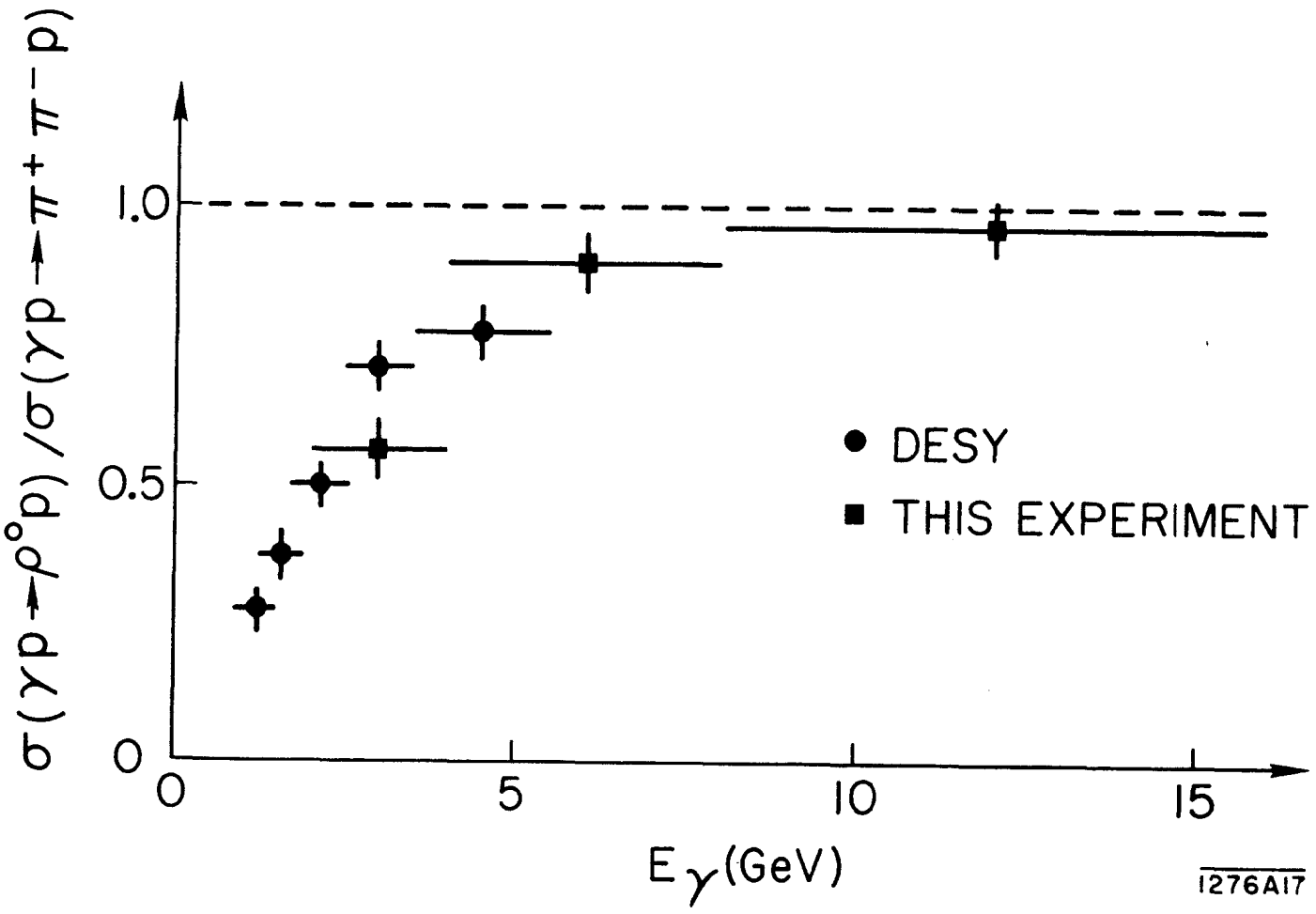
σ(γp→ρ°p) /σ(γp→π+π−p)
1.0
0.5
0
0
5
10
15
Eγ(GeV)
DESY
THIS EXPERIMENT
1276A17

Fig. 27

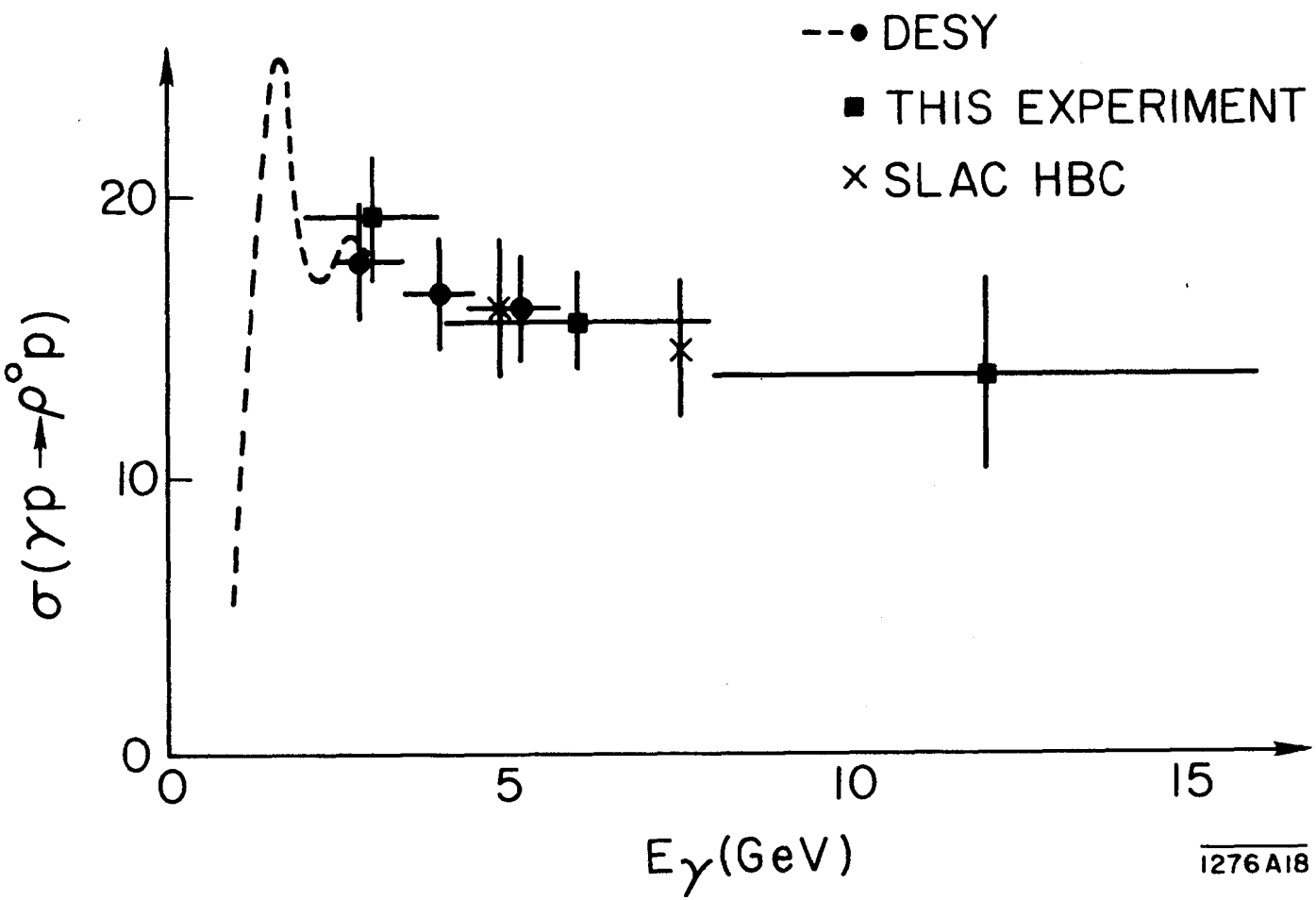
--• DESY
■ THIS EXPERIMENT
× SLAC HBC
20
10
0
0
5
10
15
σ(γp→ρ°p)
Eγ(GeV)
1276A18

Fig. 28

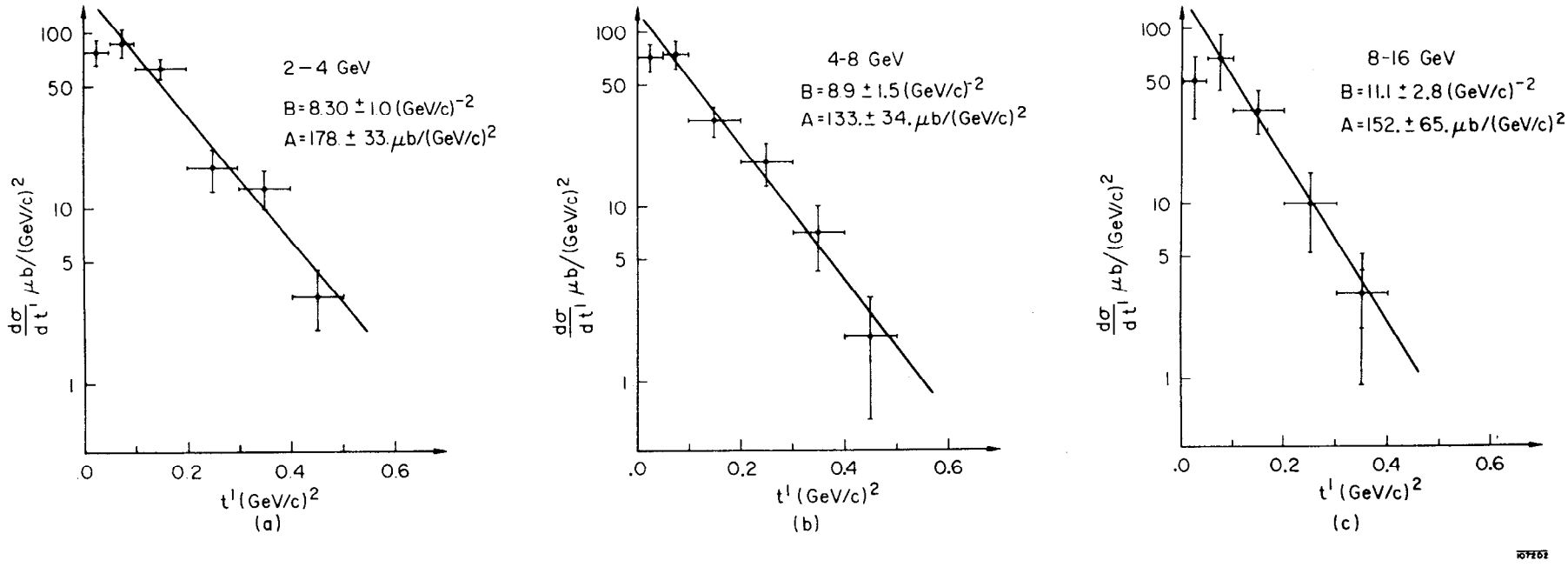
2-4 GeV
B=8.30 ± 1.0 (GeV/c)$^{-2}$
A=178. ± 33. μb/(GeV/c)^2
$\frac{d\sigma}{dt'}$ μb/(GeV/c)^2
t'(GeV/c)^2
(a)
4-8 GeV
B=8.9 ± 1.5 (GeV/c)$^{-2}$
A=133. ± 34. μb/(GeV/c)^2
$\frac{d\sigma}{dt'}$ μb/(GeV/c)^2
t' (GeV/c)^2
(b)
8-16 GeV
B=11.1 ± 2.8 (GeV/c)$^{-2}$
A=152. ± 65. μb/(GeV/c)^2
$\frac{d\sigma}{dt'}$ μb/(GeV/c)^2
t' (GeV/c)^2
(c)

Fig. 29

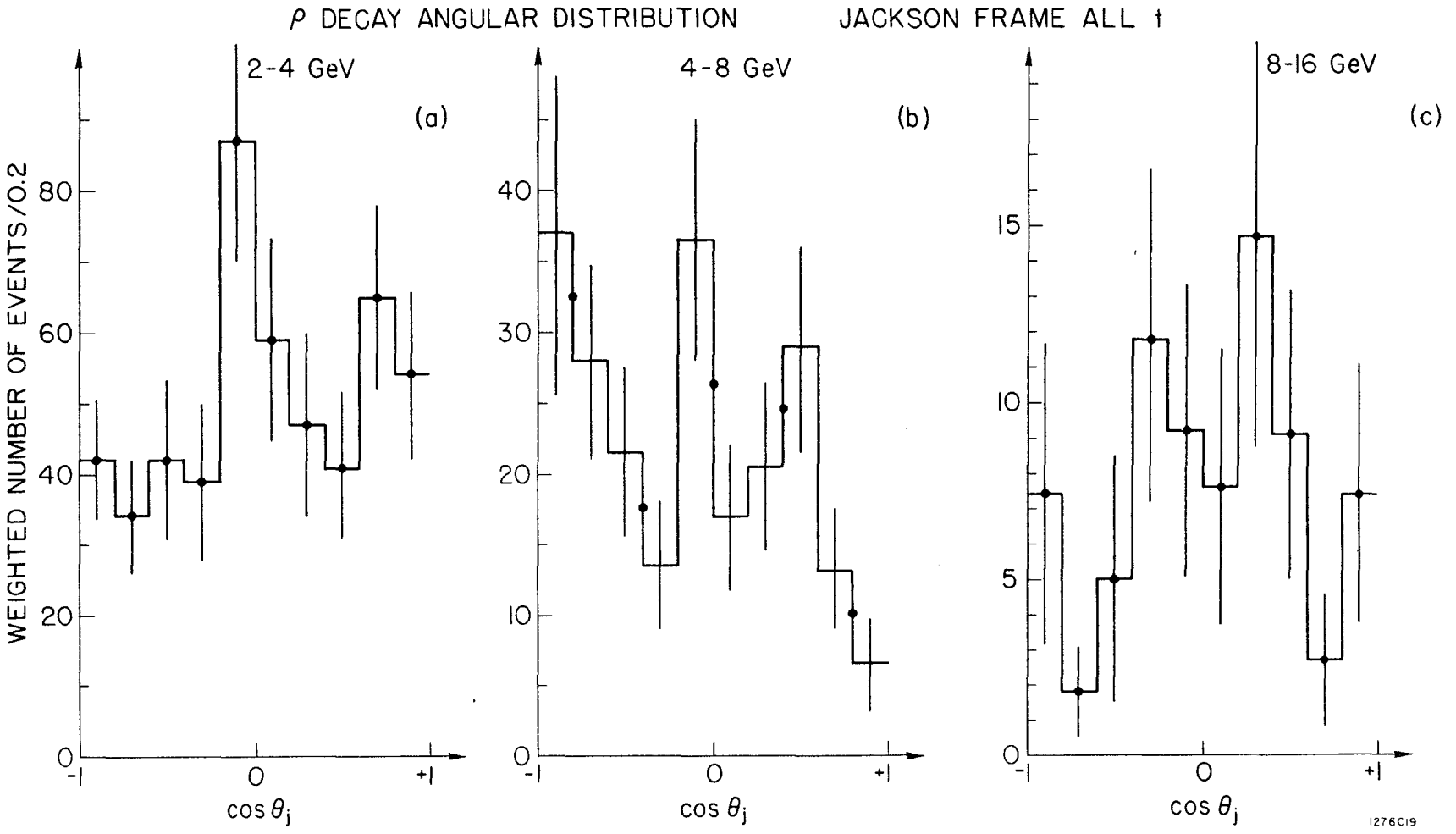
ρ DECAY ANGULAR DISTRIBUTION
JACKSON FRAME ALL t
2-4 GeV
(a)
4-8 GeV
(b)
8-16 GeV
(c)
WEIGHTED NUMBER OF EVENTS/0.2
0
20
40
60
80
10
30
5
15
-1
0
+1
cos θj
1276C19

Fig. 30

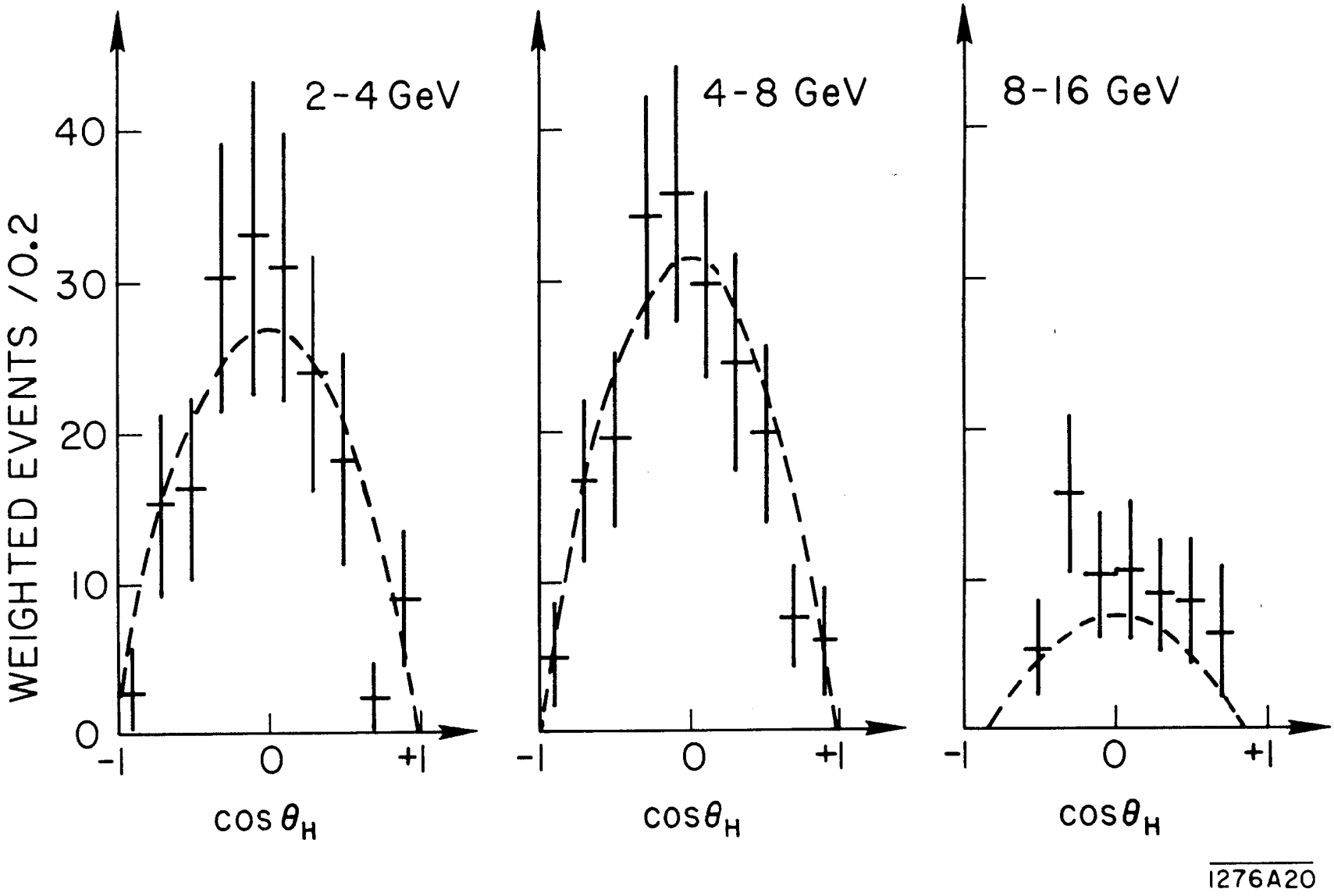
2-4 GeV
4-8 GeV
8-16 GeV
WEIGHTED EVENTS /0.2
40
30
20
10
0
-1
0
+1
cos θH
cos θH
cos θH
1276A20

Fig. 31

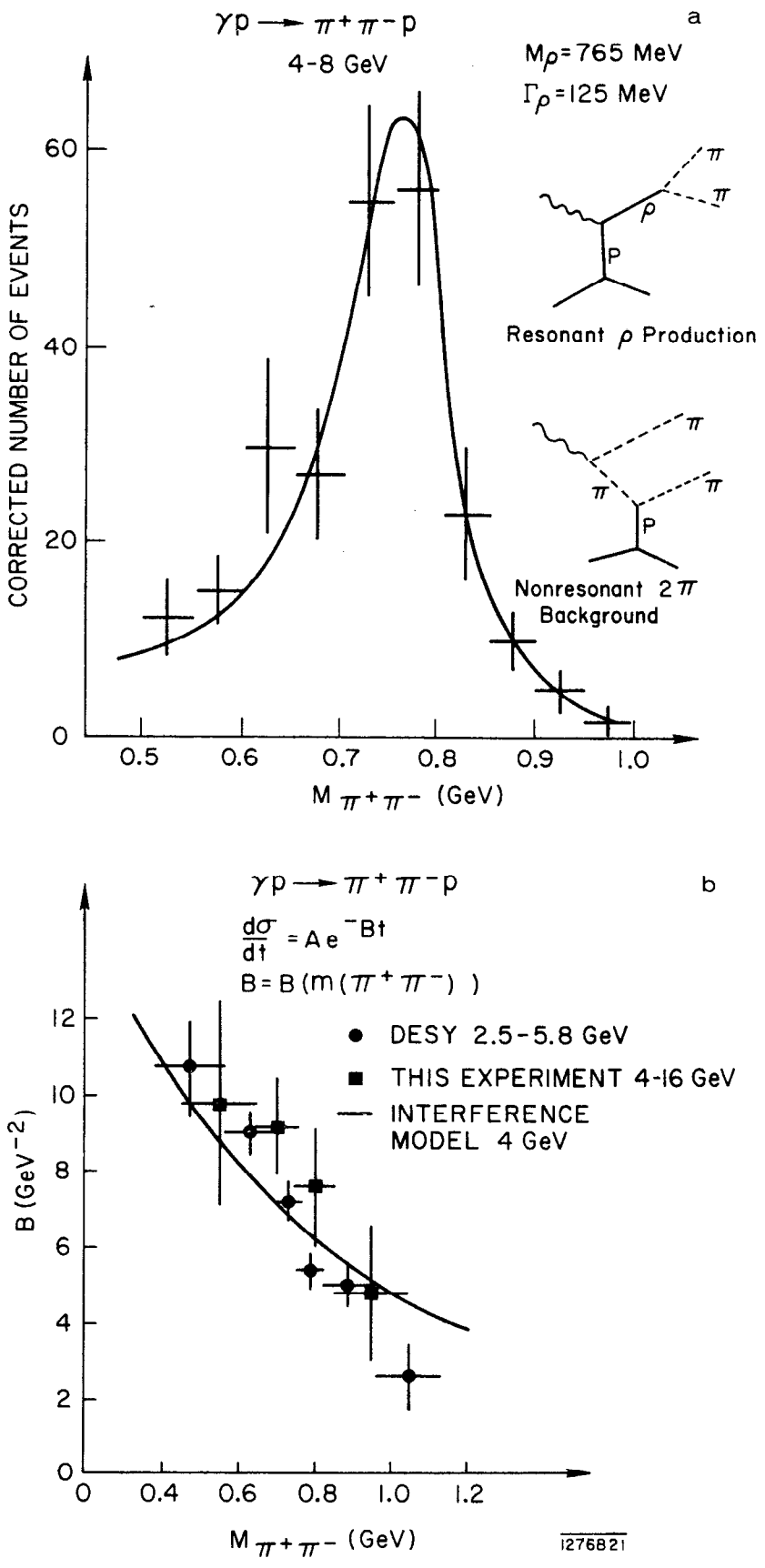
γp → π+π−p
a
4-8 GeV
Mρ=765 MeV
Γρ=125 MeV
π
π
ρ
P
Resonant ρ Production
π
π
π
P
Nonresonant 2π
Background
CORRECTED NUMBER OF EVENTS
60
40
20
0
0.5
0.6
0.7
0.8
0.9
1.0
M π+π− (GeV)
γp → π+π−p
b
dσ/dt = Ae^−Bt
B = B(m(π+π−))
DESY 2.5-5.8 GeV
THIS EXPERIMENT 4-16 GeV
INTERFERENCE
MODEL 4 GeV
B (GeV^−2)
12
10
8
6
4
2
0
0
0.4
0.6
0.8
1.0
1.2
M π+π− (GeV)
1276821

Fig. 32

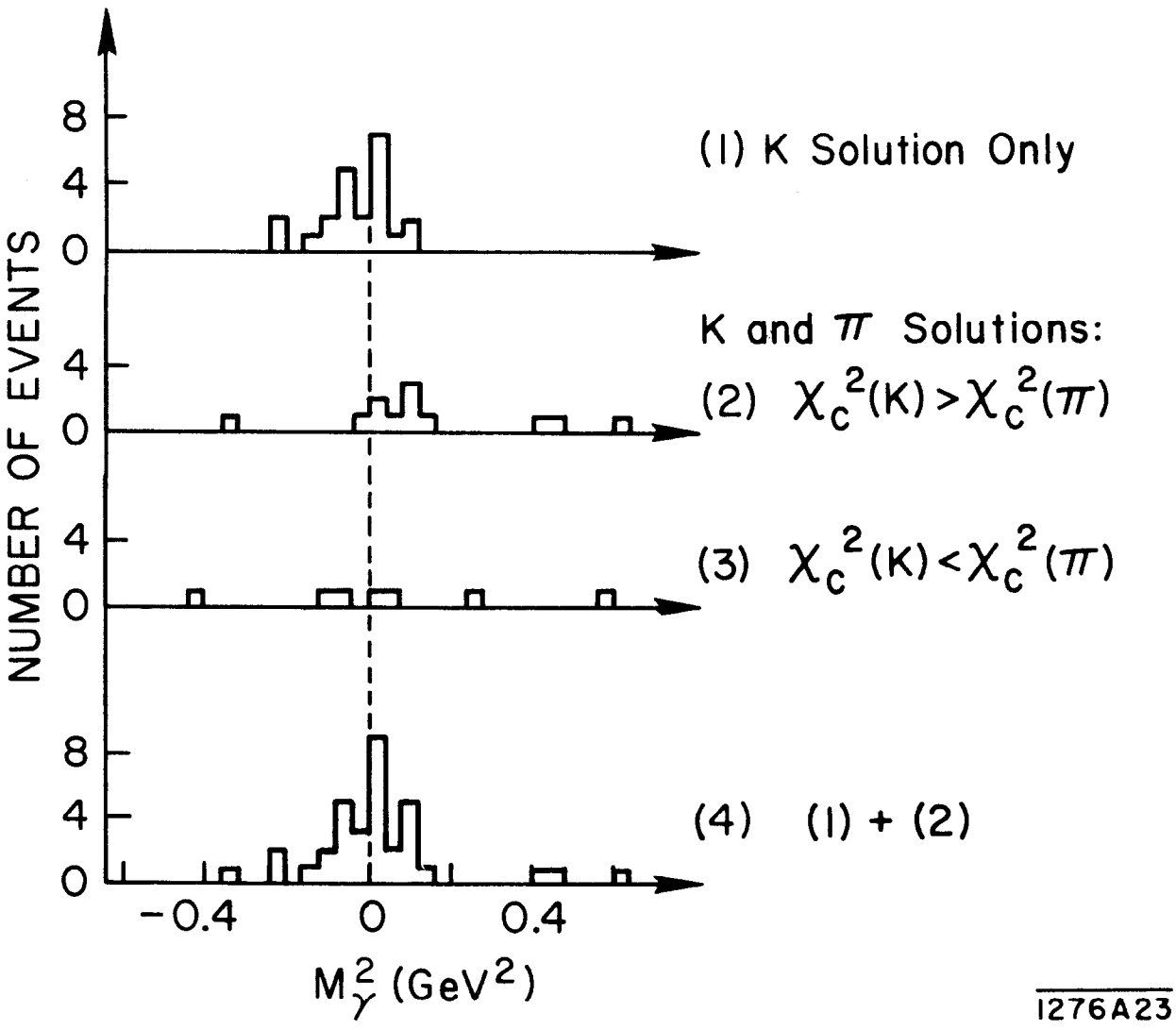
NUMBER OF EVENTS
8
4
0
4
0
4
0
8
4
0
(1) K Solution Only
K and π Solutions:
(2) $\chi_c^2(K) > \chi_c^2(\pi)$
(3) $\chi_c^2(K) < \chi_c^2(\pi)$
(4) (1) + (2)
-0.4
0
0.4
M_γ^2 (GeV^2)
1276A23

Fig. 33

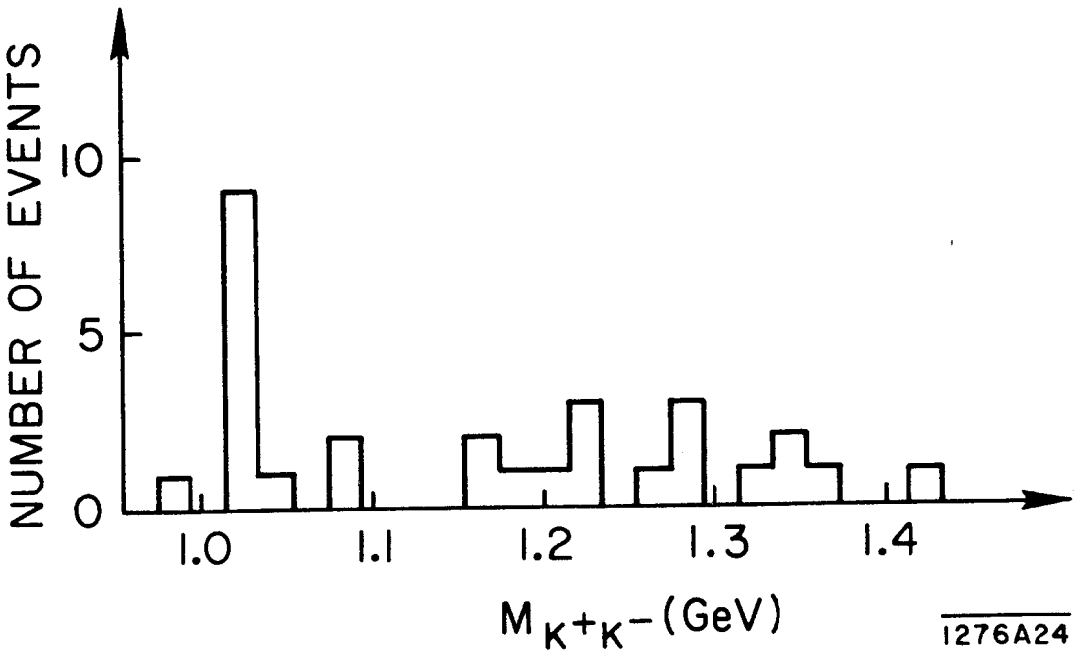

Fig. 34

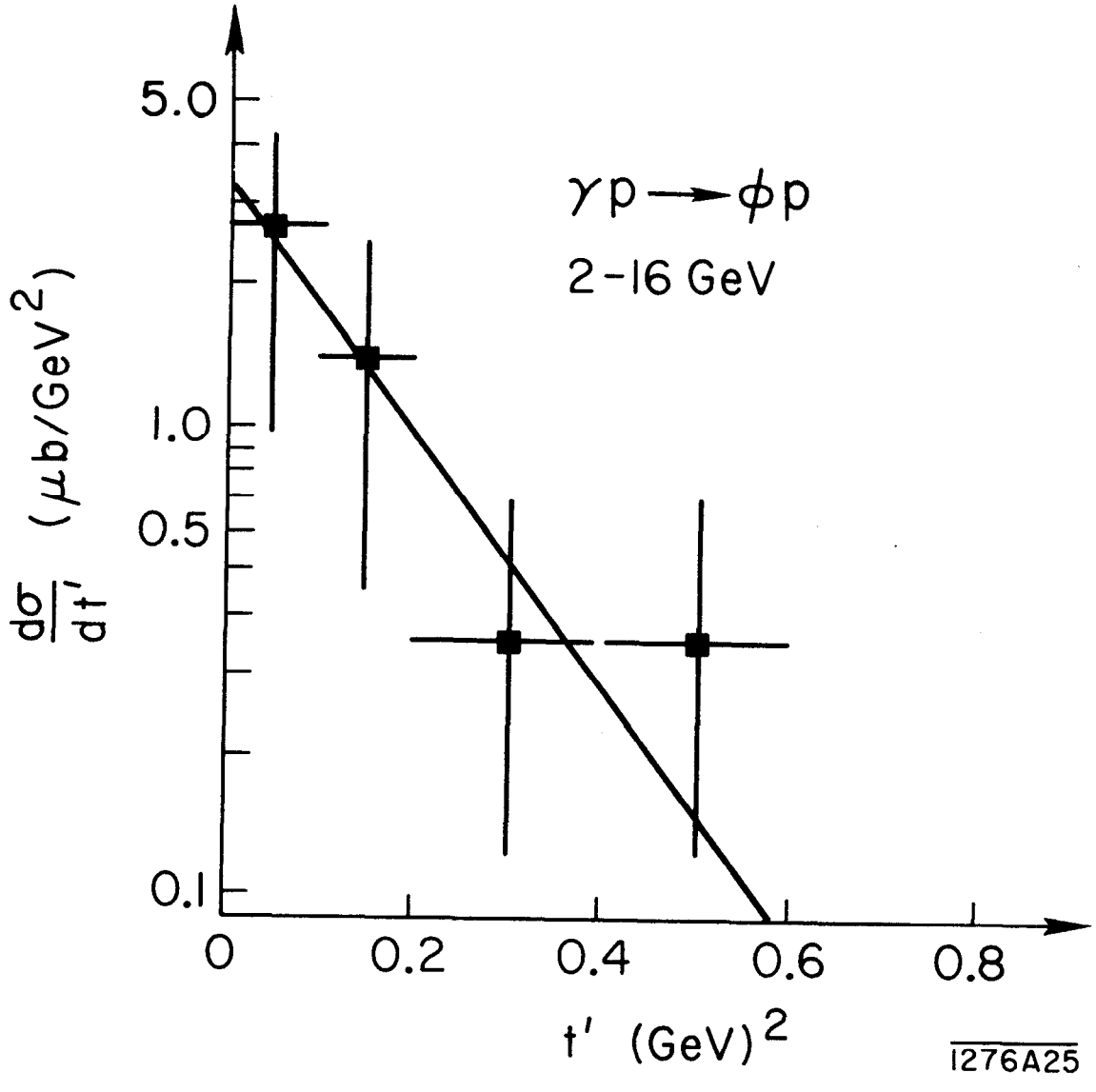
5.0
1.0
0.5
0.1
0
0.2
0.4
0.6
0.8
$\frac{d\sigma}{dt'}$ (μb/GeV^2)
$\gamma p \rightarrow \phi p$
2-16 GeV
t' (GeV)^2
1276A25

Fig. 35

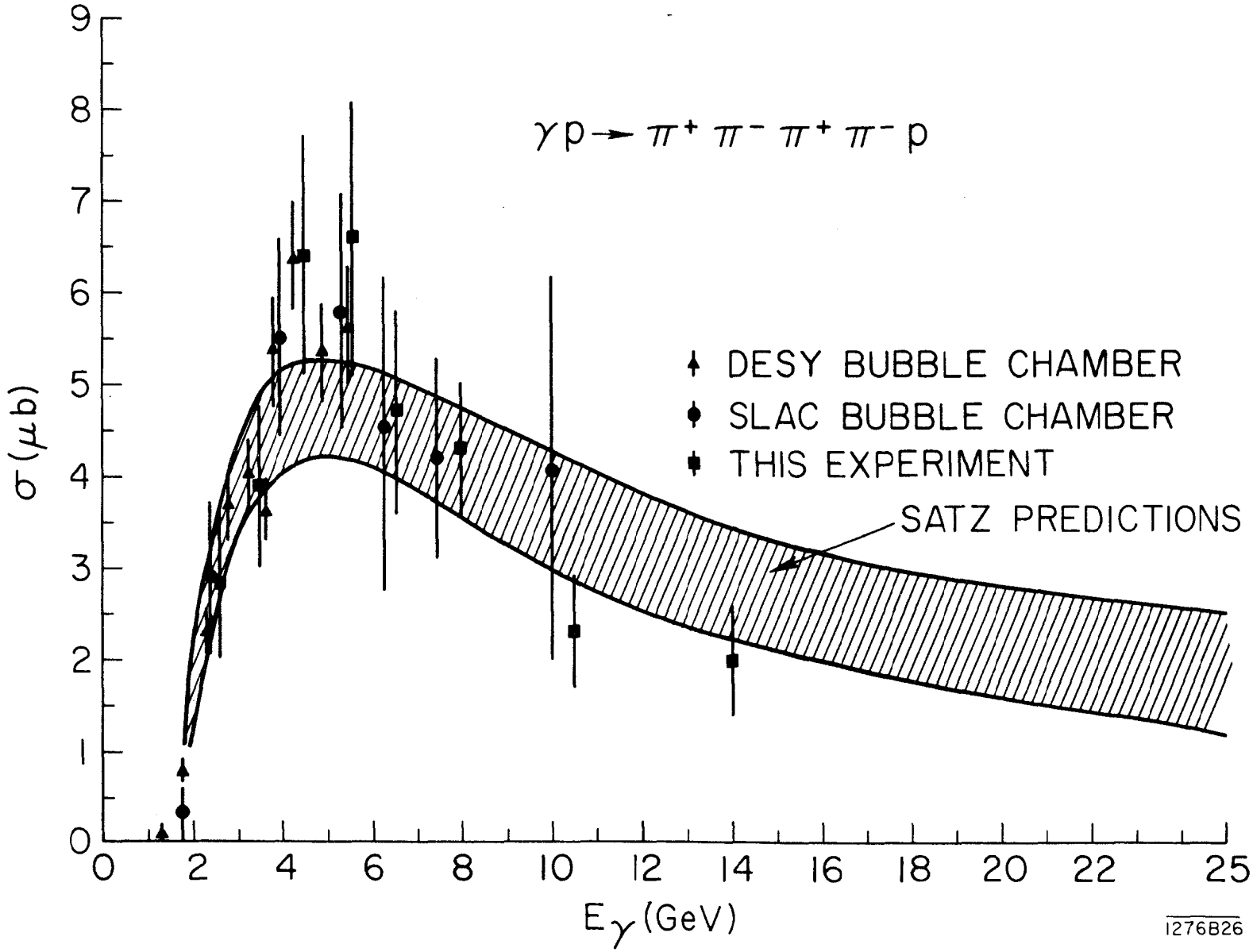
$\gamma p \rightarrow \pi^+ \pi^- \pi^+ \pi^- p$
DESY BUBBLE CHAMBER
SLAC BUBBLE CHAMBER
THIS EXPERIMENT
SATZ PREDICTIONS
$\sigma(\mu b)$
E_γ (GeV)
0
1
2
3
4
5
6
7
8
9
0
2
4
6
8
10
12
14
16
18
20
22
25
1276B26

Fig. 36

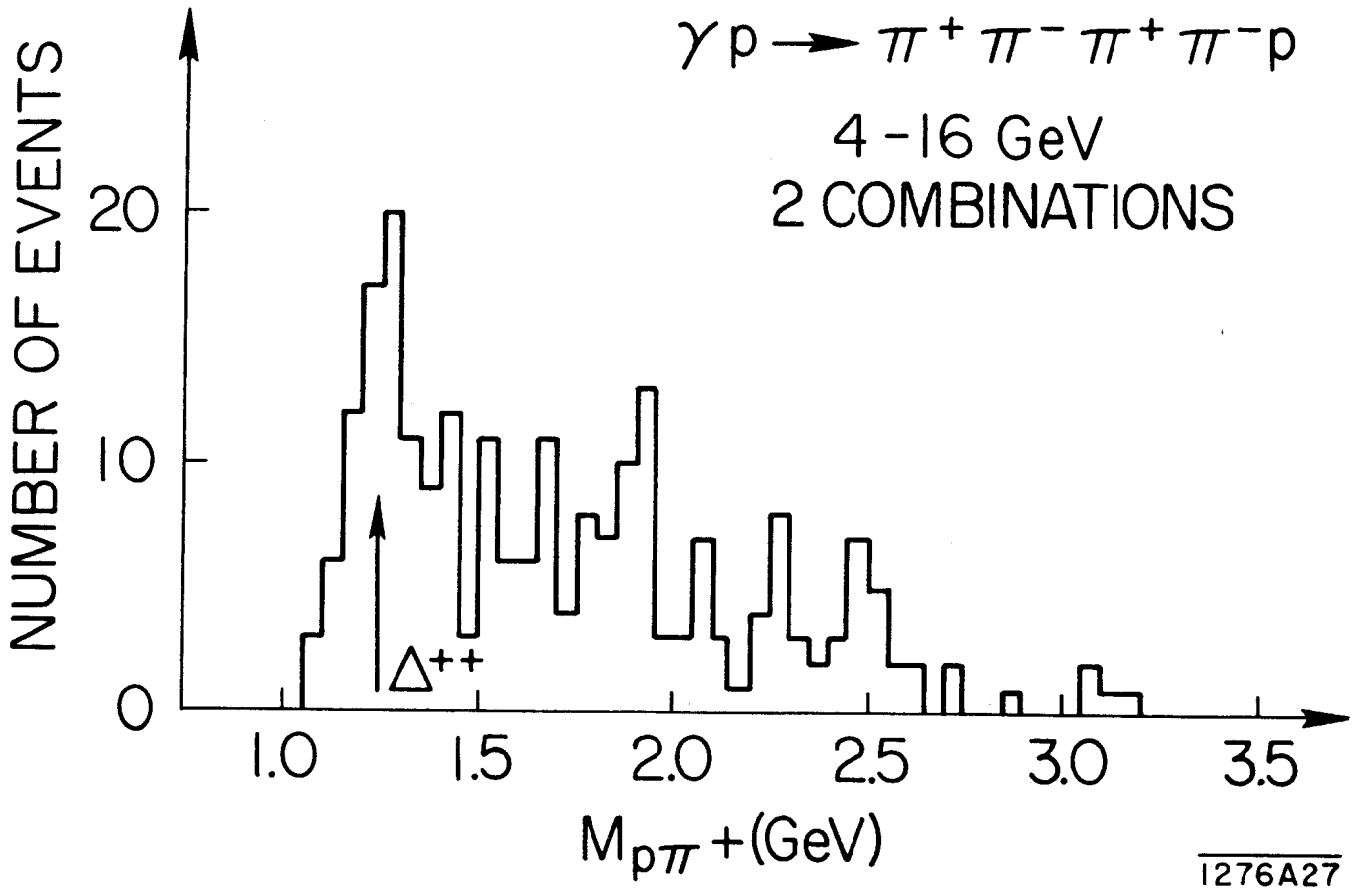
$\gamma p \rightarrow \pi^+ \pi^- \pi^+ \pi^- p$
4 - 16 GeV
2 COMBINATIONS
NUMBER OF EVENTS
20
10
0
Δ^{++}
1.0
1.5
2.0
2.5
3.0
3.5
$M_{p\pi^+}$ (GeV)
1276A27

Fig. 37

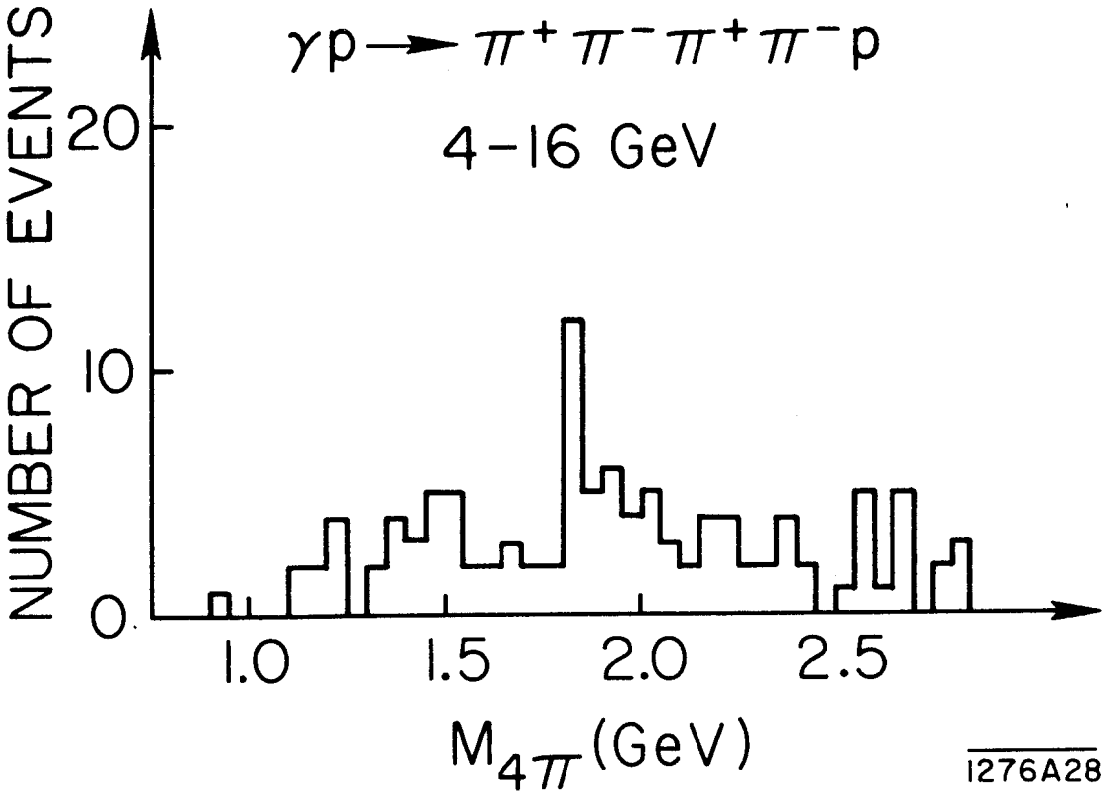
γp → π⁺π⁻π⁺π⁻p
4-16 GeV
NUMBER OF EVENTS
20
10
0
1.0
1.5
2.0
2.5
M4π (GeV)
1276A28

Fig. 38

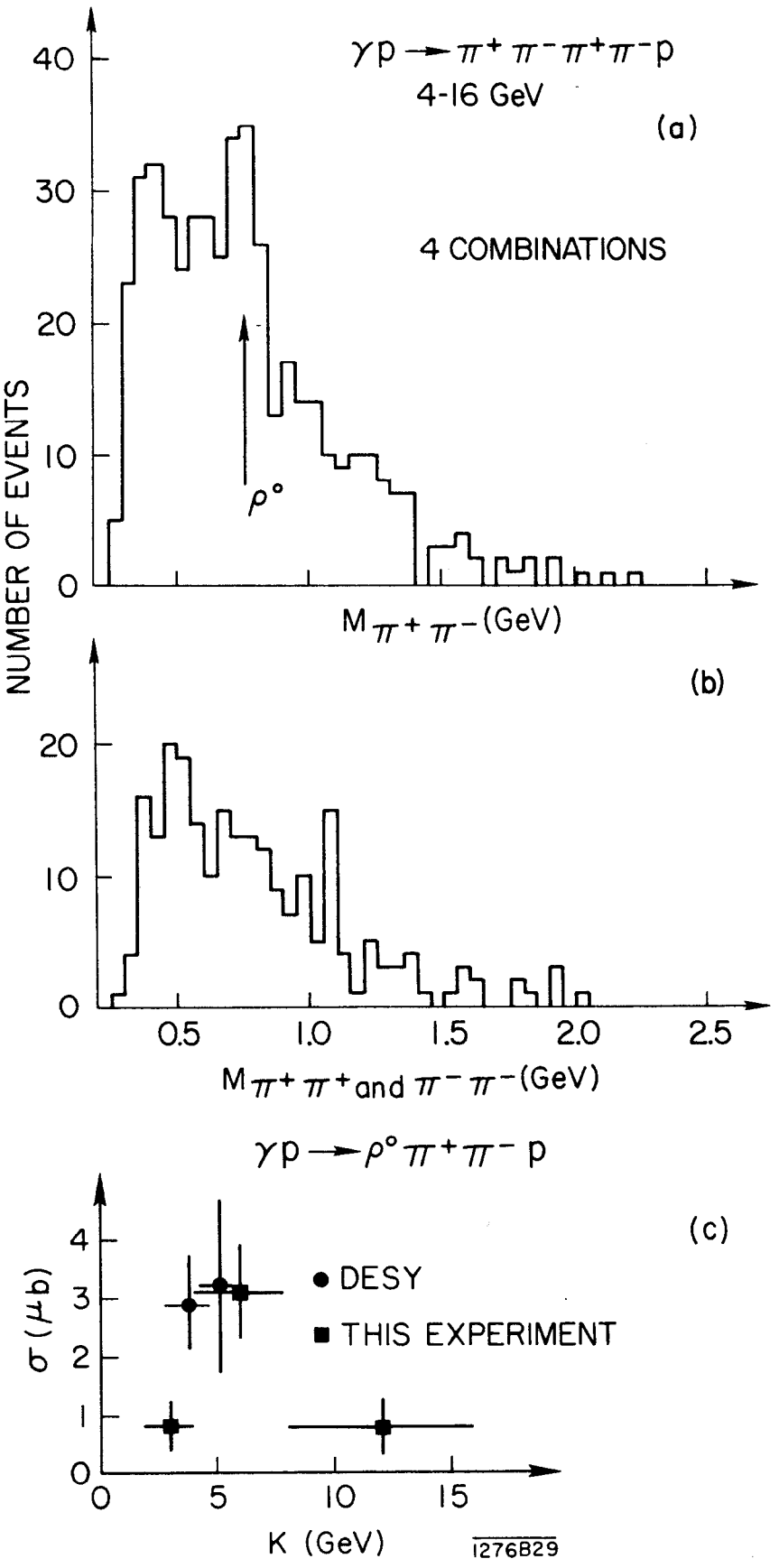
γp → π+ π− π+ π− p
4-16 GeV
(a)
4 COMBINATIONS
ρ°
NUMBER OF EVENTS
M π+ π− (GeV)
(b)
M π+ π+ and π− π− (GeV)
γp → ρ° π+ π− p
(c)
● DESY
■ THIS EXPERIMENT
σ (μb)
K (GeV)
1276B29

Fig. 39

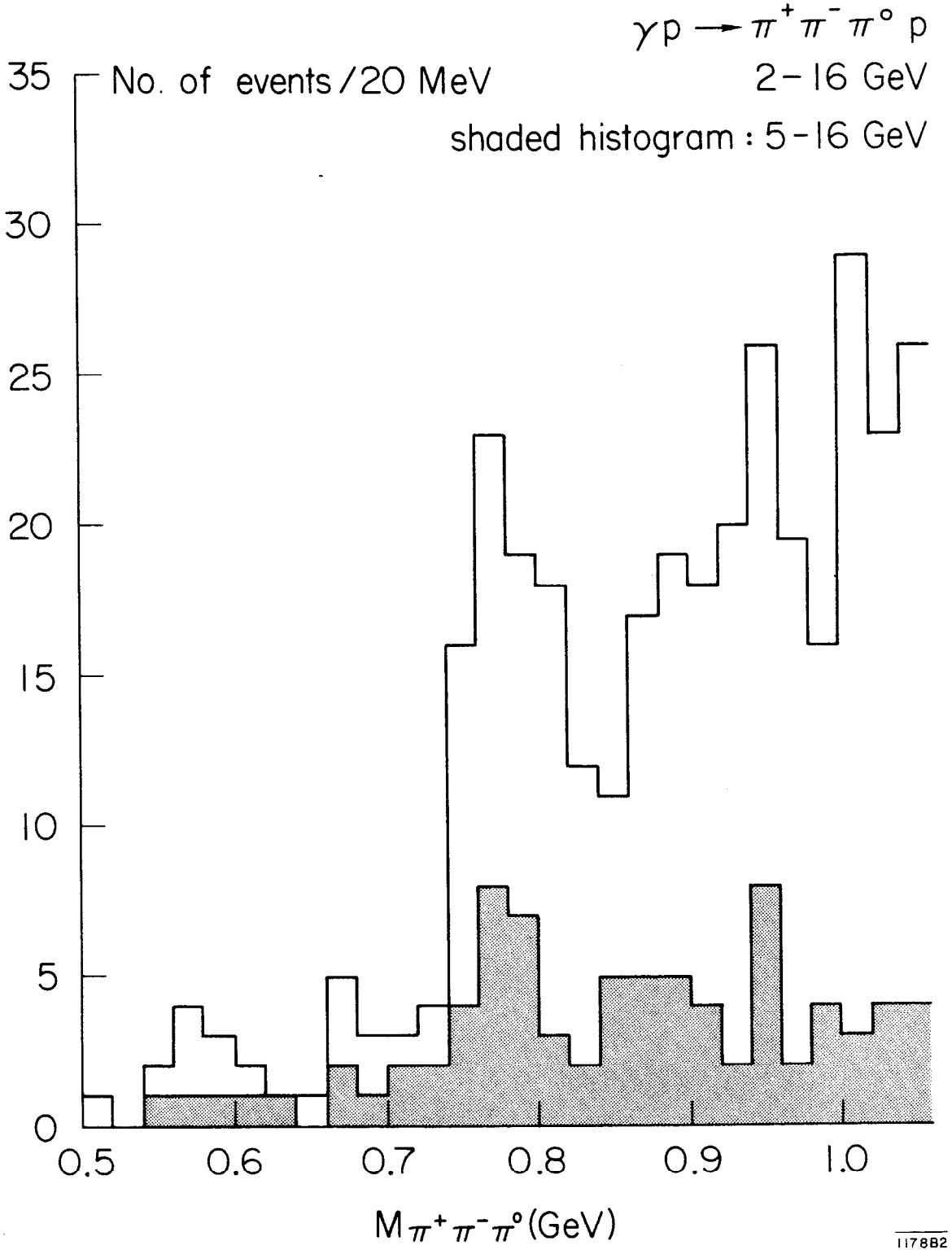
$\gamma p \rightarrow \pi^+\pi^-\pi^\circ p$
2-16 GeV
shaded histogram : 5-16 GeV
No. of events / 20 MeV
35
30
25
20
15
10
5
0
0.5
0.6
0.7
0.8
0.9
1.0
$M_{\pi^+\pi^-\pi^\circ}$ (GeV)
1178B2

Fig. 40

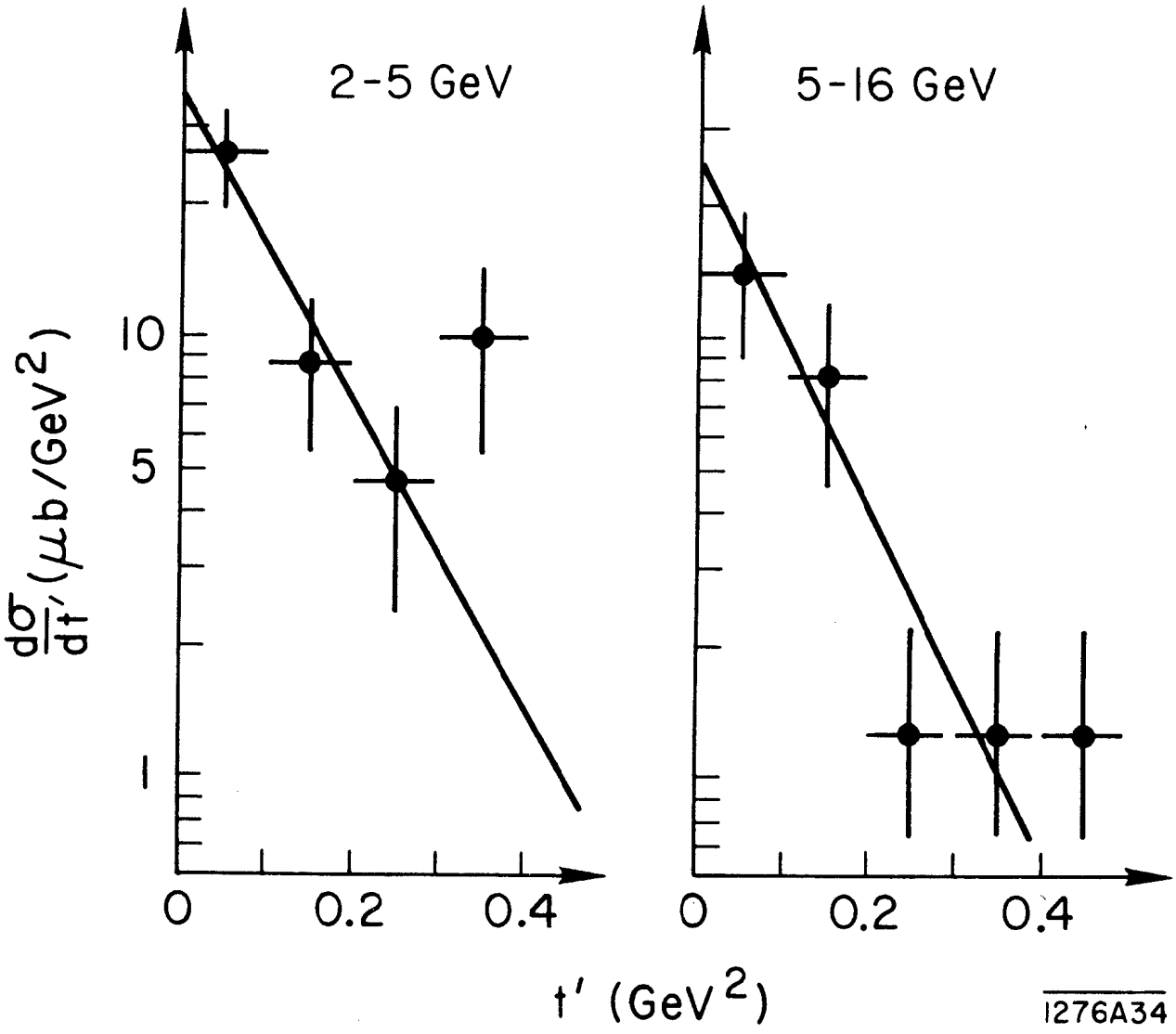
2-5 GeV
5-16 GeV
10
5
1
0
0.2
0.4
0
0.2
0.4
$\frac{d\sigma}{dt'}(\mu b/GeV^2)$
$t'\ (GeV^2)$
1276A34

Fig. 41

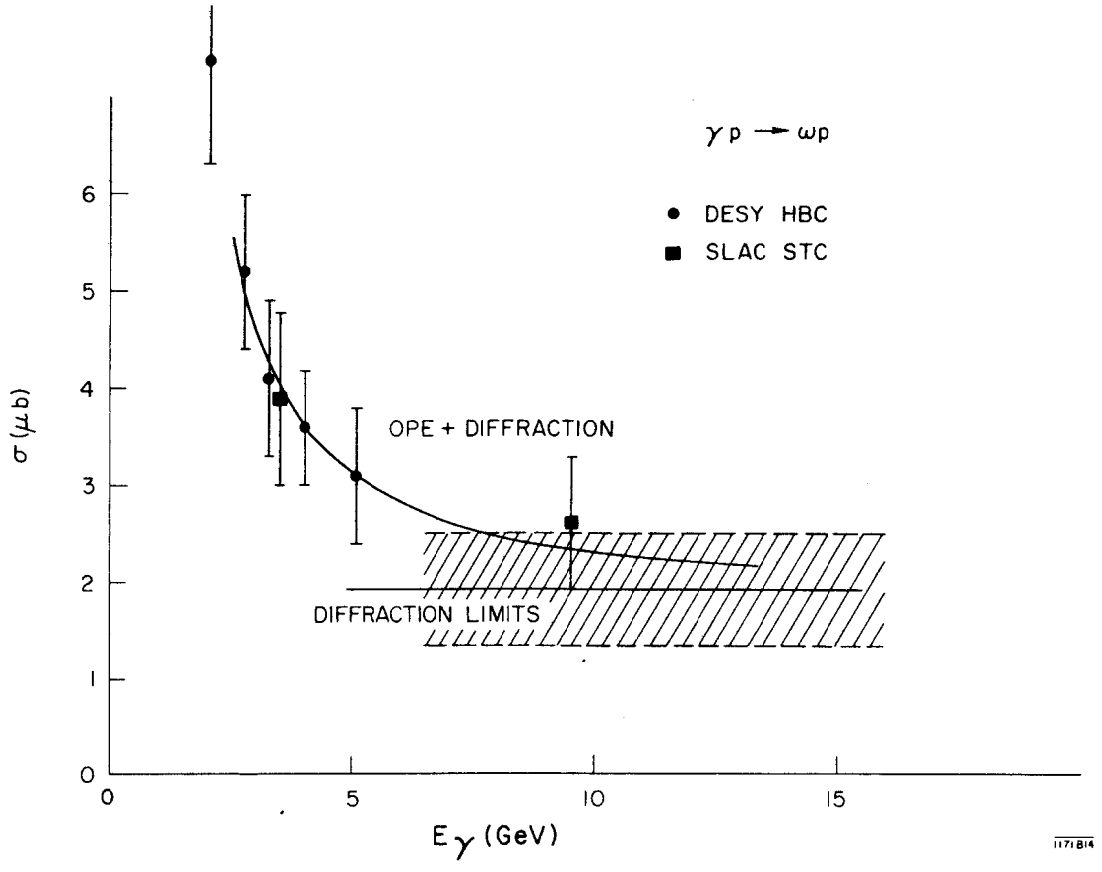
γ p → ωp
DESY HBC
SLAC STC
OPE + DIFFRACTION
DIFFRACTION LIMITS
σ (μb)
E γ (GeV)
0
1
2
3
4
5
6
0
5
10
15
1171B14

Fig. 42

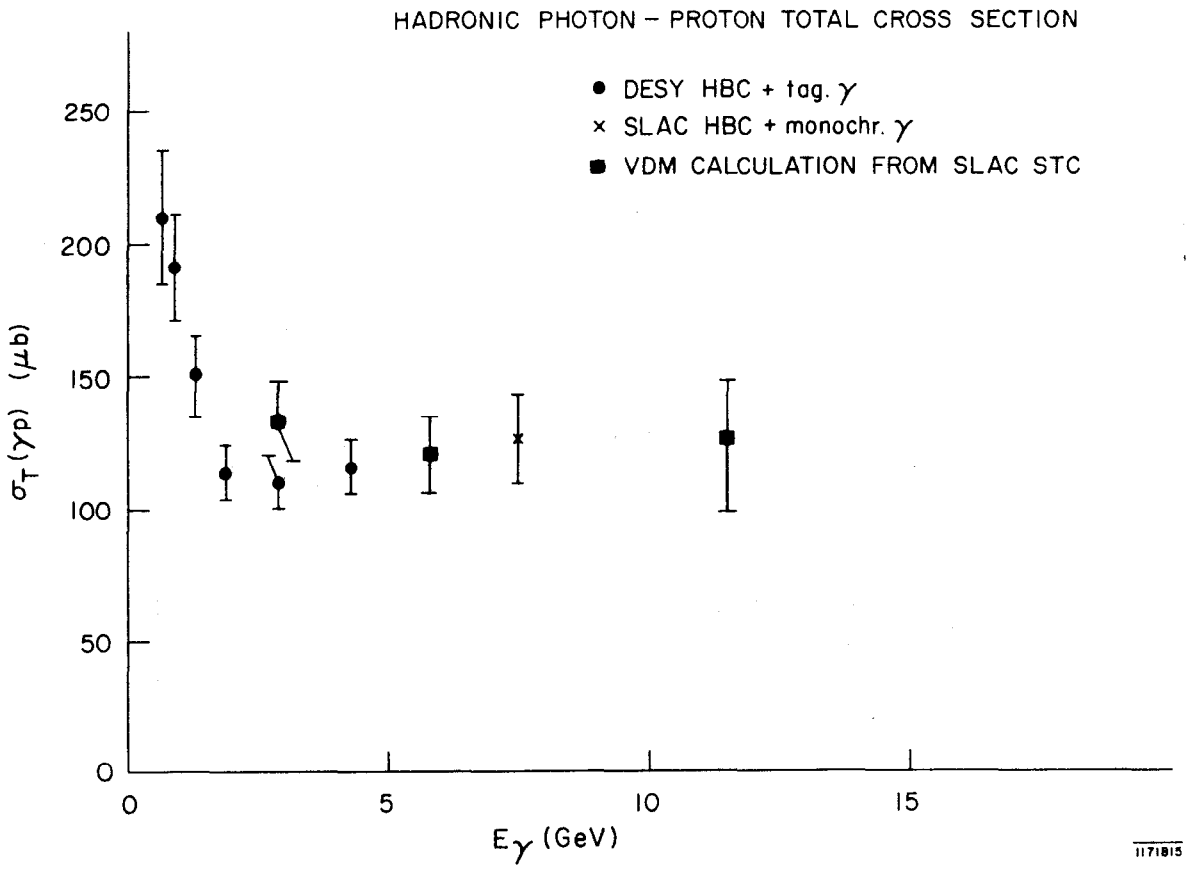
HADRONIC PHOTON – PROTON TOTAL CROSS SECTION
• DESY HBC + tag. γ
× SLAC HBC + monochr. γ
■ VDM CALCULATION FROM SLAC STC
250
200
150
100
50
0
$\sigma_T(\gamma p)$ (μb)
0
5
10
15
E_γ (GeV)
1171815

Fig. 43